



저작자표시-비영리-변경금지 2.0 대한민국

이용자는 아래의 조건을 따르는 경우에 한하여 자유롭게

- 이 저작물을 복제, 배포, 전송, 전시, 공연 및 방송할 수 있습니다.

다음과 같은 조건을 따라야 합니다:



저작자표시. 귀하는 원저작자를 표시하여야 합니다.



비영리. 귀하는 이 저작물을 영리 목적으로 이용할 수 없습니다.



변경금지. 귀하는 이 저작물을 개작, 변형 또는 가공할 수 없습니다.

- 귀하는, 이 저작물의 재이용이나 배포의 경우, 이 저작물에 적용된 이용허락조건을 명확하게 나타내어야 합니다.
- 저작권자로부터 별도의 허가를 받으면 이러한 조건들은 적용되지 않습니다.

저작권법에 따른 이용자의 권리는 위의 내용에 의하여 영향을 받지 않습니다.

이것은 [이용허락규약\(Legal Code\)](#)을 이해하기 쉽게 요약한 것입니다.

[Disclaimer](#)

공학박사 학위논문

**Integrated crystal plasticity and phase
field model for predicting
microstructure-mechanical properties
relationship of steels**

결정 소성 유한 요소 모델과 상장 모델 결합을 통한
철강 소재의 변형 및 열처리 후 미세조직-기계적
물성 관계 예측

2023 년 8 월

서울대학교 대학원
재료공학부
민 경 문

Integrated crystal plasticity and phase field model for predicting microstructure-mechanical properties relationship of steels

결정 소성 유한 요소 모델과 상장 모델 결합을 통한
철강 소재의 변형 및 열처리 후 미세조직-기계적
물성 관계 예측

지도 교수 이명규, 한홍남

이 논문을 공학박사 학위논문으로 제출함
2023년 8월

서울대학교 대학원
재료공학부
민경문

민경문의 공학박사 학위논문을 인준함
2023년 6월

위원장 유 웅 열 (인)

부위원장 이 명 규 (인)

위 원 한 홍 남 (인)

위 원 차 필 령 (인)

위 원 봉 혁 중 (인)

Abstract

Structural metallic materials are typically manufactured through a series of thermo-mechanical processes, including hot rolling, cold rolling, and heat treatment. These processes cause the materials to undergo elastic-plastic deformation along with recovery, recrystallization, grain growth, and sometimes phase transformation. As a result, microstructural characteristics such as grain size and crystallographic orientation (texture) are evolved. Such microstructure evolutions directly affect the mechanical properties of the material, including anisotropy and formability. Consequently, understanding the relationship between process, microstructure, property, and performance is essential during the process design stage to obtain a final product that meets performance requirements.

In this study, an integrated model that combines crystal plasticity finite element model (CPFEM) and phase field model (PFM) was proposed to simulate the thermo-mechanical processing of steels. The CPFEM was used as a mechanical simulation module, predicting deformation heterogeneities such as local stress concentration, inhomogeneous dislocation distribution, and shear bands. The PFM was employed as a microstructural evolution simulation module, predicting the recrystallized microstructural characteristics, including nucleation and growth, during heat treatment. To

fully couple CPFEM and PFM, which utilize finite element method and finite difference method as numerical schemes, respectively, an efficient coupling algorithm that does not lead to high computational cost was proposed. Specifically, a generalized strain energy release maximization (SERM) model, capable of predicting recrystallization texture in steels by utilizing CPFEM analysis results and considering multiple slip activities under mechanical loading conditions, was implemented within PFM. The proposed model was validated using ultra-low carbon steel and grain-oriented electrical steel.

For ultra-low carbon steel, the proposed model was applied to evaluate the anisotropy and formability of the thermo-mechanically processed material through virtual mechanical experiments. The r-values (Lankford coefficients) and yield stresses were predicted through virtual mechanical experiments and then validated by comparing them to experimentally measured values. Subsequently, the parameters of anisotropic yield functions, such as Hill'48 and Yld2000-2d, were determined using the predicted and measured values. Lastly, the identified yield functions and the Marciniak-Kuczynski (M-K) model were used to predict the forming limit diagram (FLD). In particular, the CPFEM-based M-K model was also utilized in this study to predict the FLD and validate the proposed model by comparing it to experimentally measured values.

For grain-oriented electrical steel, the proposed model was used to

predict the nucleation of Goss{110}<001> grains within shear bands during the early stages of primary recrystallization. A dual-scale representative volume element (RVE) modeling approach was employed to predict shear bands from CPFEM. Through this approach, the relationship between shear band evolution and slip mechanism, as well as the role of shear bands as preferred nucleation sites, were discussed. Subsequently, the differences in recrystallization texture resulting from shear band evolution were discussed, confirming that the predominant texture components determining the characteristics of electrical steel, including Goss grains, originate from shear bands. Model validation was conducted by comparing the predicted cold-rolled and recrystallized microstructures to experimental observations.

In conclusion, the proposed model, through its application to two types of steel, demonstrated efficient and accurate prediction of the relationship between process, microstructure, property, and performance.

Keywords: Crystal plasticity; Phase field model; Static recrystallization; Shear band; Texture; Anisotropy; Formability

Student number: 2018-24252

Contents

Abstract	iii
Contents.....	vi
List of Tables.....	ix
List of Figures	x
1. Introduction	1
1.1. Computationally driven material development and process design	1
1.2. Virtual thermo-mechanical process design of structural metals.....	6
1.3. Research objective.....	15
2. Integrated crystal plasticity and phase field model.....	18
2.1. Multi-scale approach: an overview.....	18
2.2. Crystal plasticity finite element model.....	22
2.2.1. Kinematics.....	22
2.2.2. Dislocation density evolution during plastic deformation	24
2.2.3. Plastic deformation due to shear band formation.....	28
2.2.4. Numerical implementation.....	31
2.2.5. Representative microstructure model and periodic boundary conditions	32
2.3. Multi-phase field model.....	34
2.3.1. Phase field equation	34
2.3.2. Grain boundary anisotropy.....	36

2.3.3. Parameters in phase field equation.....	38
2.3.4. Numerical implementation.....	39
2.4. Numerical mapping between CPFEM and PFM.....	40
2.5. Nucleation modeling with consideration of recovery	44
2.6. Strain energy release maximization model and its generalization	48
3. Application I: Virtual identification of anisotropy and formability for thermo-mechanically processed ultra-low carbon steel.....	57
3.1. Introduction	57
3.2. Experiments.....	61
3.2.1. Material	61
3.2.2. Basic mechanical properties.....	64
3.2.3. Heat treatment for static recrystallization	65
3.3. Results and discussion.....	70
3.3.1. Constitutive parameter identification	70
3.3.2. Simulation of cold-rolled ultra-low carbon steel.....	73
3.3.3. Simulation of recrystallized ultra-low carbon steel	79
3.3.4. Prediction of anisotropy and formability of ultra-low carbon steel	93
3.4. Summary.....	105
4. Application II: Effect of non-crystallographic shear band on formation of Goss texture in primary recrystallization of grain-oriented electrical steel.....	107
4.1. Introduction	107
4.2. Experimental methods.....	111

4.2.1. Material	111
4.2.2. Mechanical tests	113
4.2.3. Microstructure characterization	114
4.3. Results and discussion	117
4.3.1. Constitutive parameter identification	117
4.3.2. Simulation of cold-rolled GO electrical steel.....	120
4.3.3. Simulation of recrystallized GO electrical steel.....	136
4.4. Summary.....	148
5. Conclusion	150
Reference	154
Appendix A. Time integration procedure and analytical Jacobian for crystal plasticity finite element model	172
Appendix B. Stress fields around dislocation arrays	191
Appendix C. Dislocation densities measurement using the X-ray diffraction	196
Korean abstract	203
감사의 글	206

List of Tables

Table 1-1. Commonly employed computational models at different length scales and their main purposes.	4
Table 3-1. Chemical compositions of the investigated ultra-low carbon steel sheet (weight %).	61
Table 3-2. Basic mechanical properties of the investigated ultra-low carbon steel.	64
Table 3-3. Constitutive model parameters of the investigated ultra-low carbon steel.	71
Table 3-4. Measured and predicted plastic anisotropy in annealed ultra-low carbon steel, featuring the Lankford coefficients and normalized yield stresses along various material orientations.	97
Table 3-5. Material parameters of annealed ultra-low carbon steel used for anisotropic yield functions.	98
Table 4-1. Basic mechanical properties of the investigated grain-oriented electrical steel.	113
Table 4-2. Constitutive model parameters of the investigated grain-oriented electrical steel.	118

List of Figures

Fig. 1-1. Hierarchical framework of electronic- to macro-scale computational models and experiments for multiscale modeling approach. Computational models: Ab initio [1], molecular dynamics (MD)/kinetic Monte Carlo (KMC) [2], dislocation dynamics (DD) [3], microstructure-based finite element model (FEM) [4], and continuum-based FEM [5]. Experiments: Atomic probe tomography (APT) [6], high-resolution transmission electron microscopy (HRTEM) [7], transmission electron microscopy (TEM)/scanning electron microscopy (SEM) [6], electron back scatter diffraction (EBSD) [4], and component [5].5

Fig. 2-1. Overall flow chart of the integrated CP-PF approach.21

Fig. 2-2. Schematic illustrations of the numerical mapping for (a) grain orientations using Wigner-Seitz cell and (b) stored energy.....43

Fig. 2-3. Regularization of coarse integration points by introducing virtual integration points during the Wigner-Seitz mapping.....43

Fig. 2-4. Schematic illustrations of the SERM model in 1-D analogy [14].49

Fig. 2-5. Schematic diagram for predicting recrystallization orientation from deformation orientation using GSERM model.....52

Fig. 2-6. Procedure to calculate recrystallized orientation by proposed ESD concepts for (a) FCC and (b) BCC crystals.....55

Fig. 3-1. Microstructure of the investigated ultra-low carbon steel. (a) Normal direction inverse pole figure map, and (b) (110), (200), and (211) pole figures.63

Fig. 3-2. Heat treatment conditions for reproducing static recrystallization.	67
Fig. 3-3. Engineering stress-strain curves of the ultra-low carbon steel in different heat treatment conditions.	67
Fig. 3-4. Microstructure evolutions during heat treatment. (110), (200), and (211) pole figures (above) and normal direction inverse pole figure maps (below).	68
Fig. 3-5. Grain size distributions of (a) as-received, (b) cold-rolled, and (c) annealed (fully recrystallized) specimens.	69
Fig. 3-6. Comparison of CP calculated stress-strain curve with measured one for ultra-low carbon steel.	72
Fig. 3-7. Representative volume element model for hot-rolled ultra-low carbon steel.....	74
Fig. 3-8. Deformed representative volume element and its equivalent plastic strain after a thickness reduction ratio of 85.5%.	75
Fig. 3-9. (a) Deformed representation volume element and its total dislocation densities (unit: m^{-2}) after a thickness reduction ratio of 85.5% rolling and (b) comparison of total dislocation densities before (with CPFEM) and after mapping to PFM grids.	76
Fig. 3-10. Predicted rolling texture of ultra-low carbon steel after a thickness reduction ratio of 85.5%. (a) (110), (200), and (211) pole figures and (b) $\varphi_2=45^\circ$ orientation distribution function section.	78

Fig. 3-11. Microstructure evolution during static recrystallization of ultra-low carbon steel using integrated CP-PF model. The colors indicate the normal direction inverse pole figure map. At the 1.4 s mark, red dotted circles highlight the sites of the first nucleation.....82

Fig. 3-12. Schematic illustration of nucleation criterion used in the PFM simulation. The red intersection point represents the incubation time for nucleation.....84

Fig. 3-13. Predicted recrystallization texture of ultra-low carbon steel. (a) (110), (200), and (211) pole figures and (b) $\phi_2=45^\circ$ orientation distribution function section.....87

Fig. 3-14. Measured recrystallization texture of ultra-low carbon steel. (a) (110), (200), and (211) pole figures and (b) $\phi_2=45^\circ$ orientation distribution function section.....88

Fig. 3-15. Fraction of recrystallization with Johnson-Mehl-Avrami-Kolmogorov (JMAK) equation.90

Fig. 3-16. Predicted and measured grain size distributions after annealing.91

Fig. 3-17. Microstructure generation by the proposed modeling approach. The colors indicate the normal direction inverse pole figure map.92

Fig. 3-18. (a) Representative volume element (RVE) model for virtual mechanical tests based on predicted microstructural information of annealed ultra-low carbon steel and (b) example of deformed RVE and its equivalent plastic strain after the virtual uniaxial tensile test.95

Fig. 3-19. Comparison of the measured and predicted plastic anisotropy in annealed ultra-low carbon steel, featuring the Lankford coefficients and normalized yield stresses along various material orientations.96

Fig. 3-20. Variations of r-value and normalized yield stress for annealed ultra-low carbon steel along various material orientations, obtained using various anisotropic yield functions based on (a) experimental and (b) predicted values.	99
Fig. 3-21. Identified yield loci for annealed ultra-low carbon steel, obtained using the various anisotropic yield functions.	100
Fig. 3-22. Comparison of forming limit diagrams for annealed ultra-low carbon steel, obtained using various yield functions and crystal plasticity-based approach (CPFLD), with experimental values. ...	104
Fig. 4-1. (a) Normal direction inverse pole figure map and (b) $\phi_2=45^\circ$ section of orientation distribution function of hot-rolled GO electrical steel.	112
Fig. 4-2. (a) Optical microscope image of the region with activated shear bands (TD section), (b) scanning electron microscope image of the focused iron beam milling target area (white circle), and (c) transmission electron microscope sample obtained using focused ion beam milling.	116
Fig. 4-3. Comparison of CP calculated stress-strain curve with measured one for the grain-oriented electrical steel.	119
Fig. 4-4. Dual-scale cubic representative volume element models for GO electrical steel: RVE ₂₂₄ model on the left side and RVE ₁₈ model on the right side.	121

- Fig. 4-5.** Deformed representative volume elements (RVEs) and their equivalent plastic strains. (a) Results after achieving a thickness reduction ratio of 76%, with RVE₂₂₄ model on the left side and RVE₁₈ model on the right side. (b) Results after a achieving a thickness reduction ratio of 90%, with RVE₂₂₄ model on the left side and RVE₁₈ model on the right side.122
- Fig. 4-6.** $\varphi_2=45^\circ$ ODF sections of cold-rolled GO electrical steel. (a, b) Rolling texture measured using XRD analysis after a thickness reduction ratio of 76% and 90%, respectively. (c, d) Rolling texture predicted through CP finite element analysis using the macroscopic RVE₂₂₄ model after a thickness reduction ratio of 76% and 90%, respectively.125
- Fig. 4-7.** (a, b) Evolution of the edge and screw dislocation densities and (c, d) screw/edge dislocation fraction of two selected grains in the grain boundary and interior regions, respectively.....128
- Fig. 4-8.** Accumulated shear strain for shear band (γ^z) of (a) the small-scale RVE₁₈ model and (b, c, d) grains with obvious shear bands after a thickness reduction ratio of 76%. For visual clarity, contours have been mapped in the undeformed configuration.130
- Fig. 4-9.** $\varphi_2=45^\circ$ ODF sections of cold-rolled GO electrical steel predicted by the CP using the small-scale RVE₁₈ model. (a, b) Rolling texture after a thickness reduction ratio of 76% and 90%, respectively. (c, d) Rolling texture in the shear band activated elements after a thickness reduction ratio of 76% and 90%, respectively. (e, f) Rolling texture in the elements without shear bands after a thickness reduction ratio of 76% and 90%, respectively.134

Fig. 4-10. Evolution of total dislocation densities in the regions with and without shear band activation.....135

Fig. 4-11. (a) Normal direction (ND) inverse pole figure (IPF) map of cold-rolled GO electrical steel subjected to heat treatment at 600 °C for 60 s. (b) ND IPF map and (c) rolling direction IPF map in which other texture components except Goss have been suppressed to highlight the Goss texture. In (b) and (c), the yellow dotted lines indicate the shear bands.....138

Fig. 4-12. Nucleation of Goss grain (white circle) within shear band (yellow dotted line) with the $\{111\}\langle 112\rangle$ component, measured using TEM orientation imaging. (a) Normal direction inverse pole figure (IPF) map, (b) rolling direction IPF map, and (c) confidence index map.140

Fig. 4-13. Predicted nucleation orientation probabilities for recrystallized GO electrical steel in the regions (a) with shear bands and (b) without shear bands.142

Fig. 4-14. Depiction of the target area for the PF simulation, indicated by the red dotted rectangle. The contour represents the accumulated shear strain for the shear band (γ^z), as predicted using the RVE₁₈ model.143

Fig. 4-15. Microstructure evolution in the shear band-dominant region during static recrystallization of GO electrical steel, as predicted using the integrated CP-PF model. The colors indicate the normal direction inverse pole figure map.146

Fig. 4-16. (a) Predicted and (b) measured recrystallization texture of GO electrical steel, represented by the $\varphi_2=45^\circ$ orientation distribution function section.147

보존용 학위논문 정오표

페이지	정정 전	정정 후
p. 203 : 13	결정 소성 유한 요소 모델 (crystal plasticity finite element model, PFM)	결정 소성 유한 요소 모델 (crystal plasticity finite element model, CPFEM)

1. Introduction

1.1. Computationally driven material development and process design

To date, material development and process design for manufacturing have relied heavily on experiments and skilled engineers who evaluate material properties and product performance. However, experiment-based approaches in material and process design require significant amounts of time and cost. In some cases, even when the fundamental properties are satisfied at the material design stage, manufacturing the final component may not be feasible due to challenges during the processing stage. Therefore, a more efficient and robust process design approach is necessary to bridge the gap between material development and industrial applications.

Computationally driven material development and process design have emerged as an alternative to experimental methods, helping to reduce production time and costs in the industry. However, early computational development has focused on disparate applications of numerical approaches for materials, processes, and performance, which has limited their effectiveness for systematically developing highly integrated manufacturing processes.

Recently, advancements in computational engineering have integrated processes, structures, properties, and performance into a virtual engineering

platform known as Integrated Computational Materials Engineering (ICME). ICME aims to understand the process-structure-property-performance relationship through computational modeling and simulations. Using a single model to represent the wide range of phenomena and scales for material systems is overly simplistic and doesn't allow for an adequate description and design of systems that account for material behavior across multiple scales. To address this challenge, multiscale modeling and simulation have been introduced as core ICME components, which can be achieved through the hierarchical integration of models that simulate material behavior at different length scales, enabling a quantitative examination of variable sensitivity for each scale.

Fig. 1-1 illustrates a hierarchical schematic of computational models and experiments at various length scales. Robust multiscale models should be developed based on the key mechanisms of material behavior, integrating experimental characterizations during the modeling process. Table 1-1 lists commonly employed computational models for structural materials at different length scales, along with their main purposes. Models are classified into those that predict material properties and performance based on structural information and those that simulate microstructure evolutions while considering the respective manufacturing processes. The process-structure-property-performance relationship can be realized with a valid scale-bridging

approach in multiscale simulations. For example, computational models for simulating microstructure evolution are implemented by coupling additional physical kinetics of material properties obtained from lower scales. Under this ICME scheme, simulations for manufacturing processes and product performance can be efficiently conducted, helping engineers develop optimal materials and processes with lower manufacturing costs.

Table 1-1. Commonly employed computational models at different length scales and their main purposes.

	Model	Length scale	Purpose
Material model (Structure- properties / performance)	Ab initio	Electronic	Calculation of basic chemical and physical properties of materials based on the potential energy induced from electronic structures
	Molecular dynamics (MD) / Kinetic Monte Carlo (KMC)	Nano-	Determination of the movement of atomic or molecular systems based on interatomic potential functions
	Dislocation dynamics (DD)	Micro-	Behavior of dislocation aggregates such as the movement and interaction of dislocations
	Crystal plasticity (CP)	Micro- ~ Meso-	Prediction of plastic deformation based on the slip system and orientation information
	Finite element method (FEM)	Macro-	Analysis of physical behaviors in engineering systems
Microstructure evolution (Process - structure)	Kinetic Monte Carlo (KMC)	Meso-	Full-field microstructure evolution, e.g., solidification, phase transformation, grain growth, and recrystallization
	Cellular automata (CA)		
	Phase field (PF)		

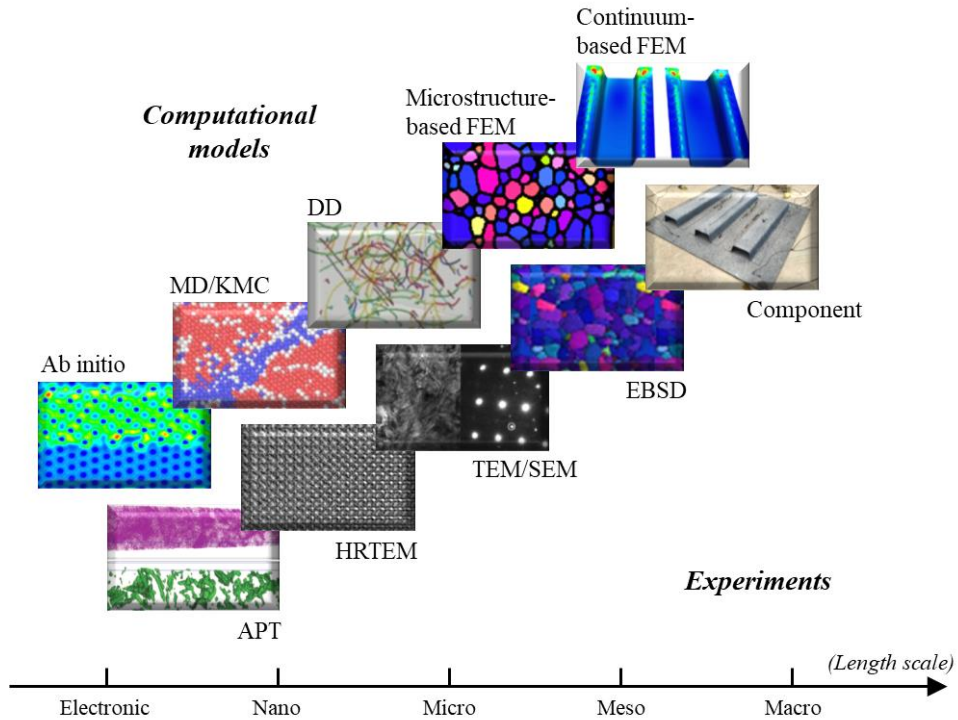


Fig. 1-1. Hierarchical framework of electronic- to macro-scale computational models and experiments for multiscale modeling approach. Computational models: Ab initio [1], molecular dynamics (MD)/kinetic Monte Carlo (KMC) [2], dislocation dynamics (DD) [3], microstructure-based finite element model (FEM) [4], and continuum-based FEM [5]. Experiments: Atomic probe tomography (APT) [6], high-resolution transmission electron microscopy (HRTEM) [7], transmission electron microscopy (TEM)/scanning electron microscopy (SEM) [6], electron back scatter diffraction (EBSD) [4], and component [5].

1.2. Virtual thermo-mechanical process design of structural metals

Structural metals are commonly manufactured through thermo-mechanical processing, which includes hot and cold working, along with a series of thermal and heat treatments. For example, sheet metals undergo several hot and cold rolling processes, followed by annealing heat treatment [8]. This intricate thermo-mechanical processing involves the accumulation and recovery of dislocations, which are complex events dependent on deformation, temperature, phase transformation, strain rate, and other factors.

During the annealing of metallic products, the energy stored in the polycrystalline microstructure from deformation is released through recovery, recrystallization, and grain growth processes. This alters microstructure characteristics, such as grain size (and distribution), dislocation structures, and crystallographic orientations (or texture). The evolution of the microstructure significantly influences the mechanical properties of the final products [9]. Mechanical properties of interest include stress-strain relations, anisotropy, path dependence, and ductility [10,11]. Thus, it is necessary to understand the relationships between thermo-mechanical processes, microstructures, and material properties during the material design stage to reduce time and cost while developing materials with improved performance.

During hot working, metallic materials exhibit unique mechanical

behavior and irreversible microstructural evolution, characterized by dynamic recrystallization (DRX). DRX is a recrystallization phenomenon that occurs at elevated temperatures during large plastic deformation, which is different from static recrystallization (SRX) during the annealing process. While both recrystallization processes involve the nucleation of new strain-free grains in the microstructure and their subsequent growth by releasing stored energy accumulated by mechanical deformation [8], DRX features specific flow stress patterns that can be attributed to the repeated deformation of nucleated grains and accumulation of stored energy. Flow stress comprises the following processes: (i) work hardening at the initial deformation stage, (ii) flow softening with single or multiple peak stresses, and (iii) steady-state flow attributed to microstructural evolution (e.g., crystallographic orientation, grain size, and recrystallization fraction) [12]. For more details on DRX, a review article by Huang and Logé is recommended [13].

A cold-worked metallic sheet with high stored energy induced by accumulated dislocations during deformation can recover its original strength and ductility by releasing the stored energy through annealing or the SRX process. Simultaneously, grains with preferred crystallographic orientations formed during cold working were consumed by newly nucleated strain-free grains with new orientations during SRX. Unlike the DRX process, SRX is a single process considering that nucleated grains do not exhibit sufficient

driving forces to cause repeated recrystallization. Therefore, the origin and evolution of polycrystalline textures during cold working and heat treatment have often been investigated. Moreover, the effect of the microstructure on resultant mechanical properties has been further studied to predict the anisotropy and formability of sheet metals in simulating cold working and annealing.

Recrystallization is known to originate from deformation-induced microstructural inhomogeneities, such as secondary particles, grain boundaries, shear bands, and transition bands [8]. Most of the typical driving forces for recrystallization are known to originate from non-homogeneously distributed dislocations within grains [14]. Therefore, to predict the mechanical properties after recrystallization (or particularly after annealing) of deformed metals, deformation-induced microstructural heterogeneities have to be understood. In addition to deformation modeling, subsequent microstructural evolutions during recrystallization will be required.

Crystal plasticity (CP) can be an effective tool for simulating the deformation inhomogeneities at the grain level and evolution of crystallographic orientations in polycrystalline metals. The mechanical properties of polycrystals were initially mathematically described by Taylor [15] based on crystallographic micromechanics and microstructure. Since then, a series of developments have extended this fundamental analysis.

Examples include the grain interaction model (GIA) developed by Crumbach et al. [16], the viscoplastic self-consistent (VPSC) model based on mean-field deformation theory [17,18], and crystal plasticity finite element models (CPFEM) that account for inter-grain equilibrium and compatibility [19–23], among many other modeling approaches. To incorporate more physics-based deformation mechanisms using simple or more realistic dislocation activities and structures, various dislocation density-based hardening models have been proposed and integrated into the framework of crystal plasticity. Several models based on dislocation density-based single crystal constitutive laws can be found in previous studies [12,24–29].

CP models have successfully simulated grain-level deformation and evolution of crystallographic orientations in single or polycrystalline metals. However, accurate modeling of recrystallization to elucidate the precise nucleation mechanism remains a challenge owing to the following: complexity of the microstructural heterogeneities present in the deformed grains, dependency of the nucleation rate on the orientation of the deformed grains, and different growth rates of nuclei into the neighboring deformed grains [30].

Significant efforts have been made in performing multiscale simulations that couple deformation and related microstructural evolutions, thanks to advances in simulations at individual length scales. Raabe and Becker [31]

combined CPFEM with a probabilistic kinetics-based cellular automata (CA) method to simulate the primary recrystallization of aluminum after plane strain compression. They applied a numerical mapping approach to integrate the solutions of the two-dimensional CP simulation with the domain of CA simulation, mapping the state variables including crystal orientations and stored elastic energy. Radhakrishnan et al. [32] and Radhakrishnan and Sarma [33] integrated CPFEM with Monte Carlo (MC) simulation to predict particle simulated nucleation during the recrystallization of aluminum alloys. Extending the approach of Radhakrishnan et al., Takaki and Tomita [34] utilized a multi-phase field model (PFM) coupled with CPFEM to simulate the static recrystallization process in aluminum, enabling them to calculate the occurrence of abnormal grain growth based on the deformation microstructure. Cho et al. [35] coupled FEM and PFM with a one-to-one correspondence method (or direct mapping) to analyze transformation plasticity during austenite-to-ferrite transformation in low carbon steel. Vondrous et al. [36] simulated cold-rolling and annealing of non-alloyed DC04 steel by coupling CPFEM and PFM, determining the nucleation criterion in their PFM from the difference between EBSD-measured grain numbers before and after heat treatment. Kim et al. [37] predicted the recrystallization texture of interstitial free (IF) steel using CPFEM coupled with the CA method. Zecevic et al. [38] proposed a recrystallization model

driven by intergranular orientation gradients and strain energy fields arising from mean-field viscoplastic self-consistent (VPSC) formulations and predicted the deformation and recrystallization texture of 90% drawn copper wire, 95% cold-rolled copper, and 88% compressed pure iron. Apart from simulating microstructure evolution in thermo-mechanical processes, Fromm et al. [39] constructed a three-dimensional microstructure of Ni-based superalloy IN100 from EBSD, used for grain growth simulation using PFM. They employed a direct mapping method between experimentally measured EBSD and PFM, conducting a uniaxial tensile test with CPFEM on the statistically generated microstructure from PFM simulation to predict mechanical properties. In addition to modeling recrystallization behavior, the PFM has been applied to unveil fundamental deformation mechanisms such as dislocation-mediated plasticity and heterogeneous twinning [40] and stress/temperature-induced phase transformations [41,42].

The mechanical properties, especially anisotropy and formability of metals, are closely related to the preferred crystallographic orientations of polycrystalline materials after thermo-mechanical processing. However, most existing computational models for simulating recrystallizations of metals rely on mapping of the empirically obtained texture information to the computational domain to predict the evolution of microstructure and corresponding mechanical properties. For instance, Fromm et al. [39] used

orientations of the IN100 alloy from experimental EBSD measurements and simulated the mechanical properties after statistical treatment.

Recrystallization texture modelling remains a subject of debate within the scientific community. The two prevailing theories that can be used to predict the recrystallization texture are the oriented nucleation (ON) and oriented growth (OG) theories. The ON theory proposes that preferentially formed nuclei with specific orientations determine the resulting recrystallization texture. However, the OG theory suggests that nuclei with specific rotation relationships with the deformed grains can preferentially grow, inducing rapid grain boundary migration. Because recrystallization can occur through nucleation and growth, both theories that have their own advantages and limitations explain the evolution of certain textures during recrystallization. For more details on recrystallization modeling, the review article by Gottstein and Sebald [43] is recommended.

More physics-based multiscale models have been proposed to calculate recrystallization textures based on either spatially discretized grains or the Avrami-type statistical method. One example of the former is the use of cellular automata (CA) models, where the cell flip of a non-recrystallized cell is calculated based on transformation probability, and the orientation of the recrystallized neighboring cell inherits the original crystal orientation [31,44,45]. A well-known model in the latter group includes the Sebald-

Gottstein model [46] or its extended model, such as the texture-component-based Avrami model [47], which uses statistically collected potential nucleation texture components by fitting known typical recrystallization textures of investigated materials. Models in the first group cannot consider the effect of the local stress state (often multiaxial) and its resultant inhomogeneous slip activities on nucleated orientations since recrystallized nuclei orientations inherit deformed grain orientations once the given nucleation criterion is met. The models in the latter group use statistically assumed spherical nuclei growing as a function of misorientation and stored energy, providing computational efficiency. However, they only consider relations with deformed grains and do not account for interactions with recrystallized grains. A more detailed discussion on the models in these two groups can be found in the review articles by Miodownik [48] and Raabe [49].

As an alternative to the aforementioned approaches, a new theory, strain energy release maximization (SERM) theory, correlating the history of deformation to the stable orientation of recrystallized nuclei has been proposed. [14,50,51] The SERM theory postulates that recrystallized grains are nucleated with orientations that maximize the strain energy released from the deformed grains. This theory has been employed to predict the recrystallization texture of Ti bearing IF steels [52], aluminum and copper [53], low carbon steels [54], grain-oriented electrical steels [55], non-grain

oriented electrical steels [56], and aluminum containing high-manganese austenitic steels [57]. However, the calculations involved only specific loading conditions with well-defined limited slip activities. To address this limitation, Min et al. [4] modified the theory to make it consistent with the results of CPFEM, resulting in the generalized SERM (GSERM) theory. They used the GSERM theory to predict the recrystallization behavior, including recrystallization texture, and resultant mechanical anisotropy of low carbon steel using an integrated CP–PF model.

1.3. Research objective

In this study, a novel multi-scale approach that integrates CPFEM and PFM (hereafter, integrated CP-PF model) is proposed and employed to simulate thermo-mechanical process typically involved in steel sheets manufacturing. CPFEM calculates local deformation heterogeneities induced by mechanical constraints during the cold rolling, including multiple slip activities, deformation texture, and corresponding dislocation density (or stored energy) distributions in the deformed polycrystal aggregates. The state variables, such as crystallographic orientations and stored energy distribution, are automatically transferred to the PFM by the proposed mapping algorithm. The annealing process is simulated by the PFM, accounting for the reduction of stored energy through the recovery process, nucleation of grains based on the nucleation criterion, and grain growth driven by both stored energy differences and misorientation between neighboring grains, making the formulation more realistic. For accurate prediction of the recrystallization texture during annealing, an analytical recrystallization texture model is revisited and further generalized based on the release of strain energy as a driving force under multiple dislocation pileups, termed the GSERM theory. To enhance the prediction accuracy of the recrystallization texture during annealing, the PF model needs to be coupled with the GSERM model, enabling the simulation of recovery, recrystallization, and grain growth

systematically within the proposed multiscale numerical scheme. More details of the integrated CP-PF model are provided in Chapter 2.

In Chapter 3, the static recrystallization of ultra-low carbon steel is represented using the proposed integrated CP-PF model. Ultra-low carbon steel that has undergone cold rolling followed by annealing, and subsequently fully recrystallized, exhibits a unique recrystallization texture and resulting anisotropic mechanical properties. The virtual microstructure, obtained from the proposed integrated CP-PF model, is used to construct representative volume elements (RVEs) for virtual mechanical tests. Orientation-dependent tensile tests are performed to predict the anisotropic mechanical properties, which are validated by comparison with experimentally measured anisotropy in terms of r-values (Lankford coefficients) and flow stresses. Subsequently, forming limit diagrams (FLDs) are predicted to evaluate sheet formability based on the Marciniak-Kuczynski (M-K) model [58], which assumes an initial imperfection on the material surface leading to the final localized plastic instability under various loading stress, ranging from shear to a balanced biaxial stress state. In addition to conventional continuum-based FLD calculations, a hybrid approach [59] that integrates CPFE and the M-K model is also employed and compared with experimental data for validation purposes.

In Chapter 4, the origin of Goss{110}<001> during the primary

recrystallization of grain-oriented (GO) electrical steel is investigated using the proposed integrated CP-PF model. Both experimental and numerical schemes are employed to represent nucleation at the early stage of primary recrystallization. The hot-rolled test specimen undergoes severe plastic deformation followed by a short and low heat treatment. Texture evolutions at each step are characterized using various experimental methods. To complement the experimental findings, the experimental process is simulated numerically. In this chapter, CPFEM is extended to consider that plastic deformation during cold rolling can originate not only from dislocation slips but also from shear band formations. Rolling texture, dislocation evolution, crystallographic orientations at which shear bands are activated, and the role of shear bands as preferred nucleation sites are discussed. The GSERM theory, coupled with PFM, is applied to predict the recrystallized microstructure of GO electrical steel based on the results of CPFEM. The relationship between the main texture components that determine the characteristics of GO electrical steel and shear bands is examined.

The developed hierarchical numerical model integrates the grain-level FEM and PFM, which can be useful for gaining a deeper understanding of the relationship between the thermo-mechanical processes, microstructure evolution, and mechanical properties.

2. Integrated crystal plasticity and phase field model

2.1. Multi-scale approach: an overview

The aim of this study is to develop numerical simulation models to investigate the effects of thermo-mechanical processing on the microstructure and resulting mechanical properties of polycrystalline metals. To achieve this, we propose a multi-scale approach that integrates CPFEM and PFM. The CPFEM offers information on inhomogeneous local deformation and orientation distribution (or deformation texture) of polycrystalline metals as the mechanical aspect of the simulation. In contrast, the PFM accounts for microstructure evolution resulting from nucleation and growth, which is calculated based on local effects obtained from the mechanical simulation. The predicted microstructural information after the thermo-mechanical process can serve as input for predicting mechanical properties of the final product by applying the CPFEM as well, known as virtual mechanical testing [60]. The proposed numerical approach can also be a valuable tool for understanding local material responses during deformation and heat treatment, which are unattainable through conventional phenomenological numerical simulations and experiments.

The proposed multi-scale approach, based on integrated CPFEM and PFM simulations, consists of the following four steps, summarized step-by-

step with main inputs and outputs at each stage:

Step 1. CP simulation for mechanical loading: Boundary value problems are addressed using FE simulation that incorporates crystal plasticity constitutive laws. Instead of realistic boundary conditions of cold rolling, which include contact between tools and workpieces, a simpler RVE approach is employed for computational efficiency while maintaining reproducible microstructure features. In this step, local deformation inhomogeneities such as crystallographic orientations (rolling texture), slip activities, and dislocation densities (or stored energy) are calculated from single crystal properties, orientations, and grain sizes.

Step 2. Numerical mapping to connect CPFEM and PFM: Due to differences in discretization methods between FEM and PFM, which is based on the finite difference method (FDM), suitable numerical mapping must be introduced to transfer state variables between the two models. The orientation and stored energy distributions calculated in the first step are transferred to the PFM using either a direct or weighted method. A second mapping is performed from the predicted microstructure to the RVE model for virtual mechanical testing, transferring updated single crystal properties, orientations, and grain sizes to the integration points of FE model.

Step 3. PF simulations for microstructure evolution: Using the mapped state variables of the FE integration points, multi-phase field simulations

[61,62] are carried out to compute grain boundary migration in static recrystallization (SRX). Grain boundary characteristics, such as grain boundary energy and mobility, serve as primary inputs for this step.

Step 4. CP simulations for virtual mechanical testing: In this step, various mechanical tests can be virtually conducted using the calculated microstructure information, such as updated grain size, crystallographic orientations, and mechanical properties. The focus of this step is on the evaluation of anisotropy and formability of thermo-mechanically processed sheet metals. For validation purposes, anisotropy, including r-values and flow stresses along different material orientations, and formability, represented by FLD, are calculated and compared with experimental results.

In addition to these main steps, two complementary steps for PF simulations are emphasized during the primary Step 3:

Step 3-1. Calculation of recrystallization texture: Dislocation densities in activated slip systems and the orientation of each grain, determined from the mechanical simulation step, are utilized to analyze the orientations of the newly recrystallized nucleus, i.e., recrystallization texture. In this study, strain energy release maximization (SERM) theory proposed by Lee [14,50,51] is expanded to accommodate the general multi-axial stress state and cubic crystals, resulting in the generalized SERM (GSERM) [4].

Step 3-2. Nucleation Criterion: The nucleation criterion is formulated by taking into account the grain boundary mobility and stored energy, using empirical expressions from Humphreys and Hatherly [8] and Zurob et al. [63] to reproduce the nucleation step.

A summary flow chart illustrating the proposed multi-scale simulation procedure can be found in Fig. 2.1.

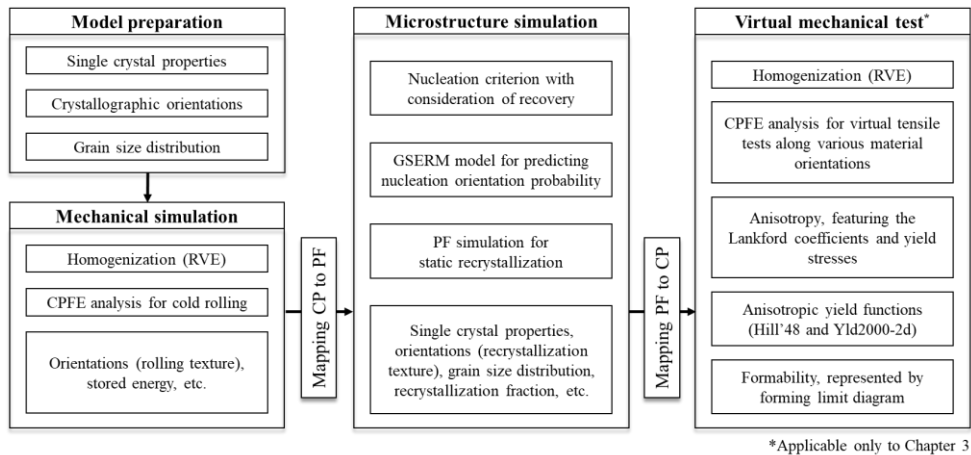


Fig. 2-1. Overall flow chart of the integrated CP-PF approach.

2.2. Crystal plasticity finite element model

In this section, the constitutive formulation of the CP model is briefly presented. The model is based on rate-dependent viscoplasticity with large deformation kinematics [21]. However, unlike the plastic deformation in the conventional CP model, that in the developed CP model is assumed to originate from dislocation slips on predefined slip systems and non-crystallographic shear bands of cubic crystals.

2.2.1. Kinematics

The deformation gradient tensor can be multiplicatively decomposed into its elastic \mathbf{F}^e and plastic \mathbf{F}^p components as follows:

$$\mathbf{F} = \mathbf{F}^e \mathbf{F}^p. \quad (2.1)$$

The stress and strain are related by the following equation based on the generalized Hooke's law with reference to an undeformed configuration.

$$\mathbf{S}^e = \mathbf{C}^e : \mathbf{E}^e \quad (2.2)$$

with

$$\mathbf{S}^e = \mathbf{F}^{e^{-1}} \left\{ (\det \mathbf{F}^e) \mathbf{S} \right\} \mathbf{F}^{e^{-T}} \quad (2.3)$$

and

$$\mathbf{E}^e = \frac{1}{2}(\mathbf{F}^{eT} \mathbf{F}^e - \mathbf{I}) \quad (2.4)$$

where \mathbf{E}^e is the Lagrangian strain tensor, \mathbf{S}^e is the second Piola-Kirchhoff stress tensor, \mathbf{C}^e is the fourth order stiffness tensor, and \mathbf{S} is the symmetric Cauchy stress tensor.

The rate of plastic deformation gradient is given by the following flow rule:

$$\dot{\mathbf{F}}^p = \mathbf{L}^p \mathbf{F}^p \quad (2.5)$$

where \mathbf{L}^p is the plastic velocity gradient.

In this study, the plastic deformation can be originated by both dislocation slips and shear band formation, thus the plastic velocity gradient can be expressed as follows [64,65]:

$$\mathbf{L}^p = \sum_{\alpha=1}^N \dot{\gamma}^{\alpha} \mathbf{m}_0^{\alpha} \otimes \mathbf{n}_0^{\alpha} + \sum_{\chi=1}^6 \dot{\gamma}^{\chi} \mathbf{m}^{\chi} \otimes \mathbf{n}^{\chi} \quad (2.6)$$

where the first and second terms on the right represent the contribution made by dislocation slips and shear band formation, respectively. For the dislocation slip, total 24 slip systems (N=24) consisting of 12{110}<111> and 12{112}<111> slip systems were prescribed for body-centered cubic (BCC) crystal structure. In the above equation, α and χ denote the slip system and shear band system, respectively. $\dot{\gamma}$ is the plastic shear strain rate. \mathbf{m} and \mathbf{n}

are orthonormal bases representing the slip (or shear band) plane and its normal direction, respectively. The detailed description of the dislocation slips and shear band formations are presented in Sections 2.2.2 and 2.2.3, respectively.

2.2.2. Dislocation density evolution during plastic deformation

In this study, the idealized dislocation loop comprising discrete edge and screw dislocations, proposed by Arsenlis and Parks [26] was adopted. The line vector of an edge dislocation is perpendicular to the Burgers vector (or the slip direction \mathbf{m}), while its screw dislocation component is parallel to the Burgers vector. For a slip system α , the total dislocation density is the sum of the two dislocation densities as given in Eq. (2.7):

$$\rho^\alpha = \rho_{edge}^\alpha + \rho_{screw}^\alpha \quad (2.7)$$

where ρ_{edge} and ρ_{screw} are the edge and screw dislocation components, respectively. By assuming that the dislocations in different slip systems have identical interaction strengths, the densities of the forest and parallel dislocation densities in the slip system α can be expressed as follows:

$$\rho_F^\alpha = \sum_\beta [\rho_{edge}^\alpha |\cos(\mathbf{n}^\alpha, \mathbf{n}^\beta \times \mathbf{m}^\beta)| + \rho_{screw}^\alpha |\cos(\mathbf{n}^\alpha, \mathbf{m}^\beta)|] \quad (2.8)$$

$$\rho_P^\alpha = \sum_\beta [\rho_{edge}^\alpha |\sin(\mathbf{n}^\alpha, \mathbf{n}^\beta \times \mathbf{m}^\beta)| + \rho_{screw}^\alpha |\sin(\mathbf{n}^\alpha, \mathbf{m}^\beta)|]. \quad (2.9)$$

The forest dislocations ρ_F^α have line vectors parallel to \mathbf{n}^α , while the parallel dislocations ρ_p^α are perpendicular to \mathbf{n}^α .

The plastic flow caused by the dislocation slips follows the well-known Orowan equation in which the plastic shear strain rate $\dot{\gamma}^\alpha$ of the slip system α is assumed to be a function of mobile dislocation density ρ_{mobile}^α and average slip velocity v^α [24,25]:

$$\dot{\gamma}^\alpha = b\rho_{mobile,edge} v_{edge}^\alpha + b\rho_{mobile,screw} v_{screw}^\alpha. \quad (2.10)$$

If backward jumps are ignored, the average slip velocity v^α can be expressed as follows for the edge and screw dislocations as a function of thermally activated dislocation motion:

$$v_{edge}^\alpha = \frac{1}{2} \lambda^\alpha v_0 \exp \left\{ \left(-\frac{Q_0}{k_B T} \left(1 - \left(\frac{|\tau^\alpha| - \tau_{pass,edge}^\alpha}{\tau_{CRSS}^\alpha} \right) \right) \right) \right\} \quad (2.11)$$

$$v_{screw}^\alpha = \frac{1}{2} \lambda^\alpha v_0 \exp \left\{ \left(-\frac{Q_0}{k_B T} \left(1 - \left(\frac{|\tau^\alpha| - \tau_{pass,screw}^\alpha}{\tau_{CRSS}^\alpha} \right) \right) \right) \right\} \quad (2.12)$$

with

$$\tau_{pass,edge}^\alpha = \frac{c_1 G b}{2\pi(1-\nu)} \sqrt{\rho_{P,edge}^\alpha + \rho_{mobile,edge}^\alpha} \approx \frac{c_1 G b}{2\pi(1-\nu)} \sqrt{\rho_{P,edge}^\alpha} \quad (2.13)$$

$$\tau_{pass,screw}^{\alpha} = \frac{c_1 G b}{2\pi} \sqrt{\rho_{P,screw}^{\alpha} + \rho_{mobile,screw}^{\alpha}} \approx \frac{c_1 G b}{2\pi} \sqrt{\rho_{P,screw}^{\alpha}} \quad (2.14)$$

where c_1 is a material constant, G is the shear modulus, b is the magnitude of the Burgers vector, ν is Poisson's ratio, λ^{α} is the jump width, ν_0 is the attack frequency, Q_0 is the activation energy, k_B is the Boltzmann constant, and T is the temperature. Further, τ_{pass}^{α} denotes the athermal passing stress caused by mobile dislocations. Because ρ_{mobile}^{α} was reported to be one (or more) order less than ρ_p^{α} [24], the passing stresses can be considered the last terms of the above equations. The resolved shear stress τ^{α} can be approximated as:

$$\tau^{\alpha} \approx \mathbf{S}^e : (\mathbf{m}_0^{\alpha} \otimes \mathbf{n}_0^{\alpha}) \quad (2.15)$$

and λ^{α} can be defined as a function of ρ_F^{α} as follows:

$$\lambda^{\alpha} = \frac{c_2}{\sqrt{\rho_F^{\alpha}}} \quad (2.16)$$

where c_2 is a material constant. The critical resolved shear stress τ_{CRSS}^{α} is defined to account for the contributions made by work hardening τ_{work}^{α} and grain boundary hardening τ_{gb}^{α} . The solid solution hardening τ_{ss}^{α} was also included in the model to account for the effects of silicon atoms in GO

electrical steel [66,67].

$$\begin{aligned}\tau_{CRSS}^{\alpha} &= \tau_{work}^{\alpha} + \tau_{0,gb}^{\alpha} + \tau_{0,ss}^{\alpha} \\ &= \frac{Q_0}{c_2 c_3 b^2} \sqrt{\rho_F^{\alpha}} + GH^{\alpha} \sqrt{\frac{b}{d_g}} + \sqrt{2GC}^{1/2} (\cos \theta_c)^{3/2}\end{aligned}\quad (2.17)$$

where c_3 is a material constant, H^{α} is the Hall-Petch coefficient, d_g is the average grain diameter, C is the solute atom concentration, and θ_c is the critical breakaway angle of the dislocations.

Following the work of Ma and Roters [24], a scaling relationship, which assumes that a given external stress generates the maximum plastic deformation, can be employed as a constraint for ρ_{mobile}^{α} :

$$\left(\frac{\partial \dot{\gamma}^{\alpha}}{\partial \rho_{mobile}^{\alpha}} \right)_{\tau^{\alpha}, \rho_F^{\alpha}, \rho_P^{\alpha}, T} = 0. \quad (2.18)$$

By combining Eqs. (2.10) and (2.18), ρ_{mobile}^{α} for edge and screw dislocations can be derived as follows:

$$\rho_{mobile,edge}^{\alpha} = \frac{2(1-\nu)k_B T}{c_1 c_2 c_3 G b^3} \sqrt{\rho_{P,edge}^{\alpha} \rho_F^{\alpha}} \quad (2.19)$$

$$\rho_{mobile,screw}^{\alpha} = \frac{2k_B T}{c_1 c_2 c_3 G b^3} \sqrt{\rho_{P,screw}^{\alpha} \rho_F^{\alpha}}. \quad (2.20)$$

Finally, the evolution of edge and screw dislocation densities are defined based on the idealized dislocation loop. The evolution of each dislocation

density comprises dislocation generation and dislocation annihilation terms (or athermal recovery) as follows:

$$\dot{\rho}_{edge}^{\alpha} = \frac{\sqrt{\rho_F^{\alpha}}}{c_4} \rho_{mobile,screw}^{\alpha} v_{screw}^{\alpha} - \frac{1}{2} \rho_{mobile,edge}^{\alpha} \rho_{edge}^{\alpha} R_{edge} v_{edge}^{\alpha} \quad (2.21)$$

$$\dot{\rho}_{screw}^{\alpha} = \frac{\sqrt{\rho_F^{\alpha}}}{c_5} \rho_{mobile,edge}^{\alpha} v_{edge}^{\alpha} - \frac{1}{2} \rho_{mobile,screw}^{\alpha} \rho_{screw}^{\alpha} R_{screw} v_{screw}^{\alpha} \quad (2.22)$$

where c_4 and c_5 are material constants and R_{edge} and R_{screw} are the critical radii of annihilation of edge and screw dislocations, respectively.

2.2.3. Plastic deformation due to shear band formation

In addition to the common dislocation density-based plastic flow, shear band formation, a mechanism responsible for local plasticity, is incorporated into the constitutive modeling scheme. Non-crystallographic plasticity has often been reported in metallic materials with severe deformation, such as cold-rolled materials with high thickness reduction ratios. The incorporation of the shear band formation mechanism was motivated by Anand and Su [68], Wei et al. [69], and Jia et al. [65], who originally proposed the mechanisms relevant to amorphous, nanocrystalline, and face-centered cubic metals, respectively. In this study, shear band formulation describes the non-crystallographic mechanical behavior of GO electrical steel with a BCC

crystal structure.

The main difference between dislocation slips and shear band mechanism is the dependency of the deformation system on the local stress state. Unlike the slip systems, which are predefined depending on the crystal structures and preferably selected based on crystal orientations and active loading conditions, active shear band formation and evolution depend on the principal directions of the stress state (denoted by \mathbf{S}^e in this paper). Therefore, local plasticity due to shear band formation is non-crystallographic and its actively system should be calculated during the increment of plastic deformation in the finite element simulation.

The spectral decomposition of \mathbf{S}^e can be expressed as follows:

$$\mathbf{S}^e = \sum_{i=1}^3 \sigma_i \hat{\mathbf{e}}_i \otimes \hat{\mathbf{e}}_i \quad (2.23)$$

where σ_i is the principal stresses and $\hat{\mathbf{e}}_i$ is the orthonormal principal basis of \mathbf{S}^e . From $\hat{\mathbf{e}}_i$ calculated at each loading step, six potential shear band systems in total can be defined as follows:

$$\begin{cases} \mathbf{m}^1 = \cos \mathcal{G}_{\hat{\mathbf{e}}_1} + \sin \mathcal{G}_{\hat{\mathbf{e}}_2}, & \mathbf{n}^1 = \sin \mathcal{G}_{\hat{\mathbf{e}}_1} - \cos \mathcal{G}_{\hat{\mathbf{e}}_2}, \\ \mathbf{m}^2 = \cos \mathcal{G}_{\hat{\mathbf{e}}_1} - \sin \mathcal{G}_{\hat{\mathbf{e}}_2}, & \mathbf{n}^2 = \sin \mathcal{G}_{\hat{\mathbf{e}}_1} + \cos \mathcal{G}_{\hat{\mathbf{e}}_2}, \\ \mathbf{m}^3 = \cos \mathcal{G}_{\hat{\mathbf{e}}_1} + \sin \mathcal{G}_{\hat{\mathbf{e}}_3}, & \mathbf{n}^3 = \sin \mathcal{G}_{\hat{\mathbf{e}}_1} - \cos \mathcal{G}_{\hat{\mathbf{e}}_3}, \\ \mathbf{m}^4 = \cos \mathcal{G}_{\hat{\mathbf{e}}_1} - \sin \mathcal{G}_{\hat{\mathbf{e}}_3}, & \mathbf{n}^4 = \sin \mathcal{G}_{\hat{\mathbf{e}}_1} + \cos \mathcal{G}_{\hat{\mathbf{e}}_3}, \\ \mathbf{m}^5 = \cos \mathcal{G}_{\hat{\mathbf{e}}_2} + \sin \mathcal{G}_{\hat{\mathbf{e}}_3}, & \mathbf{n}^5 = \sin \mathcal{G}_{\hat{\mathbf{e}}_2} - \cos \mathcal{G}_{\hat{\mathbf{e}}_3}, \\ \mathbf{m}^6 = \cos \mathcal{G}_{\hat{\mathbf{e}}_2} - \sin \mathcal{G}_{\hat{\mathbf{e}}_3}, & \mathbf{n}^6 = \sin \mathcal{G}_{\hat{\mathbf{e}}_2} + \cos \mathcal{G}_{\hat{\mathbf{e}}_3} \end{cases} \quad (2.24)$$

where \mathcal{G} is the angle between \mathbf{m}^χ and $\hat{\mathbf{e}}_1$ in the $(\hat{\mathbf{e}}_1, \hat{\mathbf{e}}_2)$ - and $(\hat{\mathbf{e}}_1, \hat{\mathbf{e}}_3)$ -plane or $\hat{\mathbf{e}}_2$ in the $(\hat{\mathbf{e}}_2, \hat{\mathbf{e}}_3)$ -plane. The resolved shear stress τ^χ and compressive normal traction σ^χ of the shear band system χ can be expressed as follows:

$$\tau^\chi(\mathcal{G}) = \mathbf{S}^e : (\mathbf{m}^\chi \otimes \mathbf{n}^\chi) \quad (2.25)$$

$$\sigma^\chi(\mathcal{G}) = -\mathbf{S}^e : (\mathbf{n}^\chi \otimes \mathbf{n}^\chi). \quad (2.26)$$

The internal friction angle θ and internal friction coefficient μ have the following relationship:

$$\theta = \arctan \mu. \quad (2.27)$$

Based on the Coulomb friction model, shearing is initiated on the shear band systems where the following function has attained its maximum value with respect to \mathcal{G} .

$$f(\mathcal{G}) = \left\{ \tau^\chi(\mathcal{G}) - (\tan \theta) \sigma^\chi(\mathcal{G}) \right\}. \quad (2.28)$$

The condition is satisfied or $\text{Max}(f(\mathcal{G}))$ under the following condition:

$$\vartheta = \frac{\pi}{4} + \frac{\theta}{2}. \quad (2.29)$$

Plastic incompressibility in metallic materials, such as GO electrical steel investigated in this study, can be assumed or $\det(\mathbf{F}^p) = 1$. Therefore, the effect of shear-induced plastic dilatancy can be ignored.

Finally, the flow rule for the shear bands can be formulated as done for the dislocation slips.

$$\dot{\gamma}^\lambda = \dot{\gamma}_0^\lambda \exp \left\{ \left(-\frac{Q_0}{k_b T} \left(1 - \left(\frac{\tau^\lambda}{\tau_0^\lambda + \mu \sigma^\lambda} \right) \right) \right) \right\} \text{sign}(\tau^\lambda) \quad (2.30)$$

where $\dot{\gamma}_0^\lambda$ is the reference shear rate of shear band and τ_0^λ is the constant resistance that activates shear bands.

2.2.4. Numerical implementation

The CP model was formulated using the user material subroutine UMAT provided in Abaqus/Standard, a commercial software package that can be used in implicit finite element analysis. The numerical scheme particularly introduced a two-step implicit stress integration algorithm based on the mixed Newton-Raphson and incremental methods that can be used for updating the stress tensor and plastic hardening by dislocations and shear bands,

respectively. The procedure used for time integration with analytically derived Jacobian matrix are presented in Appendix A.

2.2.5. Representative microstructure model and periodic boundary conditions

The representative volume element (RVE) approach was adopted to simulate the mechanical response of the polycrystalline metals. The microstructural characteristics of materials to be simulated were statistically analyzed. The crystallographic orientations and grain sizes were thereafter distributed in the RVE using DREAM.3D [70]. The 8-node continuum element with a reduced integration (C3D8R) provided in ABAQUS/Standard was used for meshing the RVE in which each element represented a single grain with an orientation appropriate for capturing intra-granular features at a high resolution.

Periodic boundary conditions (PBCs) were applied to the RVE by linearly constraining two equivalent nodes (a and b) located on the opposite planes perpendicular to the j -direction (i.e. $x_i^a = x_i^b$ for $i \neq j$) in their displacement along the j -direction:

$$u_i^b - u_i^a = L_0^j (F_{ij} - \delta_{ij}) \quad (2.31)$$

where u_i^a and u_i^b are the displacements of nodes a and b along the i -direction,

L_0^j is the initial RVE size along the j-direction, and δ_{ij} is the Kronecker delta.

The PBCs ensures that the RVE unit cell behaves as a physically continuous domain [59]. These equations can be implemented using the linear multi-point constraints option in Abaqus/Standard.

2.3. Multi-phase field model

The multi-phase field model proposed by Steinbach and Pezzolla [61] is employed for simulations of grain growth during static recrystallization. In the following, the summary of the PFM is briefly introduced, whereas details on the model are provided in the studies of Kim et al. [62] and Kim and Park [71].

2.3.1. Phase field equation

For polycrystalline metals with Q crystals (or grains), a phase field ϕ_p is defined for the p -th grain. Each phase field has values between 0 and 1; 0 for outside of the grain (or interior of other grains), 1 for the grain interior, and between 0 and 1 for the grain boundary. A constraint for the phase field values is that the sum of these in a grid point should be 1, or $\sum_{p=1}^Q \phi_p = 1$.

A free energy functional F is defined in the model as follows:

$$F = \int_{\Omega} \left(f^e + \sum_{p>q}^Q \sum_q^Q -\frac{a_{pq}^2}{2} \nabla \phi_p \cdot \nabla \phi_q + \omega_{pq} \phi_p \phi_q \right) d\Omega \quad (2.32)$$

where f^e is the free energy density of grains, a and w are the coefficients of gradient energy and height of the potential, respectively, of the interfacial

energy term. The following phase field equation is suggested by Steinbach and Pezzolla [61]:

$$\frac{\partial \phi_p}{\partial t} = -\frac{2}{S} \sum_{q \neq p}^Q s_p s_q M_{pq}^\phi \left(\frac{\partial F}{\partial \phi_p} - \frac{\partial F}{\partial \phi_q} \right) \quad (2.33)$$

where $S = S(\mathbf{x}, t) = \sum_{p=1}^Q s_p$ is the number of co-existing phase fields at a grid,

$s_p = s_p(\mathbf{x}, t)$ is a step function with a value of 1 for $\phi_p > 0$ and 0 for $\phi_p = 0$,

and M_{pq}^ϕ is the phase field mobility.

From the derivative of Eq. (2.32) to ϕ_p ,

$$\frac{\partial F}{\partial \phi_p} = \sum_{r \neq p}^Q \left(\nabla \cdot \frac{a_{pr}^2}{2} \nabla \phi_r + \omega_{pr} \phi_r \right) + \frac{\partial f^e}{\partial \phi_p}. \quad (2.34)$$

Then, Eq. (2.33) and (2.34) lead to

$$\frac{\partial \phi_p}{\partial t} = -\frac{2}{S} \sum_{q \neq p}^Q s_p s_q M_{pq}^\phi \left[\left\{ \sum_{r \neq p, q}^Q \left(\frac{a_{pr}^2 - a_{qr}^2}{2} \right) \nabla^2 \phi_r + (\omega_{pr} - \omega_{qr}) \phi_r \right\} + \frac{8}{\pi} \sqrt{\phi_p \phi_q} \Delta E_{store, pq} \right] \quad (2.35)$$

where a relationship $\left(\frac{\partial f^e}{\partial \phi_p} - \frac{\partial f^e}{\partial \phi_q} \right) = \frac{8}{\pi} \sqrt{\phi_p \phi_q} \Delta E_{store, pq}$ is used by referring to

the work by Takaki et al. [72–74] to consider the effect of stored energy ΔE_{store} as the major driving force in static recrystallization. The difference in

the stored energy can be calculated from the CPFEM results.

$$\Delta E_{store,pq} = \alpha G b^2 (\rho_p - \rho_q) \quad (2.36)$$

with [75]

$$G = G^0 \left(1 - 1.31 \left(\frac{T - 300}{1810} \right) \right) \quad (2.37)$$

where G^0 is the shear modulus at room temperature, T is the temperature in Kelvin, α is a material constant, and ρ_p is the dislocation density in the p -th grain.

2.3.2. Grain boundary anisotropy

In the model, the recrystallization process is assumed to be thermodynamically uniform, except for the anisotropy of grain boundaries. The grain boundary energy and mobility are known to be dependent variables, related to the boundary characteristics. However, for the sake of model simplicity, the properties of boundaries are assumed to depend only on grain misorientation, and thus, the Read–Shockley [76] relationship is used to relate boundary energy and mobility to the misorientation. This has been valid in the literature from the empirical relationship obtained from experimental data [77].

The energy of the grain boundary γ_{pq} is given as follows:

$$\gamma_{pq} = \gamma_{pq}^0 f_\gamma(\Delta\theta) \quad (2.38)$$

with

$$f_\gamma(\Delta\theta) = \begin{cases} \frac{\Delta\theta}{\theta_{c,\Delta\theta}} \left(1 - \ln \frac{\Delta\theta}{\theta_{c,\Delta\theta}} \right) & \text{if } \Delta\theta < \theta_{c,\Delta\theta} \\ 1 & \text{if } \Delta\theta \geq \theta_{c,\Delta\theta} \end{cases} \quad (2.39)$$

where $\Delta\theta$ depicts the misorientation between grains, γ_{pq}^0 is the energy of the high angle grain boundary (HAGB) with the misorientation angle larger than a critical value $\theta_{c,\Delta\theta}$. In this study, $\theta_{c,\Delta\theta}$ is 15° . The mobility of the grain boundary can also be expressed as the Read-Shockley equation using the empirical relationship derived from the work of Humphreys [77]:

$$m_{pq} = m_{pq}^0 f_m(\Delta\theta) \quad (2.40)$$

with

$$f_m(\Delta\theta) = \begin{cases} 1 - \exp\left(-C_B \left(\frac{\Delta\theta}{\theta_{c,\Delta\theta}}\right)^{C_A}\right) & \text{if } \Delta\theta < \theta_{c,\Delta\theta} \\ 1 & \text{if } \Delta\theta \geq \theta_{c,\Delta\theta} \end{cases} \quad (2.41)$$

where m_{pq}^0 depicts the mobility of the HAGB. Constants $C_A = 4$ and $C_B = 5$ are chosen from the reference [8,77].

2.3.3. Parameters in phase field equation

To complete the phase field equations, the following parameters for a , M^ϕ , and ω in Eq. (2.35) are used to consider the anisotropic properties of grain boundaries.

$$a_{pq} = \frac{4}{\pi} \sqrt{\xi_{pq}^0 \gamma_{pq}^0} f_\gamma(\Delta\theta) \quad (2.42)$$

$$M_{pq}^\phi = \frac{\pi^2 m_{pq}^0 f_m(\Delta\theta)}{16 \xi_{pq}^0 f_\gamma(\Delta\theta)} \quad (2.43)$$

$$\omega_{pq} = 2 \frac{\gamma_{pq}^0}{\xi_{pq}^0} \quad (2.44)$$

where $\xi_{pq}^0 = \frac{\xi}{f_\gamma(\Delta\theta)}$ is a grain boundary thickness. All parameters with a superscript '0', except m_{pq}^0 , are inputs to PF simulations corresponding to the properties of HAGBs. For the grain boundary mobility, the Arrhenius type relationship was suggested.

$$m_{pq}^0 = c^m \exp\left(-\frac{Q_0^m}{RT}\right) \quad (2.45)$$

where c^m is a constant, Q_0^m is the activation energy, and R is a gas constant.

2.3.4. Numerical implementation

All the equations above for the multi-phase field model were implemented in the Intel Visual Fortran® program, which enables a numerical treatment for memory space management and efficient computation by restricting the number of phase fields at the grid [62].

2.4. Numerical mapping between CPFEM and PFM

In the proposed integrated numerical scheme, the state variables between the CPFEM and PFM need to be properly mapped. The challenge of this mapping arises due to different numerical schemes for the storage of state variables. In the FEM, they are stored in integration points, while for the PFM, they are stored in regularly spaced grids. Particularly, when the RVE model is discretized by continuum elements with reduced integration, it involves highly coarse meshes and distortions during the deformation. To address this issue, a Wigner-Seitz mapping algorithm [31,36,78] was employed in this study to avoid the high computational cost of the direct mapping algorithm.

In the Wigner-Seitz algorithm, regular grids are mapped onto the distorted FE meshes defined by the integration points. Construction of the Wigner-Seitz cell begins with triangulation by connecting neighboring integration points of FE meshes. In this step, no single integration point should exist in the circumcircle of each triangle. This step is referred to as Delaunay triangulation. Subsequently, the Wigner-Seitz cells are formed by connecting the centers of neighboring circumcircles. Fig. 2-2(a) shows a schematic illustration of the Wigner-Seitz mapping between the FE model and PF grids.

After constructing the Wigner-Seitz cells, state variables are mapped

differently. The grain orientations (with their grain indices) of individual integration points are assigned to the PF grids, which fall into the corresponding cells. In contrast, the stored energy (or dislocation density) of each grid point is mapped from the neighboring integration points by applying different weights, as shown in Fig. 2-2(b). The weights are inversely proportional to the distance between the target grid point and the integration point [78,79]. Hence,

$$E_{store,\mathbf{x}} = \sum_{k=1}^m \frac{E_k}{d_k} \bigg/ \sum_{k=1}^m \frac{1}{d_k} \quad (2.46)$$

where $E_{store,\mathbf{x}}$ is the mapped stored energy at a grid \mathbf{x} , d_k is the distance between the grid \mathbf{x} and integration point k , E_k is the stored energy at the integration point k , and m is the number of integration points in the mapping.

PF simulations have regular grids with periodic boundary conditions; thus, the results of CPFEM are consistently transferred to the PFM by considering the periodicity of the simulations. Moreover, when the deformation of the CPFE model is severe, the finite element meshes become distorted, and the distance between integration points is rather large, leading to distorted Wigner-Seitz cells. To tackle this numerical inefficiency, a regularization technique is applied by introducing virtual integration points

with the same orientations as the original integration points. An example of numerical regularization before the Wigner-Seitz mapping is shown in Fig. 2-3.

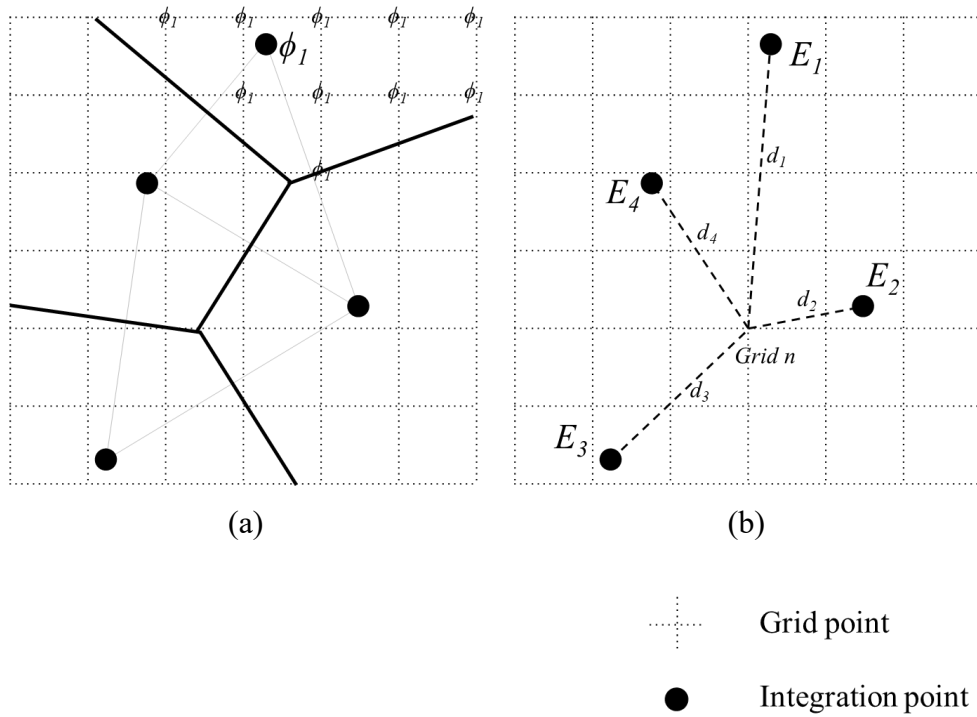


Fig. 2-2. Schematic illustrations of the numerical mapping for (a) grain orientations using Wigner-Seitz cell and (b) stored energy.

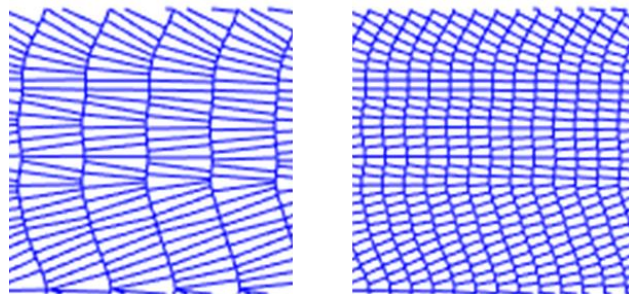


Fig. 2-3. Regularization of coarse integration points by introducing virtual integration points during the Wigner-Seitz mapping.

2.5. Nucleation modeling with consideration of recovery

The quantitative nucleation model for recrystallization, originally proposed by Bailey and Hirsch [80] and later extended by Zurob et al. [63], was utilized in this study. Zurob et al. expanded the strain-induced boundary migration (SIBM) model by factoring in the effect of subgrain growth and recovery on capillary force and stored energy. According to the SIBM theory, the critical size of recrystallized nuclei is directly proportional to the grain boundary energy and inversely proportional to the stored energy:

$$r_c(t) = \frac{2\gamma}{E_{store}(t)} \quad (2.47)$$

where r_c , γ , and E_{store} are critical nuclei radius, grain boundary energy, and stored energy, respectively. Therefore, nucleation accelerates as the amount of stored energy increases sufficiently. In the model, a subgrain is considered a nucleus when its radius surpasses the critical radius, overcoming the capillary force. However, the critical radius expands over time due to the decrease in stored energy brought about by dislocation recovery. When the size of the nucleus is smaller than its critical radius, r_c , nucleation is postponed, and the growth of neighboring recrystallized grains consumes the matrix.

Numerous studies have reported that the recovery is a thermally

activated process that takes place with the gliding or cross-slip of dislocations [81–83]. Thus, the evolution equation of the internal stress σ_i is written as:

$$\frac{d\sigma_i}{dt} = -c_1^r \exp\left(\frac{-Q^r(\sigma_i)}{RT}\right) \quad (2.48)$$

where c_1^r is a material constant, and Q^r is the activation energy for recovery.

A linear decrease of activation energy with the internal stress is assumed:

$$Q^r(\sigma_i) = Q_0^r - c_2^r \sigma_i. \quad (2.49)$$

Then, Eq. (2.48) can be analytically solved as follows:

$$\sigma_i(t) = \sigma_{i,0} - \frac{RT}{c_2^r} \ln\left(1 + \frac{t}{t_0}\right) \quad (2.50)$$

with

$$t_0 = \frac{RT}{c_1^r c_2^r} \exp\left(\frac{Q_0^r - c_2^r \sigma_{i,0}}{RT}\right) \quad (2.51)$$

where Q_0^r is the intrinsic activation energy, $\sigma_{i,0}$ is the internal stress at $t = 0$, and c_2^r is a constant. At the early stage of recovery, the internal stress can be approximated as the following equation, if flow stress is developed by dislocations at the cell wall [8]:

$$\sigma_i(t) = \beta G b \sqrt{\rho(t)} \quad (2.52)$$

where β is a constant.

Lastly, the time-dependent evolution of stored energy can be acquired using Eqs. (2.36) and (2.50), as previously proposed by Song and Rettenmayr [84]:

$$E_{store}(t) = \left(\sqrt{E_0} - \frac{\sqrt{\alpha}RT}{c_2^r \beta \sqrt{G}} \ln \left(1 + \frac{t}{t_0} \right) \right)^2 \quad (2.53)$$

where E_0 is the stored energy at $t=0$. Eq. (2.53) links the stored energy with temperature and time during recovery, indicating a higher rate of recovery at the initial stage, which gradually decreases as the recrystallization process continues.

The growth rate of the subgrain is proportional to the boundary mobility and the stored energy [8,85,86], which leads to the following equation:

$$r(t) = r_0 + \int_0^t m^{sub} E_{store}(t) dt \quad (2.54)$$

where r_0 is the initial radius of the subgrain, and m^{sub} is the subgrain boundary mobility between the subgrain and surrounding grains, accounting for the misorientation effect. Therefore, the criterion for the subgrain nucleation becomes:

$$r(t) \geq r_c(t) . \quad (2.55)$$

The time before this criterion is met is referred to as the incubation time. The aforementioned nucleation models for recrystallization are incorporated into the current PF model.

2.6. Strain energy release maximization model and its generalization

The prediction of the orientations of newly nucleated grains or recrystallization texture has been a significant challenge during the simulation of recrystallization process. Although several models have already been formulated for this prediction, the SERM model, originally proposed by Lee [14,50,51] and subsequently modified for consistency with the CP model [4], called GSERM model, was employed in this study. The GSERM model suggests that the orientations of the nuclei are determined by the need to release the maximum amount of strain energy accumulated during deformation. This is achieved by aligning the absolute maximum stress direction (AMSD), which is characterized by the dislocation stress fields of the deformed grains, parallel to the minimum Young's modulus direction (MYMD) of the recrystallized grains.

Fig. 2-4 schematically illustrates how a partially recrystallized metallic bar under uniaxial tension releases maximum strain energy [14]. Note that the recrystallization process is assumed to induce no volume change. When a specimen is elastically elongated and is partially replaced by a stress-free volume (i.e., recrystallized volume), the strain energy changes schematically from ΔABD to ΔACD . These correspond to the elongated bar (Fig. 2-4, state B) and the partially recrystallized bar (Fig. 2-4, state C), respectively. The strain energy released (ΔABC) is at its maximum when ΔABD is maximized

and ΔACD is minimized, which correspond to the AMSD and MYMD in a one-dimensional analogy, respectively.

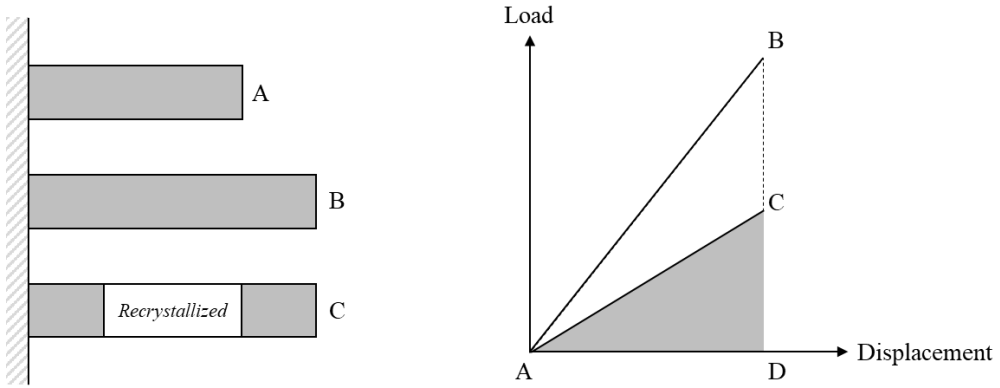


Fig. 2-4. Schematic illustrations of the SERM model in 1-D analogy [14].

In general stress state, the strain energy released per unit volume can be expressed as follows:

$$\Delta E_{release} = \int (\mathbf{S}_{def} - \mathbf{S}_{rex}) : d\mathbf{E} = \int (\mathbf{S}_{def} - \mathbf{C}_{rex}^e : \mathbf{E}) : d\mathbf{E} \quad (2.56)$$

where \mathbf{E} is the strain tensor. Subscripts def and rex in Eq. (2.56) denote the “deformed” and “recrystallized” grains, respectively. In the equation, the strain energy released (per unit volume) can be close to its maximum value as the principal stress component of the Cauchy stress tensor of the deformed grains (\mathbf{S}_{def}) increases (in absolute value), while that of the recrystallized

grains (\mathbf{S}_{rex}) decreases. Therefore, the identification of the directions along which the principal stress becomes maximum and minimum is important. This corresponds to the eigenvector calculated through the spectral decomposition of the stress tensor.

The recrystallization process involves the formation of strain-free grains without any change in their volumes [8,14]. It's noted that the direction along which the Cauchy stress tensor of the recrystallized grains (\mathbf{S}_{rex}) is minimized coincides with the direction along which the stiffness tensor of the recrystallized grains (\mathbf{C}_{rex}^e) is minimized. In the case of the materials studied in this work, such as ultra-low carbon steel and GO electrical steel, MYMD, is found to be $\langle 100 \rangle$ [87,88].

Unlike the MYMD, the AMSD is strongly dependent on the internal stress field produced by the stored energy during deformation. The difference between the stored energy of the deformed state and that of the recrystallized state results from dislocations and their arrangements [8]. The internal stress field of the deformed grains can be approximated to the superposition of the stress field induced by the dislocation arrangement on the active slip systems.

Screw dislocations contribute a symmetric stress field around the center of the dislocation [89–91]. Moreover, their densities are known to be approximately an order of magnitude less than those of edge dislocations after

severe plastic deformation including cold rolling [92,93]. This discrepancy is likely attributable to the enhanced active recovery (or annihilation) process of screw dislocations, facilitated by cross slips. Consequently, in the case of texture evolution, only edge dislocation component was considered when calculating the dislocation arrangement.

Sutton and Balluffi [94] calculated the stress field of equally spaced and infinitely arrayed edge dislocations and showed that the direction of the absolute maximum principal stress is parallel to the slip direction. This proof, accomplished through numerical analysis, is presented in Appendix B. In activated multiple slip systems, the effective slip direction (ESD, $\bar{\mathbf{m}}$) can be defined as follows:

$$\bar{\mathbf{m}} = \sum_{\alpha=1}^N \rho_{edge}^{\alpha} \mathbf{m}_0^{\alpha} \quad (2.57)$$

where ρ_{edge}^{α} is the weighting factor of the effective slip direction. The AMSD of the deformed grains can then be assumed to be parallel to the effective slip direction.

Using the calculated ESD at each integration point of the FE mesh, as defined in Eq. (2.57), the rotation matrix relating the ESD and MYMD can be determined. This rotation matrix facilitates the calculation of the recrystallization orientation from the deformation orientation, as computed

using CPFEM. Fig. 2-5 schematically presents the procedure utilized to calculate the orientation of recrystallized grain. The primary challenge in this process is the selection of the ESD, which varies depending on the case for both face-centered cubic (FCC) and BCC crystal structures.

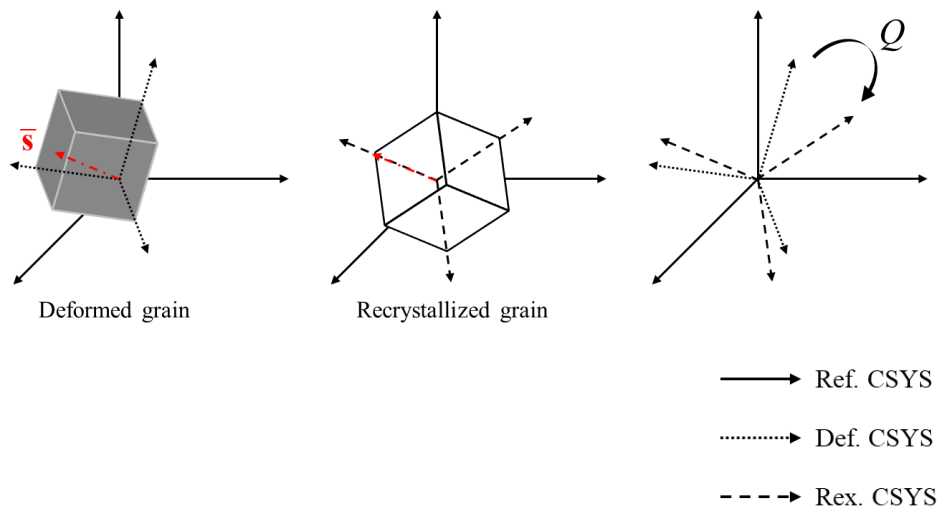


Fig. 2-5. Schematic diagram for predicting recrystallization orientation from deformation orientation using GSERM model.

FCC crystals possess well-defined potential slip systems of $\{111\}\langle 110\rangle$, and the ESD is ascertained from the activations of preferred slip systems and their respective edge dislocation densities, using Eq. (2.57). Consequently, the procedure detailed in Lee [14,51] is initially applied to the FCC crystal to

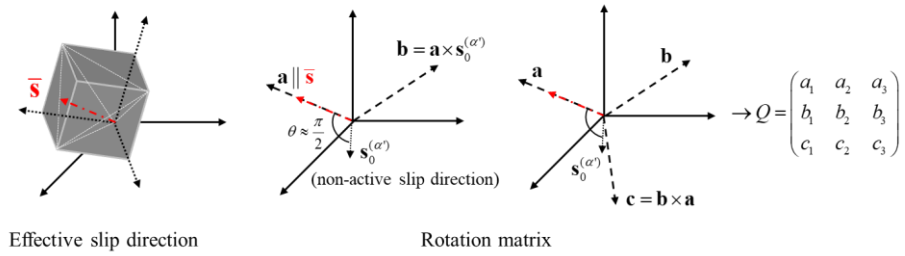
determine the rotation matrix. Upon the determination of the ESD, the angle between the ESD and each non-active slip direction is examined. If the slip direction vector approximates orthogonality with the ESD vector within a predetermined tolerance ($\pm 5^\circ$ in this study), it is chosen as the rotation axis of the ESD. The degree of rotation required to align with the MYMD can be easily obtained from the cross-product of the two vectors. Fig. 2-6(a) visually depicts the complete process for determining the rotation matrix.

In contrast to the FCC case, BCC crystals have the slip plane normals of the slip systems that share a common $\langle 111 \rangle$ slip direction, leading to the phenomenon known as pencil glide. As a result, multiple ESDs can be calculated using Eq. (2.57). To address the non-unique problem of ESD, Min et al. [4] proposed a variant selection rule by considering the direction of the virtual in-grain shear band and $\{110\}$ plane matching theory:

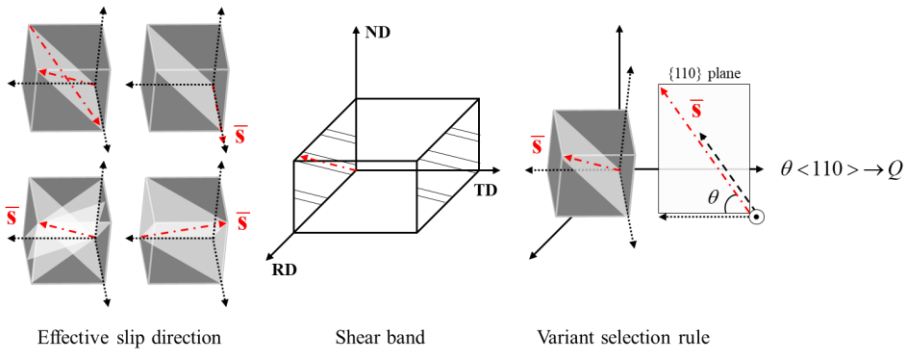
Virtual in-grain shear band: In the case of cold-rolled steels, significant in-grain shear bands form at an angle of 30° – 35° relative to the rolling direction (RD) [95]. Park et al. [91] pointed out that shear bands were closely associated with the movement and accumulation of dislocations in the active slip systems. Furthermore, they found that the in-grain shear bands are approximately co-linear with the direction of maximum internal stress of the deformed grains. Therefore, the known angle of the shear band was used as the criterion to determine ESD.

{110} plane matching theory: Urabe and Jonas [96] noted that the most active slip plane in such situations tends to be $\{110\}$, and the highly mobile grains exhibit rotational relationships along a common $\langle 110 \rangle$ axis. This observation aligns with the plane matching theory proposed by Watanabe [97]. Thus, the common $\{110\}$ plane (or the normal vector defining the plane) containing both ESD and MYMD is selected as the rotation axis.

In the variant selection rule, the typically observed shear band direction was utilized to determine the ESD, and the normal direction of $\{110\}$ plane containing both ESD and MYMD was selected as its rotation axis. A summary of the rotation scheme for determining the orientation of recrystallized grains in BCC crystals is depicted in Fig. 2-6(b).



(a)



(b)

- > Ref. CSYS
-> Def. CSYS
- - - -> Rex. CSYS

Fig. 2-6. Procedure to calculate recrystallized orientation by proposed ESD concepts for (a) FCC and (b) BCC crystals.

In this study, shear band formation is incorporated into the constitutive model to predict the evolution of shear bands formed during cold rolling. Therefore, when the shear bands are activated in specific regions, the ESD

can be directly determined by using Eq. (2.57), eliminating the need for any assumption. Effect of evolved shear bands on the recrystallization orientations is discussed in Section 4.3.3.

3. Application I: Virtual identification of anisotropy and formability for thermo-mechanically processed ultra-low carbon steel

3.1. Introduction

Low carbon steels are FeC alloys with a BCC structure where the carbon concentration is typically maintained below ~ 0.1 wt%. Ultra-low carbon steels, a subset of low carbon steels, have even lower carbon concentrations, typically less than ~ 0.02 wt% [98]. These steels find use in a variety of applications, both in their hot-rolled state and after further thermo-mechanical processing steps such as cold-rolling, annealing, and potentially coating. Modern processing techniques allow for a high degree of control over both the chemical composition and manufacturing processes of low carbon steel, enabling the production of a wide range of grades with varying combinations of strength and formability. Precise control of dimensions such as gauge, width, shape, and flatness is also achievable [99].

However, it is the formability of low carbon steel that ensures its continued prominence as a major engineering material. This material can be economically and satisfactorily formed into a wide array of complex shapes without issues such as splitting, necking, or wrinkling, which are common problems in the forming processes of other materials [99].

Sheet formability can be evaluated from two perspectives: drawability and stretchability. Drawability refers to the ability of the material to flow easily in the plane of the sheet and resist thinning in the thickness direction [100]. It is primarily characterized by sheet anisotropy, as measured by Lankford coefficients (r-values), and flow stresses. These parameters are significantly influenced by the developed crystallographic orientations that evolves during thermo-mechanical processes. In contrast, stretchability represents the capacity of the material to resist localized necking and consequently withstand complex non-uniform deformation. It is typically characterized by factors such as the strain hardening and strain rate hardening [101].

During the thermo-mechanical processes where SRX occurs, the crystallographic orientations of low carbon steel evolve. These orientations can be represented by two main characteristic fibers: α -fiber ($\langle 110 \rangle // RD$) and γ -fiber ($\{111\} // ND$, where ND stands for the normal direction). For instance, during the cold rolling process, α -fiber is predominantly developed, with only minor development of γ -fiber. However, during the subsequent annealing process, the γ -fiber becomes the primary component, providing unique anisotropic properties to low carbon steel. Simultaneously, cold-rolled low carbon steel, which has high stored energy due to dislocation accumulation during deformation, can recover its original strength and ductility by releasing

this stored energy through SRX, affecting material hardening. As both sheet anisotropy and material hardening are influenced by these microstructure evolutions, it is necessary to take them into account in any comprehensive evaluation of the formability of the thermo-mechanically processed low carbon steel.

In this chapter, a virtual identification scheme has been proposed as a complementary strategy to the conventional experiment-based approach, with the aim of predicting the anisotropy and formability of thermo-mechanically processed ultra-low carbon steel sheets. This scheme employs the proposed integrated CP-PF model, taking into consideration the effect of microstructural characteristics on the mechanical performance of the final product. Local inhomogeneities during cold rolling were predicted using the CPFEM, while the PFM was used to analyze microstructure evolution during the annealing process. Upon simulating the sheet manufacturing process of ultra-low carbon steel, RVE were generated. The RVE, which encompass deformation history and recrystallized microstructural data, served as the basis for evaluating sheet anisotropy and formability during the virtual experiments. Plastic anisotropy, characterized by r values and yield stresses, was predicted using virtual experiments and then compared with experimental values. Various anisotropic yield functions were identified based on the predicted anisotropic mechanical properties. When calculating

the FLD using the M-K model [58] to evaluate sheet formability, this chapter discussed not only the conventional approach using phenomenological anisotropic yield functions, but also a crystal plasticity-based approach [59] designed to consider texture evolution during deformation. Both approaches were quantitatively compared to provide a comprehensive understanding for evaluating formability. The anisotropy and formability predictions from these approaches were then validated experimentally, confirming the accuracy of the proposed integrated CP-PF model.

3.2. Experiments

3.2.1. Material

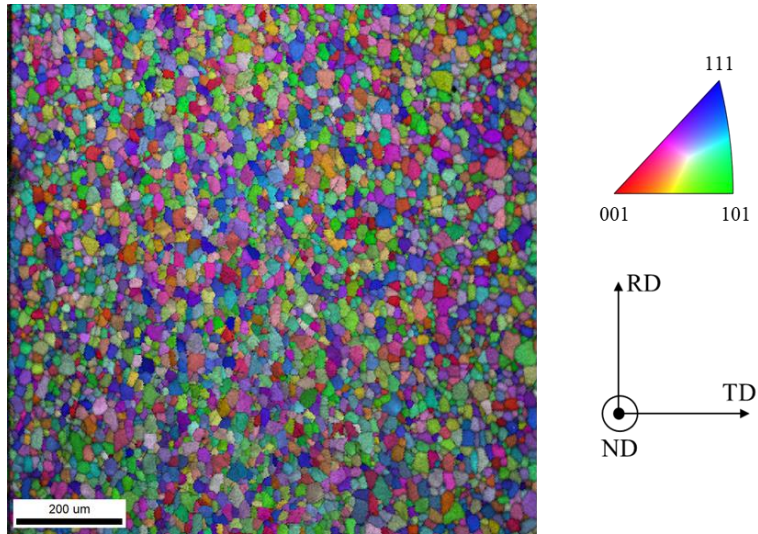
The material investigated in the chapter is a hot-rolled ultra-low carbon steel with a tensile strength of 350 MPa. Its thickness prior to cold rolling is 4.5 mm. The chemical composition of the steel is given in Table 3-1. The investigated steel features extremely low carbon for enhanced drawability and stretchability.

Table 3-1. Chemical compositions of the investigated ultra-low carbon steel sheet (weight %).

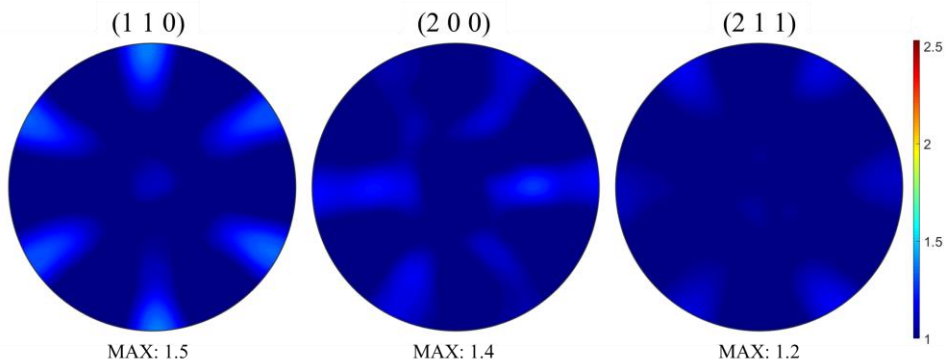
Elements (wt%)								
C	Si	Mn	P	S	N	Ti	Nb	Fe
0.002	0.01	0.1	0.01	0.005	0.002	0.03	0.003	Bal.

The initial microstructure of the ultra-low carbon steel was characterized using electron backscatter diffraction (EBSD). The EBSD data were represented and analyzed using TSL OIM AnalysisTM and MTEX software [102]. Fig. 3-1(a) and (b) display the inverse pole figure (IPF) map in the ND with a step size of 3.0 μm , and the (110), (200), and (211) pole figures,

respectively. The average grain size of the material is approximately 15 μm , indicating that the microstructure is composed of equiaxed ferritic phases with no particular preferred orientation, which is consistent with the expected result of the hot-rolling process.



(a)



(b)

Fig. 3-1. Microstructure of the investigated ultra-low carbon steel. (a) Normal direction inverse pole figure map, and (b) (110), (200), and (211) pole figures.

3.2.2. Basic mechanical properties

Uniaxial tension tests were conducted following the ASTM E8 standard to measure basic mechanical properties such as elastic properties, yield stress, ultimate tensile stress, and uniform elongation. These tests were performed under quasi-static conditions with a strain rate of 0.001 s^{-1} . The stress-strain data indicated an upper yield point of 243.6 MPa and a lower yield point of 238.6 MPa, followed by substantial work hardening. The ultimate tensile stress was measured to be 356 MPa, and the uniform elongation was 22.2%. The elasto-plastic properties of the ultra-low carbon steel sheet are summarized in Table 3-2.

Table 3-2. Basic mechanical properties of the investigated ultra-low carbon steel.

Young's modulus (GPa)	Poisson's ratio	Yield strength (MPa)		Tensile strength (MPa)	Uniform elongation (%)
		Upper	Lower		
205	0.3	243.6	238.6	356	22.2

3.2.3. Heat treatment for static recrystallization

The ultra-low carbon steel was subjected to cold rolling with an 85.5% reduction ratio, followed by heat treatments ranging from 650 °C to 790 °C for durations ranging from 0 s to 400 s to reproduce static recrystallization. Seven ASTM E8 specimens (denoted as S1 to S7) were obtained after different heat treatments followed by rapid quenching, as shown in Fig. 3-2. The engineering stress-strain curves for the as-received, cold-rolled, and seven heat-treated samples (S1 to S7) are depicted in Fig. 3-3. Pole figures and ND IPF maps for the heat-treated specimens were obtained as outlined in Section 3.2.1. The process employed a step size of 1.5 μm , and the results are shown in Fig. 3-4.

The flow stress curves indicate that the strength decreases and ductility improves with annealing. A further improvement in ductility is observed at the annealing temperature of 790 °C (S3), without a corresponding decrease in strength. This is corroborated by the microstructural changes, which do not show significant differences beyond this temperature, as shown in Fig. 3-4.

For the validation of the proposed models, the recrystallization (or annealing) condition is set as that of the S3 specimen. Fig. 3-5 displays the grain size distributions for the as-received, cold-rolled, and annealed (recrystallized) specimens. The average grain sizes of the three specimens are

14.96 μm , 3.34 μm , and 11.02 μm , respectively. These average values were measured using EBSD software, following the commonly used standard measurement procedure, which involves monitoring grain boundaries where the orientation changes abruptly.

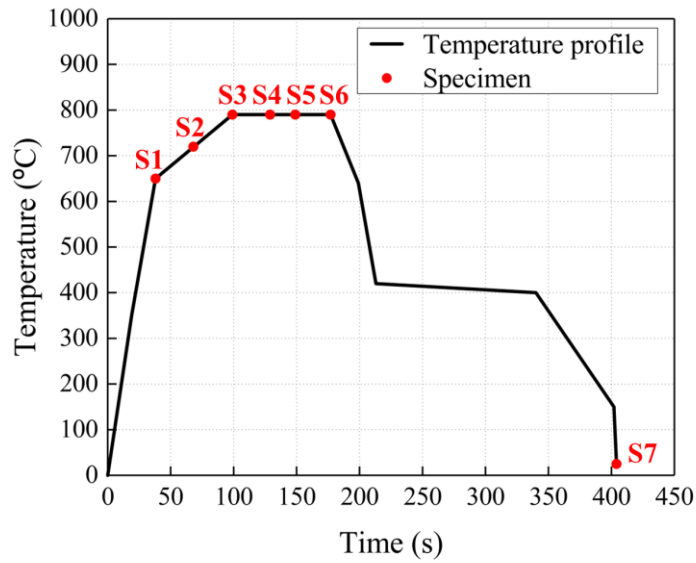


Fig. 3-2. Heat treatment conditions for reproducing static recrystallization.

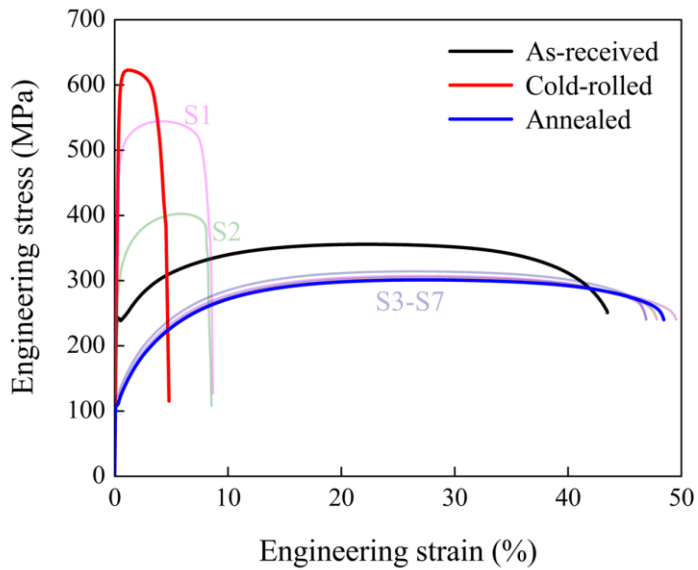


Fig. 3-3. Engineering stress-strain curves of the ultra-low carbon steel in different heat treatment conditions.

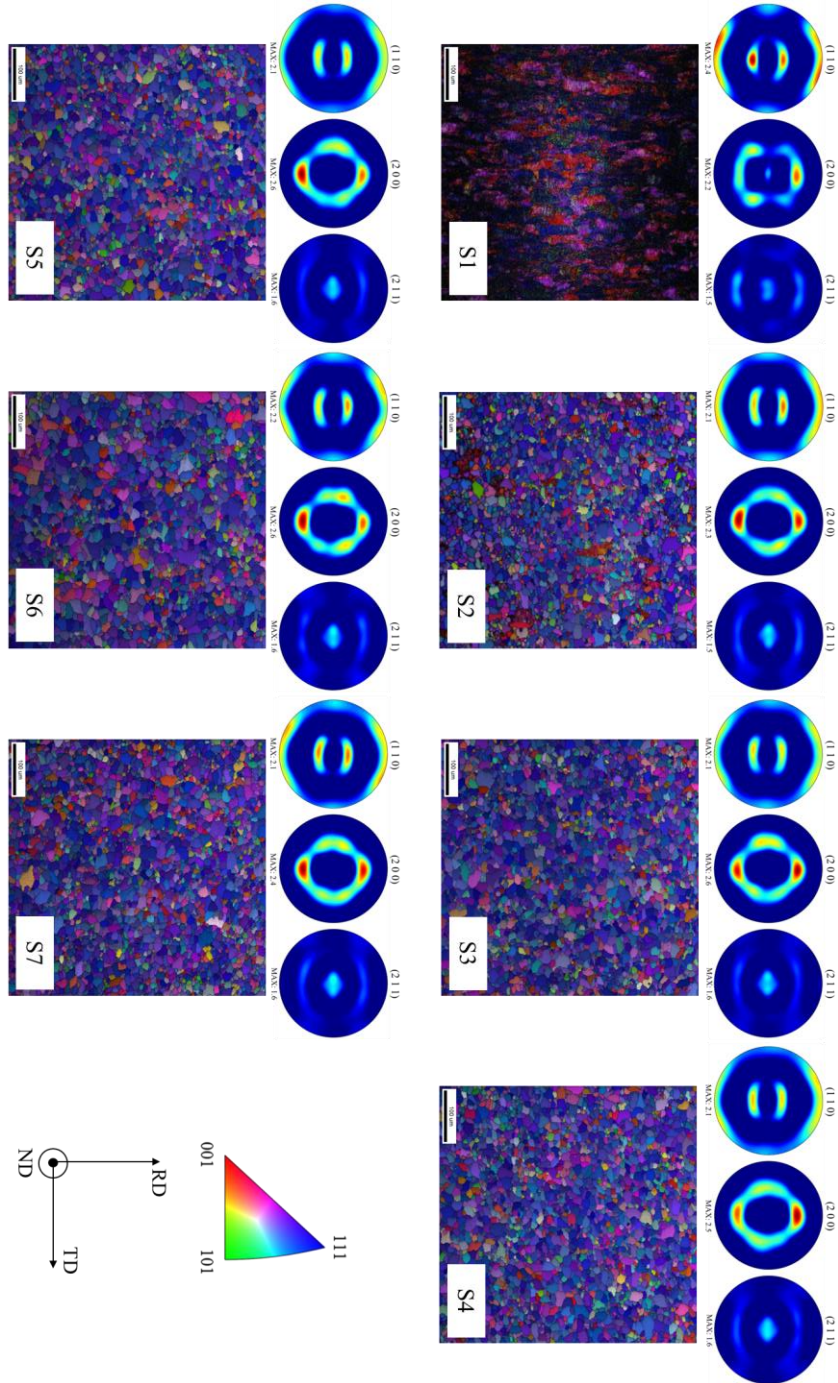
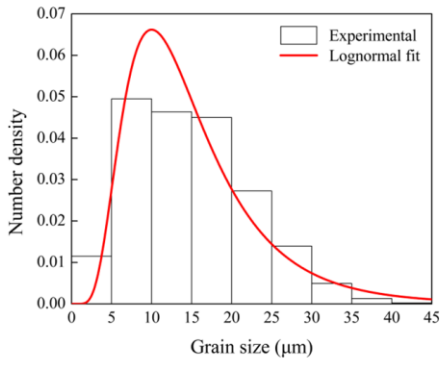
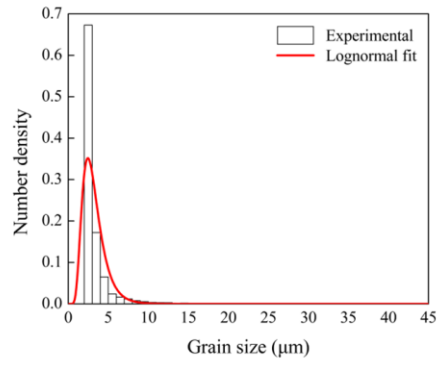


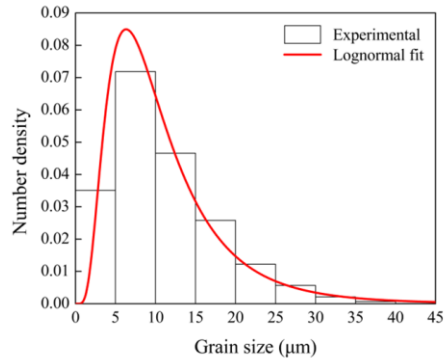
Fig. 3-4. Microstructure evolutions during heat treatment. (110), (200), and (211) pole figures (above) and normal direction inverse pole figure maps (below).



(a)



(b)



(c)

Fig. 3-5. Grain size distributions of (a) as-received, (b) cold-rolled, and (c) annealed (fully recrystallized) specimens.

3.3. Results and discussion

3.3.1. Constitutive parameter identification

For the cold rolling simulation, the constitutive parameters of ultra-low carbon steel, as described in Section 2.2, were determined. The parameters associated with intrinsic material properties, such as the anisotropic elastic constants (C_{11} , C_{12} , and C_{44}), shear modulus (G^0), magnitude of the Burgers vector (b), and Poisson's ratio (ν) for the cubic crystals for steel, could be obtained from both experimental data and the literature [75,103]. Q_0 and v_0 , parameters of the plastic shear strain rate, were obtained from Ma and Roters [24] and Jia et al. [65], respectively, considering both edge and screw dislocations. H^α and d_g , which are the parameters associated with grain boundary hardening, were determined based on Takaki [104] and experimental data, respectively. The effect of solid solution on hardening behavior of ultra-low carbon steel was not taken into consideration in this chapter. Additionally, the effects of shear band on thermo-mechanical processed ultra-low carbon steel, which is beyond the scope of this chapter, were also not addressed.¹ $\rho_{0,edge}$ and $\rho_{0,screw}$ were calculated using the

¹ This chapter is primarily dedicated to the prediction of anisotropy and formability for thermo-mechanically processed ultra-low carbon steel using the integrated CP-PF model. The role of shear band during static recrystallization, while significant, is not the subject of this chapter and will be covered in Chapter 4.

measured yield strength based on Takaki et al. [92], considering the initial edge and screw dislocation fractions. The other sets of parameters could be determined by fitting the tensile stress-strain curve and load data during cold rolling of the specimen. Because the uniform elongation of the investigated material was limited to ~22 %, the larger part of the flow stress curve was extrapolated using the dislocation density-based constitutive law employed in the current CPFEM. While the validity of considering flow stress at a larger strain for the cold rolling simulation remains controversial, this approach is still commonly used. The identified constitutive parameters are listed in Table 3-3.

Table 3-3. Constitutive model parameters of the investigated ultra-low carbon steel.

C_{11}	C_{12}	C_{44}	G	b
230.1 GPa	134.6 GPa	116.6 GPa	69.2 GPa	0.248 nm
ν	Q_0	ν_0	H^α	d_g
0.3	2.0×10^{-19} J	1.0×10^{10} s ⁻¹	0.55	14.96 μ m
$\rho_{0,edge}$	$\rho_{0,screw}$	c_1^*	c_2^*	c_3^*
9.18×10^{11} m ⁻²	1.21×10^{12} m ⁻²	0.006	0.55	1.29
c_4^*	c_5^*	R_{edge}^*	R_{screw}^*	
1.51	3.38	47.12 nm	63.05 nm	

* Fitting parameters used in the dislocation density-based hardening model

Fig. 3-6 shows the comparison of the fitted stress-strain curve with the curve obtained using the measured stress and strain values. As seen from the figure, the identified constitutive parameters align well with the experimental data.

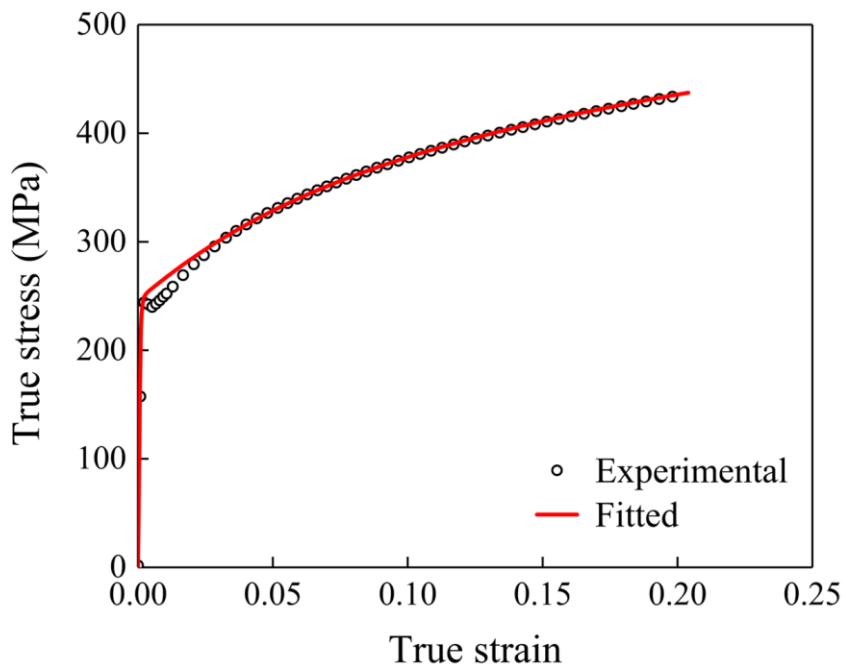


Fig. 3-6. Comparison of CP calculated stress-strain curve with measured one for ultra-low carbon steel.

3.3.2. Simulation of cold-rolled ultra-low carbon steel

The RVE model, consisting of 498 grains, was generated based on the statistically analyzed microstructural information of hot-rolled ultra-low carbon steel, as detailed in Section 3.2.1. This RVE model was subsequently employed for simulating the cold rolling process. More details regarding the generation of the RVE can be found in Section 2.2.5. The side length of the RVE model was set to 90 μm , and it comprised 27,000 ($30 \times 30 \times 30$) elements. Fig. 3-7 presents the RVE model for the hot-rolled ultra-low carbon steel.

For the simulation, a plane strain compression condition was imposed as a simplified loading equivalent to the typical cold rolling process. The displacement in the transverse direction (TD) was fixed and compressive loading was applied along the ND. The thickness reduction ratio was set to 85.5%, identical to the experimental conditions. Additionally, PBCs, as discussed in Section 2.2.5, were also applied to the RVE to ensure its physically continuous behavior.

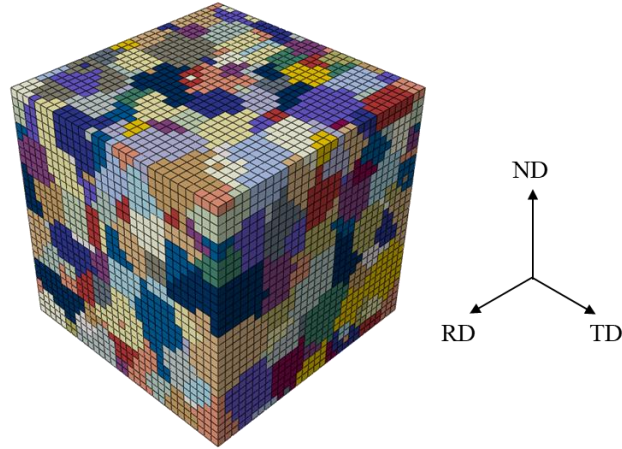


Fig. 3-7. Representative volume element model for hot-rolled ultra-low carbon steel

Fig. 3-8 displays the deformed RVE and its equivalent plastic strain with a thickness reduction ratio of 85.5%. Due to the severe plastic deformation from plane strain compression with a thickness reduction ratio of 85.5%, the equivalent plastic strain reached ~ 2.3 . Fig. 3-9(a) presents the distributions of the total dislocation densities after the CPFEM simulations, as well as the dislocation densities mapped for the PFM simulations. Approximately 3000 grids per grain were used in this mapping process. In the CPFEM, the dislocation densities and other state variables are calculated at the integration points, which are then properly mapped onto the PFM grids. In this chapter, a regularized Wigner-Seitz cell approach was employed, as detailed in the Section 2.4. Fig. 3-9(b) shows the comparison of the total dislocation

densities along an arbitrary RD line before (with CPFEM) and after mapping to PFM grids. As shown, the quality of proposed mapping approach was reasonably validated, although the overall mapping procedure was automatically programmed without manual direct mapping.

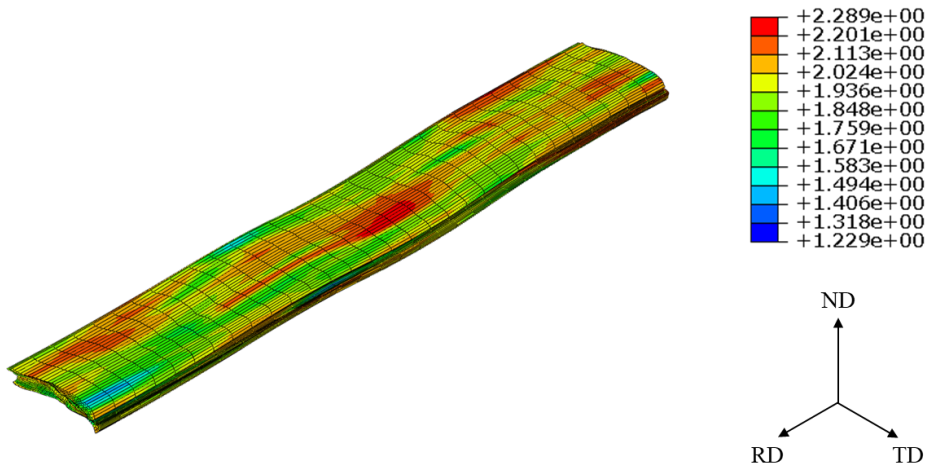
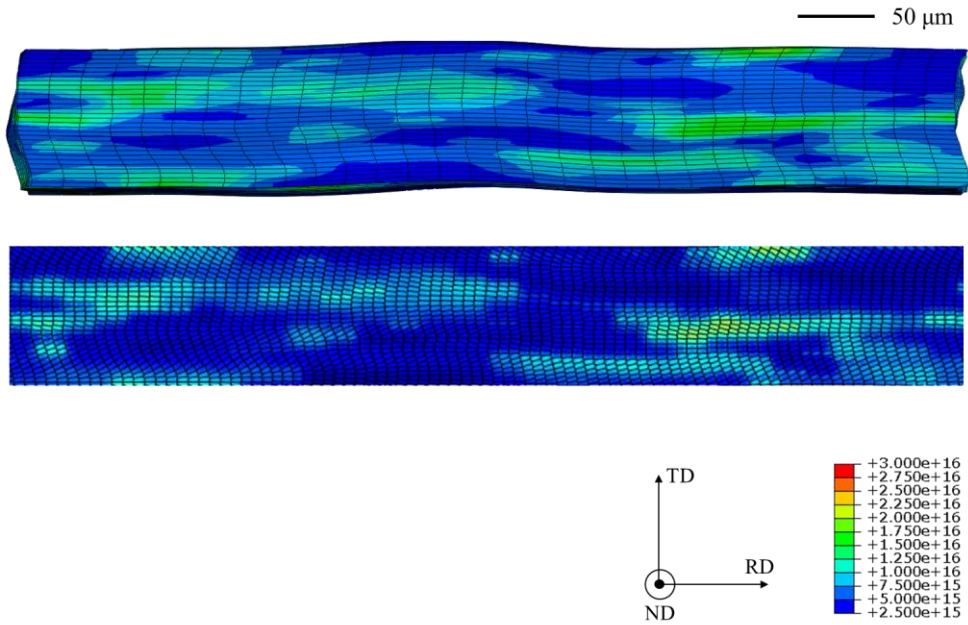
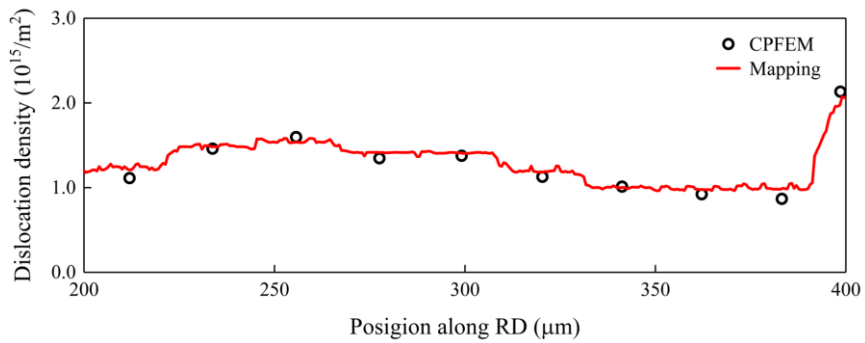


Fig. 3-8. Deformed representative volume element and its equivalent plastic strain after a thickness reduction ratio of 85.5%.



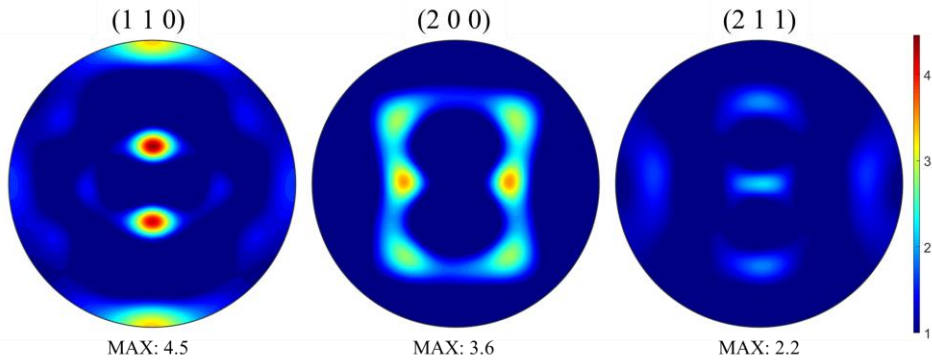
(a)



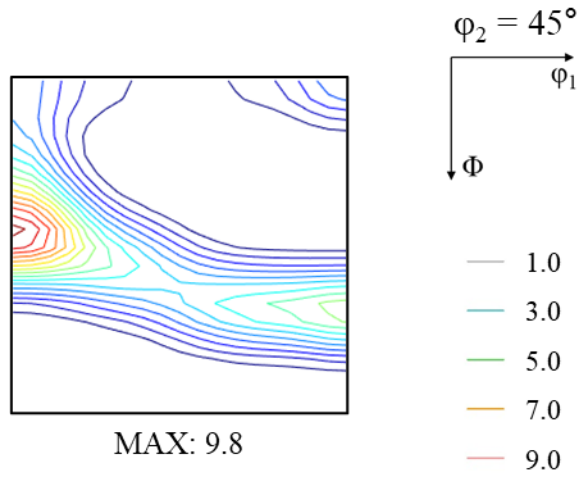
(b)

Fig. 3-9. (a) Deformed representation volume element and its total dislocation densities (unit: m^{-2}) after a thickness reduction ratio of 85.5% rolling and (b) comparison of total dislocation densities before (with CPFEM) and after mapping to PFM grids.

The calculated rolling texture of ultra-low carbon steel are presented in Fig. 3-10. Fig. 3-10(a) and (b) depict the three (110), (200), and (211) pole figures and the $\varphi_2=45^\circ$ orientation distribution function (ODF) section after 85.5% cold rolling (equivalently, the plane strain compression), respectively. The calculated cold-rolling texture of ultra-low carbon steel showed mixture of the major α -fiber ($\langle 110 \rangle // \text{RD}$) and minor γ -fiber ($\langle 111 \rangle // \text{ND}$), which is in agreement with experimentally measured texture components [52,91]. In particular, three main experimentally reported cold-rolling texture components, $\{665\}\langle 110 \rangle$ (approximated by $\{111\}\langle 110 \rangle$), $\{558\}\langle 110 \rangle$ (approximated by $\{112\}\langle 110 \rangle$), and $\{001\}\langle 110 \rangle$, can be perfectly predicted from the proposed CPFEM.



(a)



(b)

Fig. 3-10. Predicted rolling texture of ultra-low carbon steel after a thickness reduction ratio of 85.5%. (a) (110), (200), and (211) pole figures and (b) $\phi_2=45^\circ$ orientation distribution function section.

3.3.3. Simulation of recrystallized ultra-low carbon steel

The process of static recrystallization, or annealing, was simulated using the proposed PFM. This was performed by utilizing the state variables derived from the CPFEM results of the cold rolling (plane strain compression) simulation. The parameters used for the PFM simulation are as follows:

- Phase field grid size (Δx): 0.6 μm
- Grain boundary thickness (ξ^0): $3\Delta x$
- Grain boundary mobility (c^m): $316 \times 10^6 \text{ m}^4 \text{ s}^{-1} \text{ J}^{-1}$ [105]
- Activation energy for grain boundary mobility (Q_0^m): 387 kJ mol^{-1} [105]
- Grain boundary energy (γ^0): 1.11 J m^{-2} [106]
- Material constant for recovery (c_1^r): $1.65 \times 10^{22} \text{ N m}^{-2}$
- Material constant for recovery (c_2^r): $3.118 \times 10^{-4} \text{ m}^3 \text{ mol}^{-1}$ [107]
- Activation energy for recovery (Q^r): 345 kJ mol^{-1} [107]
- Temperature (T): 1023.15 K
- Gas constant (R) = 8.3145 $\text{J mol}^{-1} \text{ K}^{-1}$

The time increment used in the simulation was 0.002 s. The periodic

boundary conditions were applied throughout the simulation.

Fig. 3-11 depicts the progression of static recrystallization over time during the annealing process, as predicted by the PFM. The color code within the grains corresponds to the ND IPF map. The orientations of the newly nucleated grains were determined from the results predicted using the GSERM model, which calculates the orientation probability upon nucleation.² In order to avoid the formation of idealistically oriented grains by theoretical calculations, random orientations were also assigned to nucleation orientation probability. The ratio of calculated orientations to random orientations was maintained at 7:3.

The recrystallized grains can be clearly distinguished from the remaining deformed grains due to their equiaxed morphology. The residual deformed grains were elongated along the RD in the form of fibers, which is a characteristic feature of metals subjected to cold rolling.

It is noted that there are significant inter- and intra-heterogeneities induced from different slip activities under different grain orientations during the rolling process. In Fig. 3-11, a high angle grain boundary of 15° was used, making the color coding present a single-grain-like appearance. However,

² The GSERM model does not consider nucleation and grain growth during the process of static recrystallization. Therefore, the results derived from the GSERM model was expressed as nucleation orientation probability.

there were actually orientation differences (within a low angle) among different grids in a grain. Moreover, in Fig. 3-11, the original parent grain boundaries (elongated to the RD) were fixed. This was primarily due to the large difference in stored energy between the recrystallized grain boundaries and their corresponding parent grains. This assumption was also beneficial in terms of reducing the computational cost.

As depicted in the figure, nucleation was initiated in regions with a higher level of stored energy (refer to Fig. 3-9(a) for the distribution of dislocation density after rolling simulation). The calculated results from the annealing simulation effectively reproduced the experimentally observed characteristics of static recrystallization. Consequently, nucleation took place in areas of the high dislocation density, and it was delayed in the areas where there was less stored energy. As recrystallization progresses, the matrix was gradually consumed by growing nuclei originating from highly recrystallized regions. Furthermore, no additional nucleation occurred within the previously recrystallized grains; rather, they undergo coarsening due to small misorientation differences with adjacent grains.

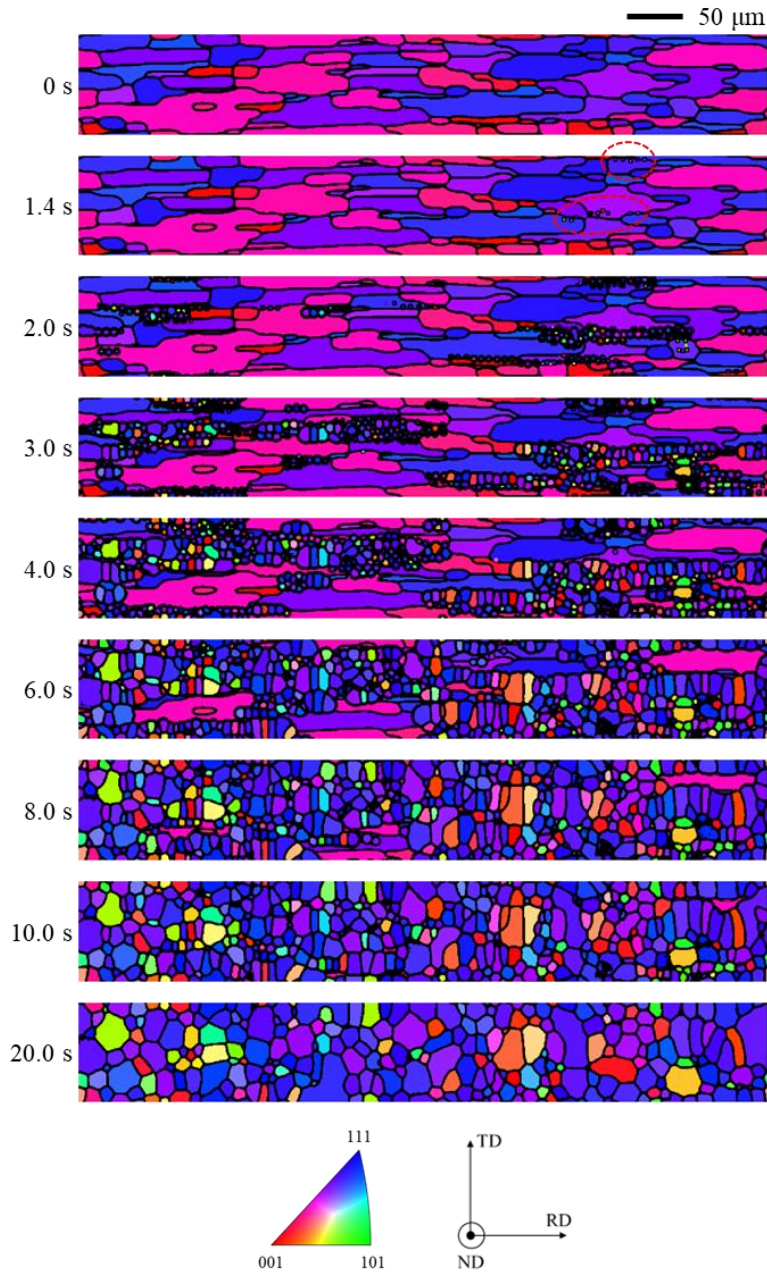


Fig. 3-11. Microstructure evolution during static recrystallization of ultra-low carbon steel using integrated CP-PF model. The colors indicate the normal direction inverse pole figure map. At the 1.4 s mark, red dotted circles highlight the sites of the first nucleation.

Fig. 3-12 presents schematic representation of the nucleation criterion in relation to the evolution of stored energy caused by the recovery process used in PFM simulation. According to this criterion, nucleation is determined at the intersection point of the critical nucleation radius $r_c(t)$ (the area marked in gray) and the growing nucleus radius $r(t)$ (the area marked with hatching), both of which are driven by stored energy. In this figure, the time taken to reach the red intersection point signifies the incubation time for nucleation. In Fig. 3-11, the first nucleation was observed at 1.4 s, which aligns the calculated incubation time shown in Fig. 3-12.

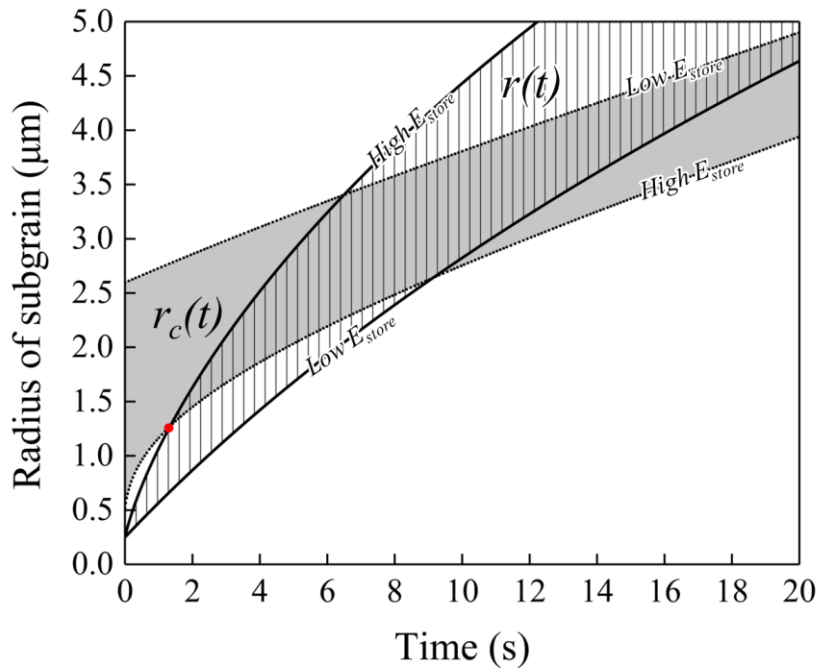


Fig. 3-12. Schematic illustration of nucleation criterion used in the PFM simulation. The red intersection point represents the incubation time for nucleation.

The recrystallization texture derived from the PFM simulation is depicted in Fig. 3-13. The (110), (200), and (211) pole figures and the $\phi_2=45^\circ$ section of the ODF after annealing are shown in Fig. 3-13(a) and (b), respectively. As mentioned above, the orientations of newly nucleated grains were determined based on calculations from the GSERM model before they underwent grain growth. The calculated recrystallization texture displays the γ -fiber centered on the $\{111\}\langle 112\rangle$ component, aligning with the texture reported in experimental studies for ultra-low carbon steel. During the annealing process, the minor rolling component $\{111\}\langle 112\rangle$ was fairly stationary, whereas other texture components moved towards $\{111\}\langle 112\rangle$ following a rotational relationship of $\pm 54.7^\circ\langle 110\rangle$. In particular, the proposed model was capable of predicting the transition from the γ -fiber $\{111\}\langle 110\rangle$ to the $\{111\}\langle 112\rangle$ component. Figs. 3-14(a) and (b) display the measured (110), (200), and (211) pole figures and the $\phi_2 = 45^\circ$ section of the ODF, respectively, after the annealing of the investigated ultra-low carbon steel. These closely align with the predicted recrystallization texture in Fig. 3-13.

The analyses suggest that the proposed PFM simulation, when coupled with the GSERM model, is a reliable approach for predicting the recrystallization texture of ultra-low carbon steels. Similar analyses were conducted by Park et al. [91] and Hong and Lee [52], employing a single component α - and γ -fiber and a fully constrained Taylor model. These studies

also reported similar evolutions of texture from α -fiber to γ -fiber, or from γ -fiber to γ -fiber. Nonetheless, these studies were conducted under the application of unique, individualized assumptions, hence their findings may not be universally applicable. Despite this, the present study offers additional verification that the GSERM model - which accommodates multiple slip activities across a potential 24 slip systems and takes into account inter-grain interactions - can indeed successfully reproduce the recrystallization texture observed in annealed ultra-low carbon steel.

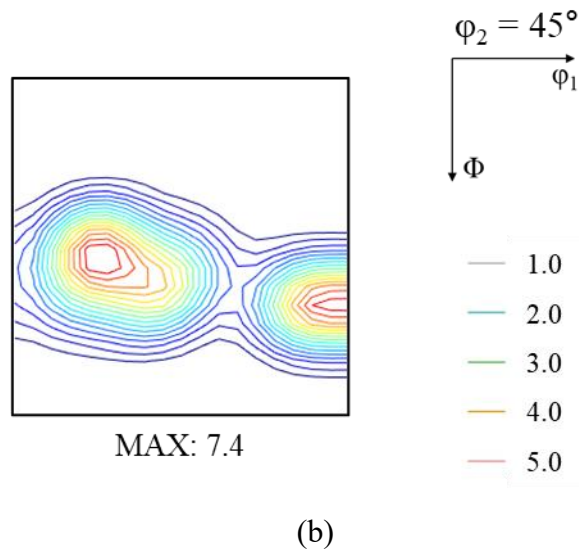
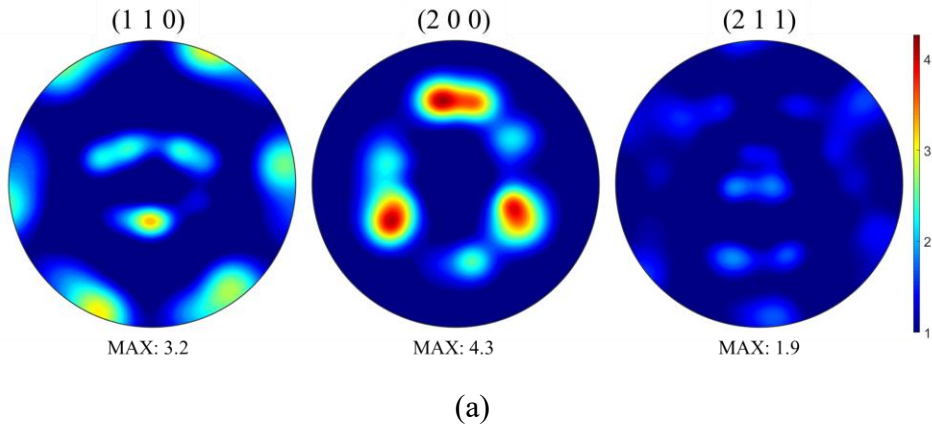


Fig. 3-13. Predicted recrystallization texture of ultra-low carbon steel. (a) (110), (200), and (211) pole figures and (b) $\phi_2=45^\circ$ orientation distribution function section.

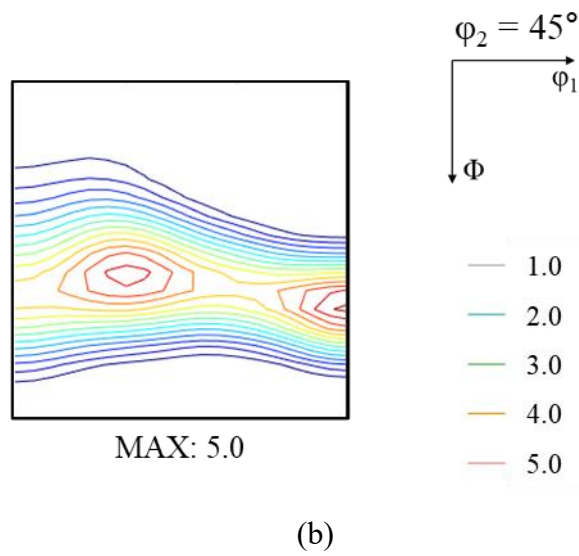
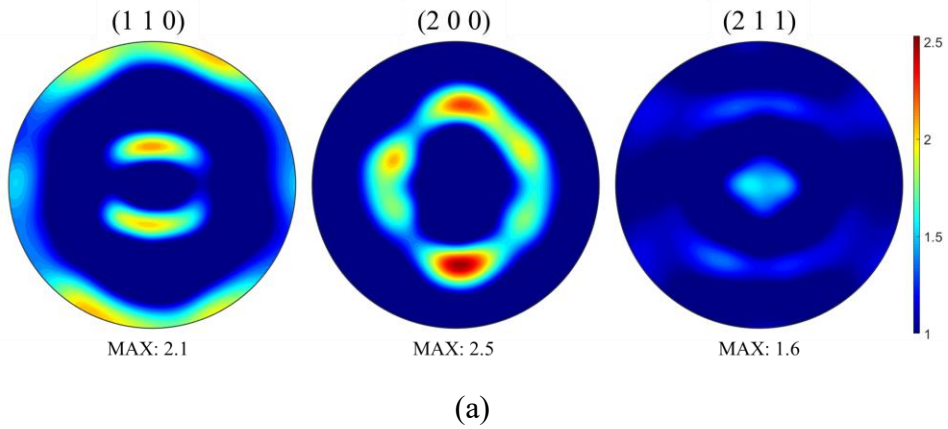


Fig. 3-14. Measured recrystallization texture of ultra-low carbon steel. (a) (110), (200), and (211) pole figures and (b) $\phi_2=45^\circ$ orientation distribution function section.

Apart from the recrystallization texture, the kinetics and grain size distribution after annealing simulation of ultra-low carbon steel were predicted using the proposed PFM. As shown in Fig. 3-15, the predicted recrystallized fraction over time matches well with the well-established Avrami type kinetics (also known as the Johnson-Mehl-Avrami-Kolmogorov, or JMAK equation), yielding an exponent of 2.51 for current study. Given that experimental studies on comparable grades of steel have reported exponents ranging from 1.3 to 2.6 [105], the result obtained from the current simulation was reasonably consistent with experimental findings.

Fig. 3-16 presents a comparison between the simulated and experimentally measured grain size distribution after annealing. Both distributions were fitted to a log-normal model. The predicted distribution aligns closely with the experimental data, exhibiting an average predicted grain size of 11.9 μm , which matches the experimental value of 11.1 μm . The parameters for the log-normal distribution, μ and σ , were found to be 2.35 and 0.51, respectively, while the corresponding experimental values were determined to be 2.22 and 0.61, respectively. This discrepancy could be attributed to the limited number of grains included in the model and the fact that the PFM employed in this chapter was two-dimensional, a choice made to optimize computational costs and efficiency of the analysis. Comparable two-dimensional methodologies have been utilized for multi-phase field

modeling for similar reasons [34,72,74,108,109]. The impact of model dimensionality on PFM could be explored in future studies.

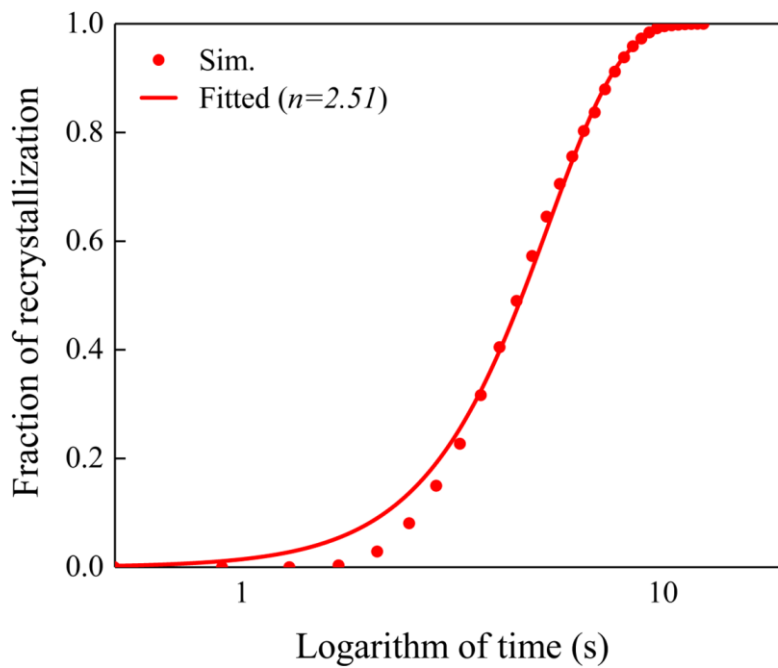


Fig. 3-15. Fraction of recrystallization with Johnson-Mehl-Avrami-Kolmogorov (JMAK) equation.

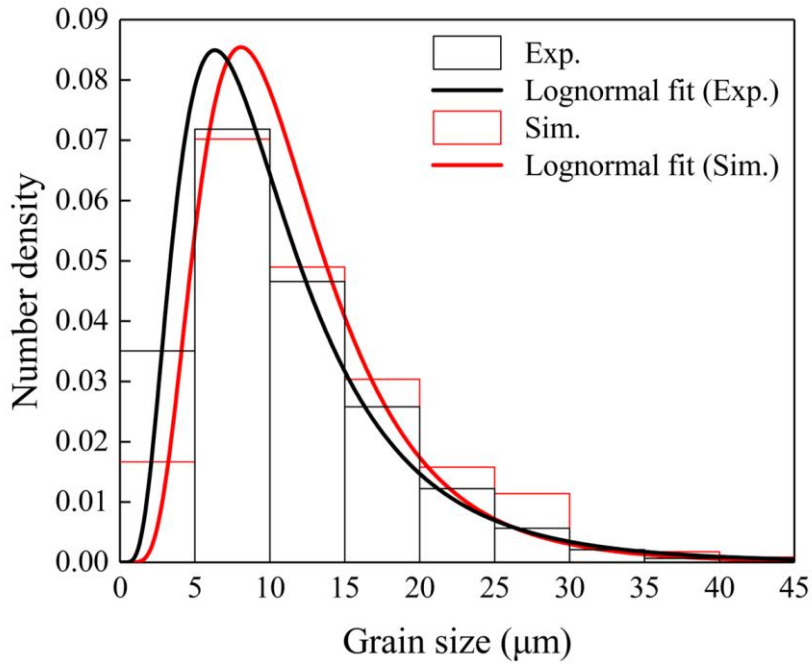


Fig. 3-16. Predicted and measured grain size distributions after annealing.

Despite these limitations, the quantitative results endorse the accuracy of the proposed modeling approach. Fig. 3-17 provides a comparison between the predicted microstructure using the calculated grain size distribution and recrystallization texture (left), and the experimental microstructure (right), which demonstrates the predictive ability of the current modeling approach.

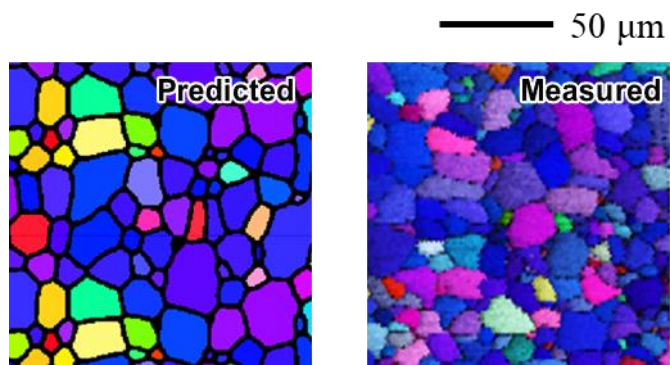


Fig. 3-17. Microstructure generation by the proposed modeling approach. The colors indicate the normal direction inverse pole figure map.

3.3.4. Prediction of anisotropy and formability of ultra-low carbon steel

In this section, the procedure for executing virtual mechanical tests was described, utilizing the microstructural information of annealed (or fully recrystallized) ultra-low carbon steel obtained from the proposed integrated CP-PF model. This information included recrystallization texture (Fig. 3-13), grain size, and its distribution (Fig. 3-16). Subsequently, the RVE for these virtual experiments was generated using the same procedure for the cold rolling simulation outlined in Section 3.3.2, based on the predicted microstructural information of annealed ultra-low carbon steel. The investigated RVE model consisted of 941 orientations and 27000 elements.³ For the FE simulations, the eight-node continuum elements with reduced integration were used.

Based on the RVE models, constructed with the predicted microstructural information, uniaxial tensile tests along material orientations differing from the RD and balanced biaxial tensile test were virtually performed. For the CPFEM parameters of the recrystallized grains, the initial dislocation densities of the recrystallized grain were reduced to 18.2% of their value, a reduction derived by fitting the yield stress of annealed ultra-low

³ In PFM, there were slight orientation differences among different grids within a grain. When applying a high angle grain boundary of 15°, 941 orientations can be interpreted as 224 distinct grains, as shown in Fig. 3-11. However, in order to generate a RVE for the accurate prediction of plastic anisotropy, all 941 orientations were taken into consideration.

carbon steel in the RD. And the average grain size (d_g) was derived from the predicted value. However, all other hardening-related parameters remained identical to those of undeformed parent grains (Table 3-3). Subsequently, the Lankford coefficients (or r-values) and yield stresses in different material directions were predicted as measures for the plastic anisotropy. The boundary conditions for the uniaxial tension and balanced biaxial tension were as follows: PBCs were applied to all simulations, and the prescribed displacement was controlled to maintain a constant strain rate of 10^{-3} s^{-1} , suitable for the quasi-static test conditions. Fig. 3-18 shows the RVE model used in the simulations and deformed meshes after uniaxial tension as an example.

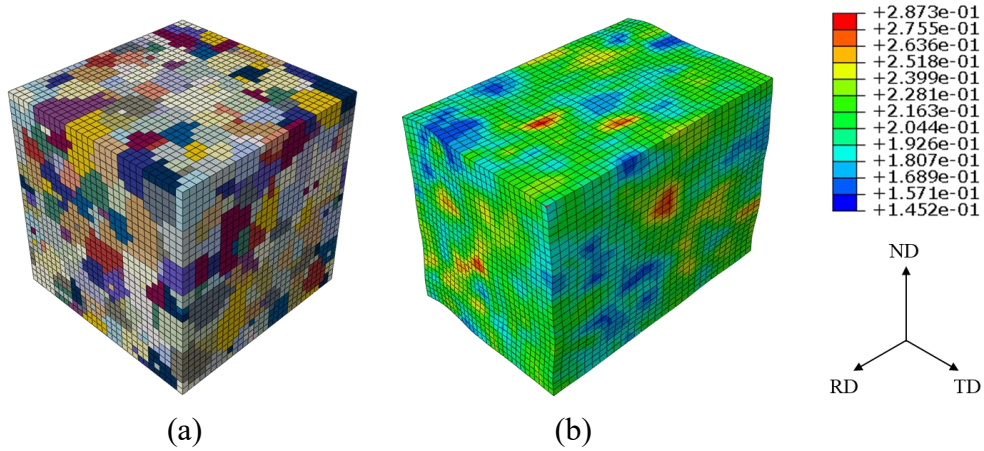


Fig. 3-18. (a) Representative volume element (RVE) model for virtual mechanical tests based on predicted microstructural information of annealed ultra-low carbon steel and (b) example of deformed RVE and its equivalent plastic strain after the virtual uniaxial tensile test.

Fig. 3-19 depicts the predicted plastic anisotropy obtained from the proposed virtual mechanical tests, which includes the r-values and yield stresses (normalized by the yield stress at RD) along different angles from the RD. These predicted results were compared with experimental data for validation. The r-values were measured at an engineering strain of 20%, taking into account a uniform elongation of approximately 25%. The results showed that the r-value at 45° from the RD was lower than those along the RD and TD, which is in line with experimental observations. Moreover, the yield stresses along different loading directions matched well with

experimental values. Table 3-4 summarizes all anisotropic mechanical properties obtained from the virtual experiments, encompassing uniaxial tension and balanced biaxial tension. These results validated that the proposed virtual experimental strategy, employing the integrated CP-PF model, can be an effective alternative for experimental procedures in evaluating anisotropic constitutive equations for future applications.

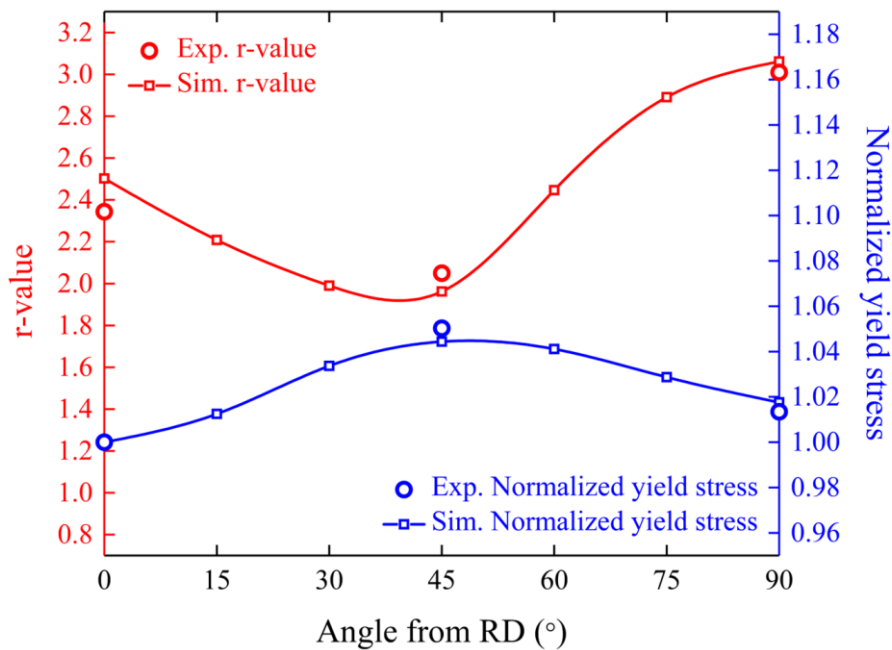


Fig. 3-19. Comparison of the measured and predicted plastic anisotropy in annealed ultra-low carbon steel, featuring the Lankford coefficients and normalized yield stresses along various material orientations.

Table 3-4. Measured and predicted plastic anisotropy in annealed ultra-low carbon steel, featuring the Lankford coefficients and normalized yield stresses along various material orientations.

		0°	15°	30°	45°	60°	75°	90°	BB*
Lankford coefficient	Exp.	2.343	-	-	2.049	-	-	3.009	0.972
	Sim.	2.502	2.209	1.99	1.962	2.447	2.891	3.062	0.947
Normalized yield stress	Exp.	1	-	-	1.05	-	-	1.013	1.059
	Sim.	1	1.012	1.034	1.044	1.041	1.029	1.018	1.087

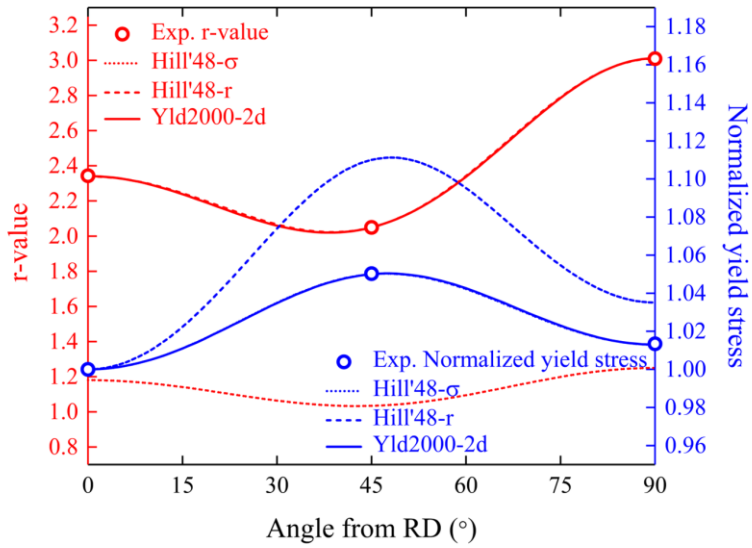
* Balanced biaxial tension

A more detailed investigation of plastic anisotropy was carried out, as presented in Fig. 3-20, using various anisotropic yield functions. For modeling plastic anisotropy of annealed ultra-low carbon steel, the Hill 1948 yield function (Hill'48) [110] and the Yld2000-2d non-quadratic yield function [111] were considered. For validation purposes, both measured and predicted plastic anisotropies, including r-values and yield stresses, were utilized to identify the anisotropic yield functions. Fig. 3-20(a) displays the variations of r-value and normalized yield stress based on experimental values, while Fig. 3-20(b) presents the corresponding variations based on predicted values obtained from virtual experiments. Among the identified yield

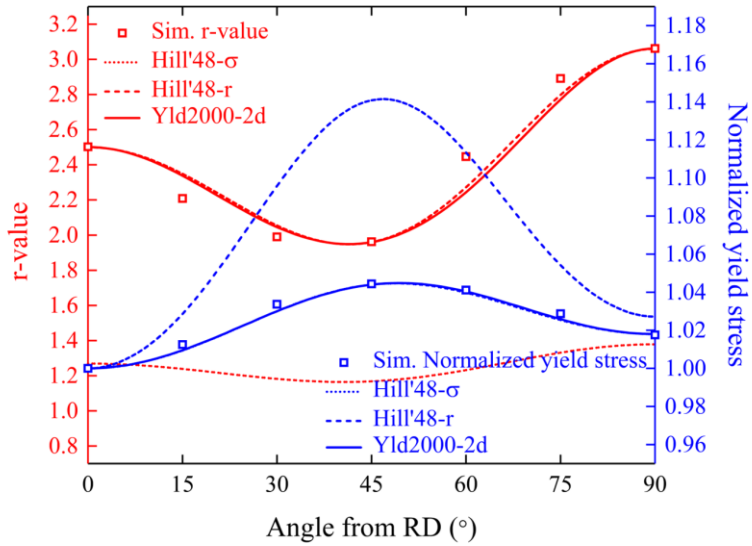
functions, the Yld2000-2d showed the best match with both measured and predicted plastic anisotropy. The yield loci identified using the Hill'48 and Yld2000-2d yield functions are depicted in Fig. 3-21, and their parameters are summarized in Table 3-5.

Table 3-5. Material parameters of annealed ultra-low carbon steel used for anisotropic yield functions

		F	G	H	N					
Hill'48 -σ	Exp.	0.433	0.459	0.541	1.368					
	Sim.	0.406	0.441	0.559	1.412					
		F	G	H	N					
Hill'48 -r	Exp.	0.233	0.299	0.701	1.357					
	Sim.	0.233	0.286	0.714	1.277					
		α₁	α₂	α₃	α₄	α₅	α₆	α₇	α₈	a
Yld 2000 -2d	Exp.	1.054	1.067	1.05	0.909	0.924	0.946	1.006	0.81	6
	Sim.	1.074	1.044	0.978	0.896	0.911	0.928	1.006	0.866	6



(a)



(b)

Fig. 3-20. Variations of r-value and normalized yield stress for annealed ultra-low carbon steel along various material orientations, obtained using various anisotropic yield functions based on (a) experimental and (b) predicted values.

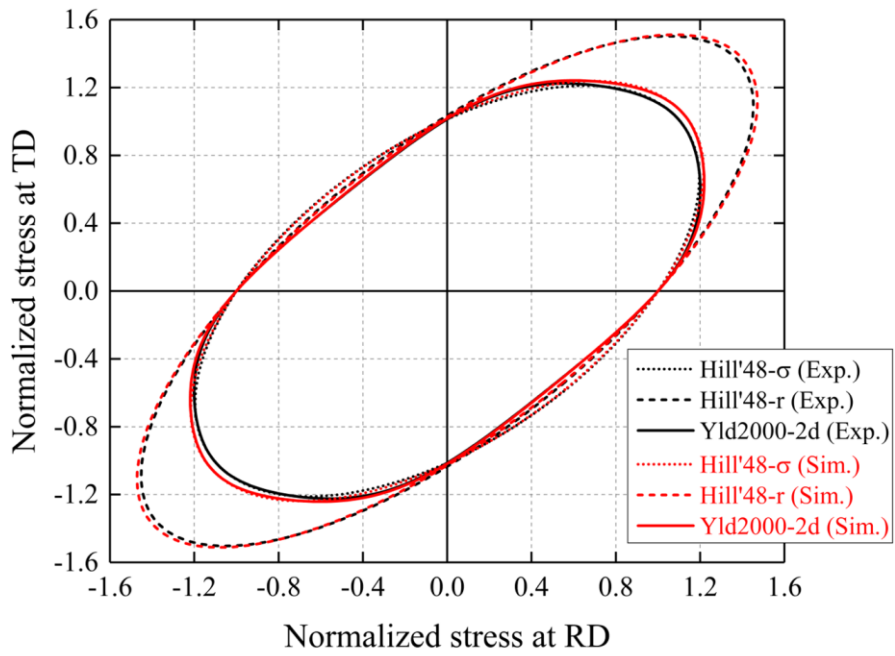


Fig. 3-21. Identified yield loci for annealed ultra-low carbon steel, obtained using the various anisotropic yield functions.

Sheet formability of annealed ultra-low carbon steel, represented by FLD, was evaluated. Based on the M-K model [58], FLDs were calculated using various anisotropic yield functions, as identified in Table 3-5 and Fig. 3-21. In addition to this yield function-based approach, a hybrid FLD prediction scheme [59], which combines the CPFEM and M-K model to account for the microstructure evolution at grain-scale and macro-scale, respectively, was utilized. Unlike the yield function-based approach, which uses fixed r-values as parameters, this approach was designed to consider the evolution of crystallographic texture during deformation, which means the evolution of r-values during deformation. Since drawability, one of the perspectives for evaluating sheet formability, is primarily characterized by sheet anisotropy, accurate predictions of anisotropic mechanical properties can be beneficial for the predictions of FLD.

Fig. 3-22 displays the FLDs for annealed ultra-low carbon steel obtained using both yield function-based and CP-based (referred to as CPFLD in Fig. 3-22) approaches. These predicted results were compared with experimental data, which was obtained from the well-known Nakajima-type ISO standard test [112]. The initial imperfection factor (f_0) was determined to be 0.995 for both approaches through an iterative fitting process of the forming limit strains under the plane strain tension condition ($\rho = 0$) or FLD₀. In the yield function-based approach, a Swift-type strain hardening law given by Eq. (3.1)

was employed:

$$\bar{\sigma} = K \left(\varepsilon_0 + \bar{\varepsilon}^p \right)^n \quad (3.1)$$

where $(K, \varepsilon_0, n) = (597.7, 0.002, 0.259)$. The hardening parameters in Eq. (3.1) were determined by iteratively fitting the uniaxial tensile stress-plastic strain curve in the RD.

As shown in Fig. 3-22, minor discrepancies were observed between the instances of using experimental and predicted values in the yield function-based approach. Instead, the calculated FLD results revealed the dependency on the yield functions. This affirms the accuracy of the predicted plastic anisotropy obtained through the virtual experiment scheme. The minimum forming limit strains were observed under a plane strain tension condition ($\rho=0$) in experimental FLD and yield function-based FLDs, whereas the CPFLD predicted the minimum forming limit strains at approximately $\rho=0.16$. On the left side of the FLD ($\rho < 0$), which is influenced by plastic anisotropy and thus related to drawability, FLDs calculated using Hill'48 showed a slightly steeper negative slope compared to the experimental FLD. In contrast, the CPFLD and FLDs calculated using Yld2000-2d aligned well with the experimental FLD. On the right side of the FLD ($\rho > 0$), corresponding to the biaxial stretching regime, there was a notable difference between the approaches. In the yield function-based approach, Hill'48- σ

showed an upper limit, while Hill'48-r displayed a lower limit, and Yld-2000-2d fell in between. Moreover, in the CPFLD and FLDs calculated using Yld2000-2d, the positive slope tended to gradually decrease with an increase in ρ , which is consistent with experimental observations. As anticipated, given the consideration of texture evolution during deformation, the CPFLD provided a more accurate prediction than the Yld2000-2d case, yielding the closest values to the experimental ones.

The predicted sheet anisotropy and formability confirmed that the proposed integrated CP-PF model can effectively reproduce the microstructural characteristics of thermo-mechanically processed ultra-low carbon steel, while so taking into account the effect of microstructure evolution on mechanical properties. This reinforces the validity and accuracy of the proposed model as a robust tool for comprehending the intricate relationship between process, structure, property, and performance.

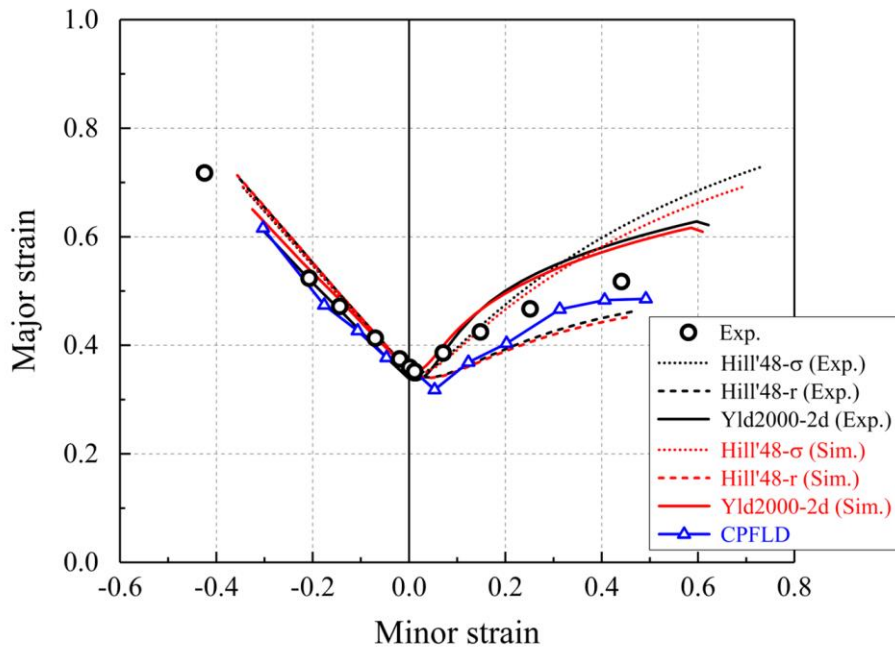


Fig. 3-22. Comparison of forming limit diagrams for annealed ultra-low carbon steel, obtained using various yield functions and crystal plasticity-based approach (CPFLD), with experimental values.

3.4. Summary

This chapter presented the numerical reproduction of static recrystallization in ultra-low carbon steel, using the proposed integrated CP-PF model. The CPFEM successfully simulated microstructural heterogeneities induced by cold rolling, while the PFM was employed to simulate microstructure evolution during the annealing process. Subsequently, the effects of microstructure evolution on mechanical properties, such as sheet anisotropy and formability, were assessed through virtual mechanical tests. The accuracy and validity of the proposed model were confirmed by comparing its predicted results with experimental observations. The key contributions of this chapter are as follows:

- (1) The microstructure resulting from thermo-mechanical processing, as predicted by the proposed model, was efficiently validated by comparing the deformation and recrystallization textures, recrystallization fraction, grain size, and its distributions with experimental observations.
- (2) The proposed mapping algorithm was successful in transferring all microstructural characteristics from the results of the integrated CP-PF model.
- (3) Virtual mechanical tests were conducted using the RVE approach to

evaluate anisotropic mechanical properties. Orientation-dependent tensile properties, characterized by Lankford coefficients and yield stresses along various material orientations, were predicted and compared with experimental data for validation purposes.

- (4) The anisotropic yield functions, including Hill'48 and Yld2000-2d, were identified using both measured and predicted plastic anisotropies.
- (5) Sheet formability, represented by FLD, was evaluated using yield function-based and CP-based M-K model approaches and compared with experimental data derived from Nakajima tests.

4. Application II: Effect of non-crystallographic shear band on formation of Goss texture in primary recrystallization of grain-oriented electrical steel

4.1. Introduction

Grain-oriented (GO) electrical steel is a soft magnetic material with a body-centered cubic (BCC) structure. It has been primarily used in the cores of electromagnetic devices, including transformers [113–115]. The magnetic properties of GO electrical steel are determined mainly by the sharpness of its Goss $\{110\}\langle 001\rangle$ texture, which provides the direction easiest for magnetization along the $\langle 100\rangle$ direction [116–118]. To obtain a strong Goss texture, GO electrical steel is commonly manufactured using a thermomechanical process, involving hot and cold rolling, followed by a two-stage annealing process with primary and secondary recrystallization [119,120].

To facilitate the abnormal growth of Goss grains during secondary recrystallization, their nucleation should precede during (static) primary recrystallization. Several studies have reported that shear bands induced by deformation instability during severe plastic deformation would be the preferred nucleation sites for Goss grains during the primary recrystallization of GO electrical steel. Haratani et al. [121] demonstrated that shear bands are formed during the cold rolling of (111)[11-2] single crystal of 3 wt% Si

electrical steel and that those shear bands become preferred nucleation sites for Goss grains. Ushioda and Hutchinson [122] revealed that Goss grains with an almost ideal orientation were nucleated along high-angle (35°) shear bands, while those whose orientations were different from the ideal orientation were nucleated along low-angle (17°) shear bands, during primary recrystallization using (111)[11-2] single crystal of 3 wt% Si electrical steel. Samajdar et al. [119] showed that two types of shear bands inclined at 20° and 37° with respect to the rolling direction (RD) are formed during the cold rolling of 3 wt% Si GO electrical steel and that Goss grains with a spread of 20° and 5° , respectively, are nucleated within those shear bands. Wang et al. [123] showed that the nucleation of small equiaxed Goss grains in 3 wt% Si GO electrical steel occurred within the shear bands in the deformed $\{111\}$ //normal direction (ND) grains. Fang et al. [124] investigated the microstructure of 3.0 wt% Si GO electrical steel and observed that Goss grains nucleated within in-grain shear bands were more closely oriented to the exact Goss orientation than those found at the grain boundaries. Xu et al. [125] reported that Goss grains nucleated within the shear bands and at the grain boundaries of deformed γ -fibers during the annealing of 6.5 wt% Si GO electrical steel.

Despite the numerous observations made of Goss grain nucleation within shear bands during primary recrystallization, accurate modeling of recrystallization to clarify the precise nucleation mechanism of the Goss

grains remains a challenge. To simulate recrystallization for GO electrical steel, deformation-induced microstructural heterogeneities, including shear bands, have to be understood. In addition to deformation modeling, prediction of orientations that will be formed during recrystallization will be required.

This chapter aimed to investigate the origin of Goss during the primary recrystallization of GO electrical steel. Both experimental and numerical schemes were used to reproduce nucleation at the early stage of primary recrystallization. The test specimen, initially hot-rolled, was subjected to severe plastic deformation followed by a short and low heat treatment. Texture evolutions at each step were characterized using various experimental methods. To complement the experimental findings, the experimental procedure was numerically reproduced using the proposed integrated CP-PF model. Microstructural heterogeneities induced by severe plastic deformation during the cold rolling were simulated by CPFEM, in which plastic deformation was assumed to originate from dislocation slips and shear band formations. Rolling texture, dislocation evolution, crystallographic orientations at which shear bands are activated, and the role of shear bands as preferred nucleation sites are discussed in this chapter. Subsequently, the GSERM model, implemented in PFM, was applied to predict the recrystallization texture of GO electrical steel, based on the results of CPFEM. The PFM then proceeded to predict microstructure evolution during the

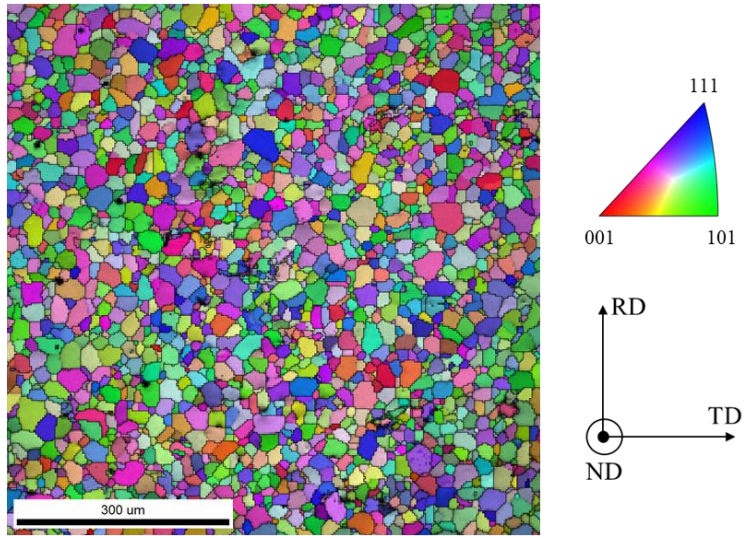
primary recrystallization of GO electrical steel. The relationship between the main texture components that determine the characteristics of GO electrical steel and shear bands is discussed. For validation purposes, the cold-rolled and recrystallized microstructures characterized by experiments were compared with those calculated by the developed model, thereby establishing the validity and accuracy of this approach.

4.2. Experimental methods

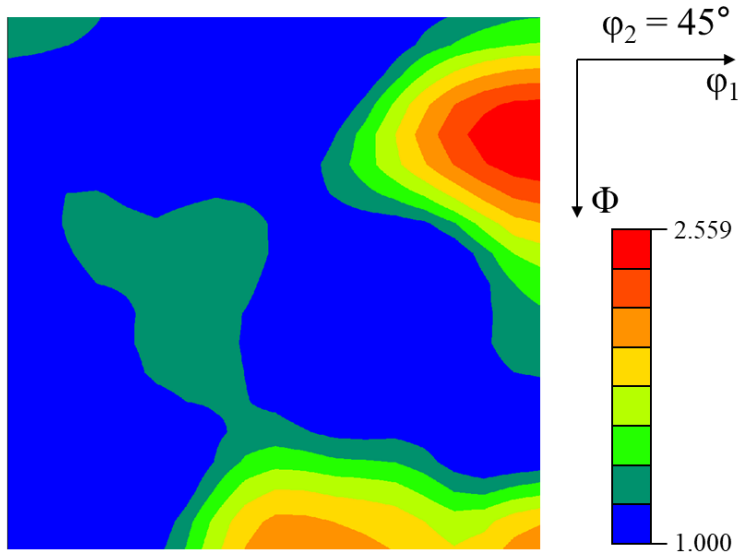
4.2.1. Material

The material studied was GO electrical steel, which contained 3.24 wt% Si. The steel was produced via vacuum melting, followed by hot rolling and hot band annealing heat treatment. The initial thickness of the steel before it underwent cold rolling was 2.92 mm.

The microstructure of GO electrical steel before it was cold rolled was characterized using electron backscatter diffraction (EBSD). Figs. 4-1(a) and (b) show the inverse pole figure (IPF) in the ND and $\varphi_2=45^\circ$ section of the orientation distribution function (ODF), respectively. Fig. 1 indicates that the microstructure mainly comprises Copper $\{112\}\langle 111\rangle$, Brass $\{110\}\langle 112\rangle$, and Goss $\{110\}\langle 001\rangle$ texture components as typically found in the commonly available hot-rolled electrical steels [126–128].



(a)



(b)

Fig. 4-1. (a) Normal direction inverse pole figure map and (b) $\phi_2=45^\circ$ section of orientation distribution function of hot-rolled GO electrical steel.

4.2.2. Mechanical tests

The uniaxial tensile test was conducted to measure the basic mechanical properties of the test material using the universal testing machine Instron™ 5582. To measure the strain in the specimen, a digital image correlation system (DIC) was used. The tensile test was conducted in accordance with the standard ASTM E8 subsize specimens along the RD under a quasistatic condition with strain rate of 0.001 s^{-1} . The measured mechanical properties of the GO electrical steel are listed in Table 4-1.

Table 4-1. Basic mechanical properties of the investigated grain-oriented electrical steel.

Young's modulus (GPa)	Poisson's ratio	Yield strength (MPa)	Tensile strength (MPa)	Uniform elongation (%)
197	0.3	527	748.9	12.2

4.2.3. Microstructure characterization

The microstructure analysis of the recrystallized specimen was performed using several characterization methods. First, the primary recrystallization of GO electrical steel was facilitated by cold rolling it at a thickness reduction ratio of 76%, followed by its annealing at 600 °C. Heat treatment was applied to the specimen within 60 s to examine nucleus formation in it at the early stage of its primary recrystallization. The heat treatment was applied using a dilatometer (R&B Inc., South Korea) at a heating rate of 30 °Cs⁻¹. The methods employed for microstructure characterization are detailed as follows:

X-ray diffraction: The cold rolling texture of GO electrical steel was measured using X-ray diffraction (XRD). An X-ray diffractometer (SmartLab, Rigaku, Japan) with MoK α radiation (wavelength $\lambda=0.711$ nm) was used for the measurements, and the three pole figures obtained, namely, (110), (200), and (211), were analyzed. The specimens were polished using SiC grinding paper with grit sizes in the range 400–1200 grit. The specimens were polished with a cloth using 1 μ m diamond suspension, followed by 0.02 μ m colloidal silica. The ODF was calculated using software Textools v3.3 developed by Resmat [129].

Electron backscatter diffraction: The crystallographic orientation data of as-received and the partially recrystallized GO electrical steel specimen

were measured using an EBSD detector (HIKARI, EDAX/TSL, USA) mounted on a field emission scanning electron microscope (FE-SEM:SU-70, Hitachi, Japan). To facilitate recrystallization, the cold-rolled specimen was heat treated at 600 °C for 60 s. The specimen preparation process was same as that followed with the XRD specimen. The specimen was scanned by a 20 kV electron beam with a step size of 1.7 μm. The ODF was represented using the generalized harmonic function introduced by Bunge and expanded to a rank of 16. The analysis was performed using software OIM Analysis 7.3.

Transmission electron microscopy: The recrystallized nucleus at the early stage of primary recrystallization was experimentally measured using the ASTAR orientation imaging system (NANOmeGas, Belgium) mounted on a transmission electron microscope (JEM-2100F, JEOL, Japan). After heat treatment at 600 °C for 2 s, the transmission electron microscopy (TEM) specimens were obtained from the region where the shear bands were activated (Fig. 4-2(a)) using a focused ion beam (FIB) system (Helios 650, FEI, USA). The scanning electron microscopy (SEM) images of the FIB milling target area and TEM specimen are shown in Figs. 4-2(b) and (c), respectively.

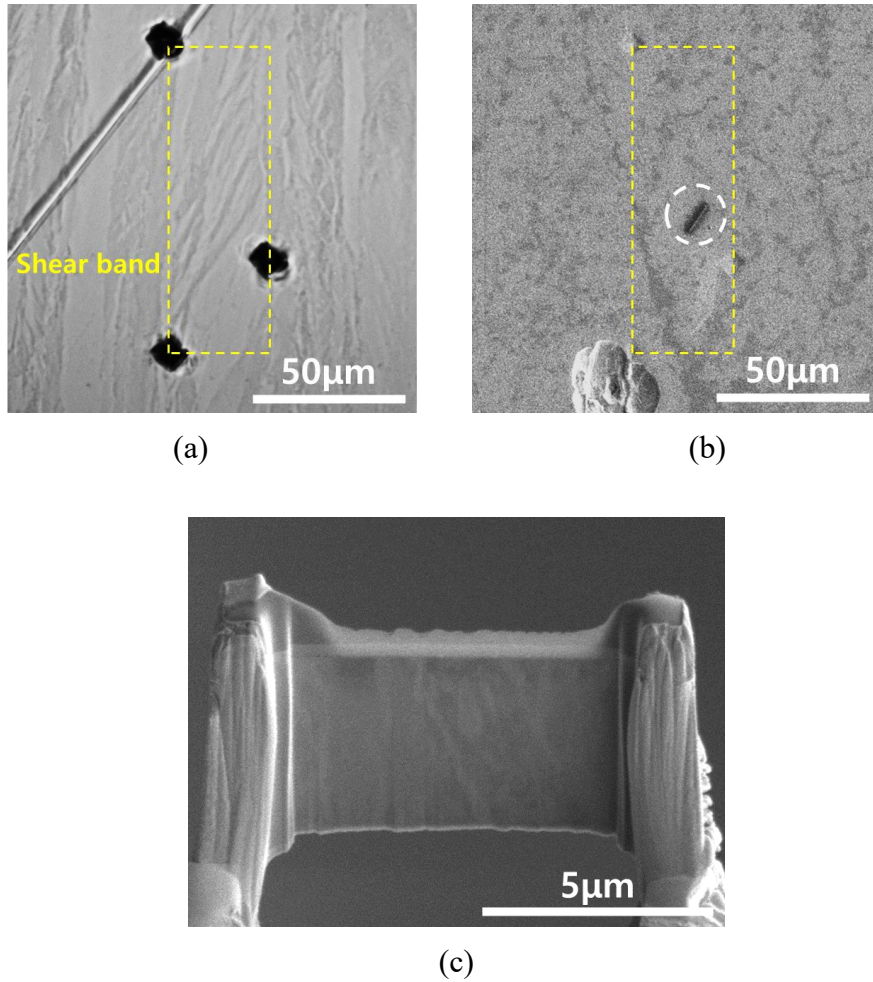


Fig. 4-2. (a) Optical microscope image of the region with activated shear bands (TD section), (b) scanning electron microscope image of the focused iron beam milling target area (white circle), and (c) transmission electron microscope sample obtained using focused ion beam milling.

4.3. Results and discussion

4.3.1. Constitutive parameter identification

The constitutive parameters, described in Section 2.2, of GO electrical steel were determined. The parameters associated with intrinsic material properties (C_{11} , C_{12} , C_{44} , G^0 , b , ν), plastic shear strain rate (Q_0 , ν_0), and grain boundary hardening (H^α) were obtained from those used for ultra-low carbon steel in Chapter 3, taking into account the similar level of carbon content (below ~0.1 wt%). To account for the effects of silicon atoms on solid solution hardening behavior, $\cos\phi_c$ were determined based on Hull and Bacon [67], while C were obtained from experimental data. Average grain diameter (d_g) was obtained from the microstructure, as characterized by EBSD, shown in Fig. 4-1. Shear band parameters ($\dot{\gamma}_0^z$, τ_0^z , and μ), which rarely have to play a role during uniaxial tension, were found to be in line with the findings of Hölscher et al. [130], Nguyen-Minh et al. [131], and Chen et al. [132]. This suggests that the shear bands are initiated at a thickness reduction ratio of ~50% and evolved to the maximum at a thickness reduction ratio in the range 70%–80%. $\rho_{0,edge}$ and $\rho_{0,screw}$ were calculated employing the same approach as those used for ultra-low carbon steel, elaborated upon in Section 3.3.1. The other sets of parameters could be determined by fitting the uniaxial tensile stress-strain curve and load data during cold rolling of the

specimen. Because of the limited uniform elongation of the GO electrical steel (~12.3%), the constitutive parameters of the CP model that were determined were extrapolated to be used for large plastic deformation, such as rolling deformation. The identified constitutive parameters are listed in Table 4-2.

Table 4-2. Constitutive model parameters of the investigated grain-oriented electrical steel.

$\cos \phi_c$	C	d_g	$\rho_{0,edge}$	$\rho_{0,screw}$
0.032	0.062 at.%	31.6 μm	$4.0 \times 10^{12} \text{ m}^{-2}$	$2.0 \times 10^{13} \text{ m}^{-2}$
$\dot{\gamma}_0^z$	τ_0^z	μ	c_1^*	c_2^*
$1.0 \times 10^{-4} \text{ s}^{-1}$	1200 MPa	0.03	0.131	0.37
c_3^*	c_4^*	c_5^*	R_{edge}^*	R_{screw}^*
1.21	1.57	2.43	33.36 nm	145.49 nm

* Fitting parameters used in the dislocation density-based hardening model

Fig. 4 shows the comparison of the fitted stress-strain curve with the curve obtained using the measured stress and strain values. From the figure, the identified constitutive parameters are in agreement with experimental data.

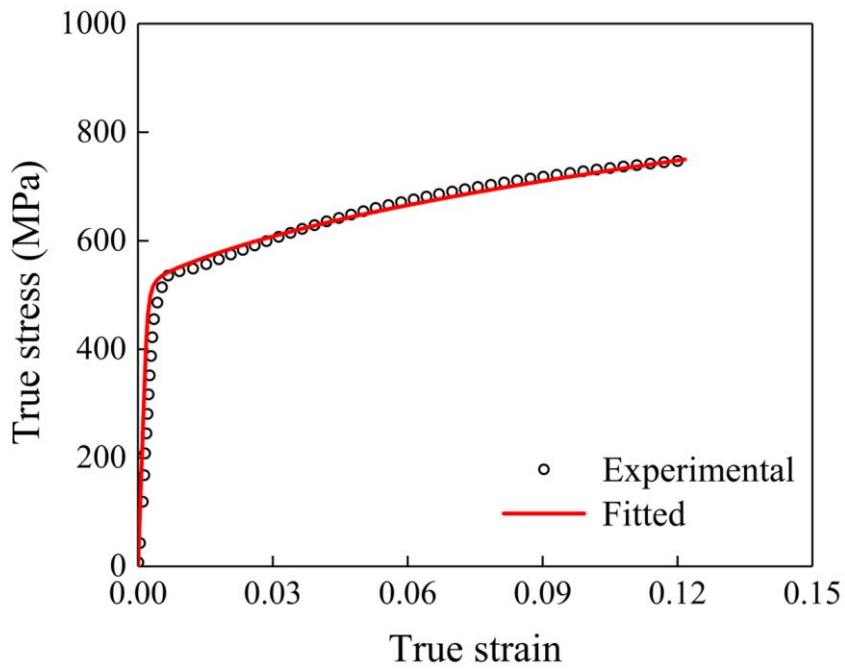


Fig. 4-3. Comparison of CP calculated stress-strain curve with measured one for the grain-oriented electrical steel.

4.3.2. Simulation of cold-rolled GO electrical steel

The RVE approach was adopted to simulate the mechanical response of the polycrystalline GO electrical steel. The microstructural characteristics of GO electrical steel presented in Fig. 4-1 were statistically analyzed. The crystallographic orientations and grain sizes were thereafter distributed in the RVE, detailed in Section 2.2.5.

Because shear bands had a thickness of only few micrometers, two distinctively sized RVE models were explored for computational efficiency: (1) RVE₂₂₄ model with 224 grains to simulate the macroscopic behavior of the cold rolling process and (2) RVE₁₈ model with 18 grains to simulate the deformation heterogeneities caused by shear band formation in the microscopic area. The side length and the number of elements of the RVE₂₂₄ model were 300 μm and 27,000 ($30 \times 30 \times 30$) elements, respectively, while those of the RVE₁₈ model were 60 μm and 27,000 ($30 \times 30 \times 30$) elements, respectively (Fig. 4-4).

As for the boundary conditions of RVE models, the plane strain compression condition was imposed as a simplified loading equivalent to the typical cold rolling process. The displacement in the TD was kept constant, and compressive loading was applied along the ND. To validate the developed CP model, the thickness reduction ratios of 76% and 90% were compared

with those in the experiments. Additionally, PBCs, as elaborated in Section 2.2.5, were also applied to the RVE to ensure its physical continuity.

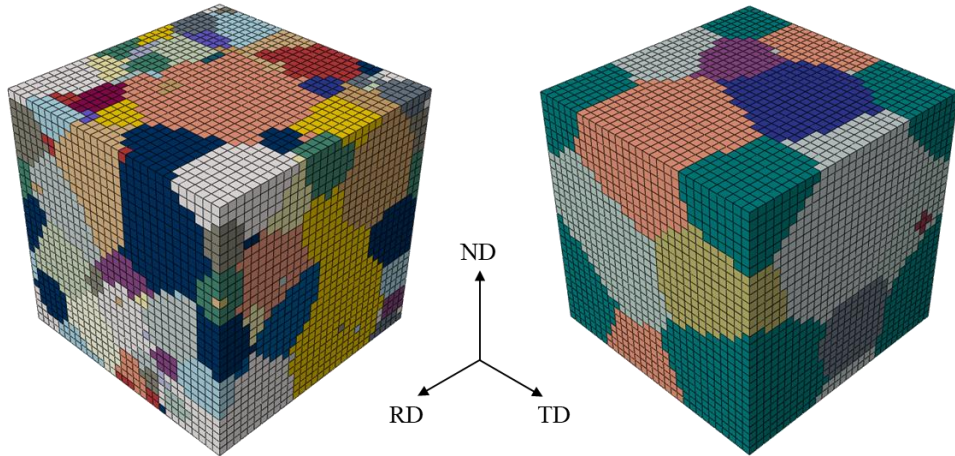


Fig. 4-4. Dual-scale cubic representative volume element models for GO electrical steel: RVE₂₂₄ model on the left side and RVE₁₈ model on the right side.

This section presents the results of texture development and microscopic deformation of cold-rolled GO electrical steel. The two RVEs were used to distinguish the deformation behavior of different scales. For example, the large-scale RVE₂₂₄ model can be used to capture the overall rolling texture evolution and related plastic deformation responses. The RVE₁₈ model can be used to capture the microscopic behavior of shear band formation and

evolution during cold rolling. Fig. 4-5 displays the deformed RVEs and their equivalent plastic strains with a thickness reduction ratio of 76% and 90%.

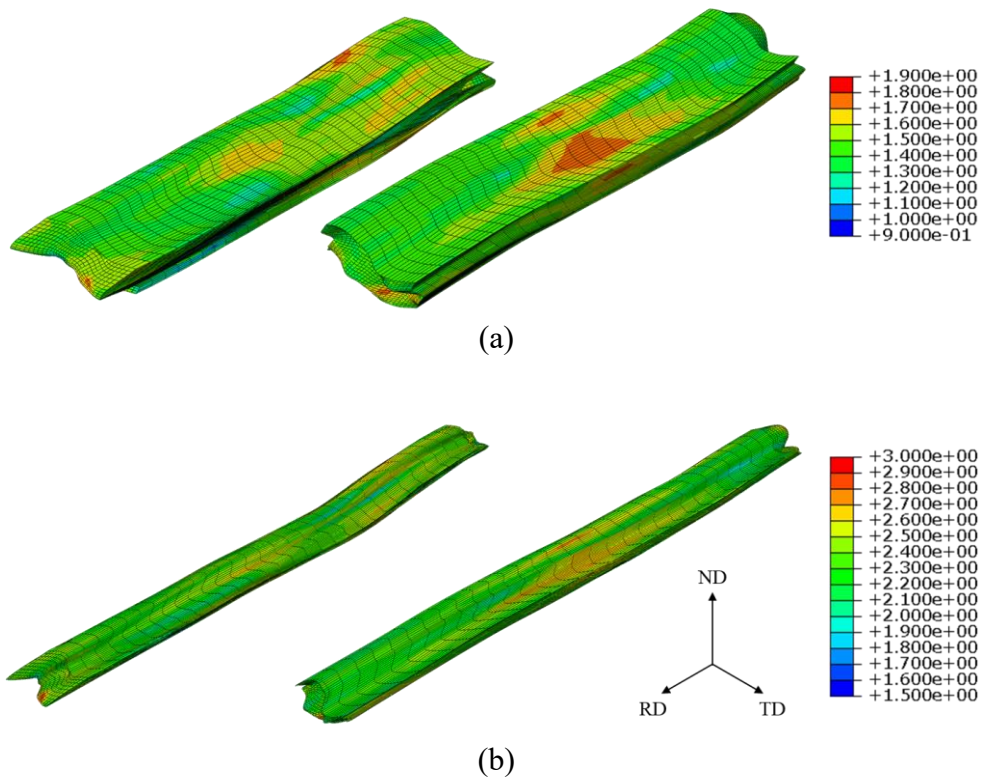


Fig. 4-5. Deformed representative volume elements (RVEs) and their equivalent plastic strains. (a) Results after achieving a thickness reduction ratio of 76%, with RVE₂₂₄ model on the left side and RVE₁₈ model on the right side. (b) Results after a achieving a thickness reduction ratio of 90%, with RVE₂₂₄ model on the left side and RVE₁₈ model on the right side.

Large-scale CP simulation using the RVE₂₂₄ model

Figs. 4-6(a) and (c) and Figs 4-6(b) and (d) show the $\varphi_2=45^\circ$ ODF sections of cold-rolled GO electrical steel after a thickness reduction ratio of 76% and 90%, respectively. Figs. 4-6(a) and (b) also show the texture obtained using XRD, while Figs. 4-6(c) and (d) show the CP-simulated texture obtained using the macroscopic RVE₂₂₄. The predicted rolling textures were similar to the measured textures for thickness reduction ratios of 76% and 90%. However, the calculated textures are distributed more widely than the measured textures owing to the underprediction of texture component intensity. This underestimation may have been caused by the difference between the boundary conditions of the RVE-based simulation and those of the actual cold rolling process. The cold rolling process involves both plane strain and shear-dominant modes although CP simulation was simplified as plane strain compression. The proportional deformation of plane strain compression can be efficiently used to simulate the main characteristics of the rolling process, but the microstructure heterogeneities induced during an actual rolling process can become underestimated. Nevertheless, at a 76% thickness reduction ratio, the experimentally measured main texture components, namely, $\{001\}\langle 110\rangle$, $\{558\}\langle 110\rangle$ (approximated as $\{112\}\langle 110\rangle$), $\{665\}\langle 110\rangle$ (approximated as $\{111\}\langle 110\rangle$), and $\{111\}\langle 112\rangle$, were reasonably predicted. Moreover, when cold rolling thickness reduction

ratio was increased from 76% to 90%, the developed $\{001\}\langle 110\rangle$ and $\{111\}\langle 110\rangle$ components were perfectly captured by the proposed model (Fig. 4-6(d)). The small-scale (or microscopic) RVE_{18} model used for predicting shear band evolution, was assigned its orientations using the large-scale (or macroscopic) RVE_{224} model, to represent the cold rolling texture calculated.

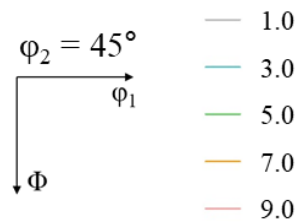
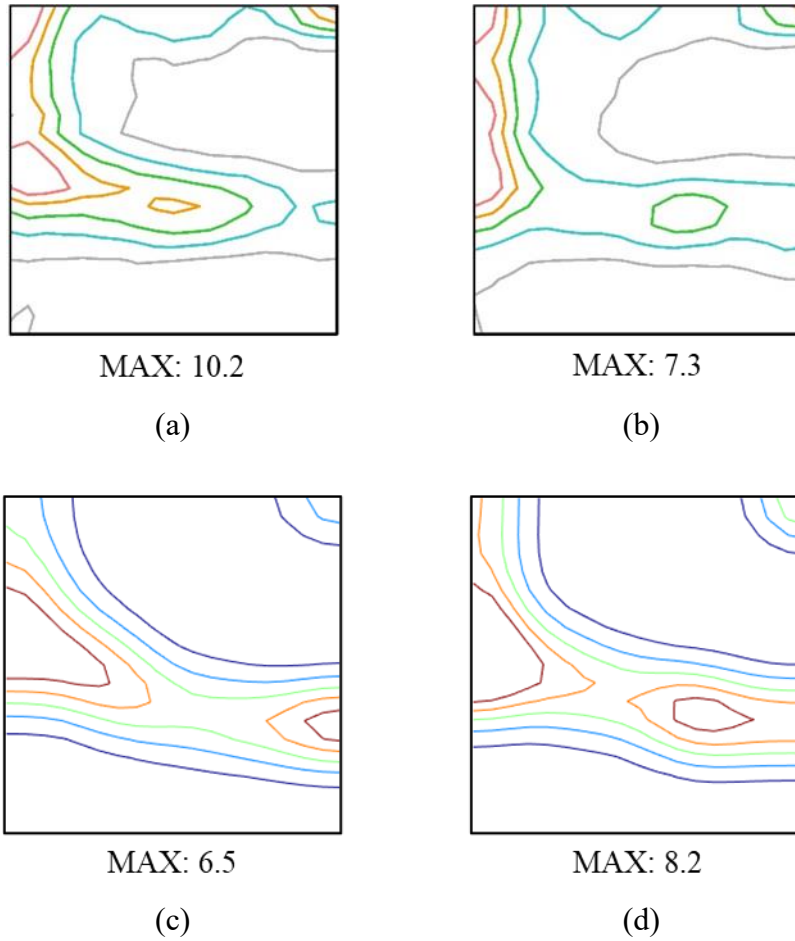


Fig. 4-6. $\varphi_2=45^\circ$ ODF sections of cold-rolled GO electrical steel. (a, b) Rolling texture measured using XRD analysis after a thickness reduction ratio of 76% and 90%, respectively. (c, d) Rolling texture predicted through CP finite element analysis using the macroscopic RVE₂₂₄ model after a thickness reduction ratio of 76% and 90%, respectively.

The evolution of the dislocations during cold rolling was examined using the large-scale RVE₂₂₄ model. Two arbitrary grains within the RVE were randomly selected to examine the heterogeneity of the dislocation densities. Figs. 4-7(a) and (b) show the evolution of edge and screw dislocation densities of the two grains selected from two different locations: grain boundary and grain interior regions. Because of severe plastic deformation caused owing to cold rolling, dislocation densities exponentially increased as the thickness reduction ratio increased. The edge dislocation density increased to $\sim 10^{16} \text{ m}^{-2}$ at a thickness reduction ratio of 90%. However, in screw dislocations, the increase was approximately one order less than that in edge dislocations. This is probably due to the increased active recovery (or annihilation) process of screw dislocations resulting in cross slips.

Figs. 4-7(c) and (d) show the ratio of screw component to edge component (or dislocation fractions, screw/edge) in the two selected grains. The density of the screw dislocations, which was initially at a level similar to that of the edge dislocation, was $\sim 20\%$ lower than that of the edge dislocations at a 90% thickness reduction ratio, mainly due to the rapid increase of edge dislocations with deformation. Because of this result and the symmetry of the stress fields of the screw dislocations, only the stress fields of the arrayed edge dislocations will be considered in the calculation of the recrystallization texture in Section 4.3.3.

The simulated results of dislocation density evolutions for edge and screw components were similar to the observations made by Takaki et al. [92]. For subsequent validation, edge and screw dislocation densities were evaluated before and after cold rolling. To measure dislocation densities, the modified Williamson-Hall method, based on the full width at half maximum (FWHM) analysis, was applied to the obtained XRD peaks of each specimen [93,133,134]. Detailed measurement methods can be found in the Appendix C. The measured results indicate that the edge and screw dislocation densities in the specimen before cold rolling were $1.6 \times 10^{13} \text{ m}^{-2}$ and $4.86 \times 10^{13} \text{ m}^{-2}$, respectively. After a 76% thickness reduction, the edge and screw dislocation densities were found to be $3.79 \times 10^{15} \text{ m}^{-2}$ and $1.37 \times 10^{15} \text{ m}^{-2}$, respectively. Thus, it can be concluded that the initial dislocation densities used in the simulation and the evolved dislocation densities resulting from the cold rolling simulation were found to be reasonable.

Due to the intergranular heterogeneities resulting from multiple slip activities with different grain orientations, dislocation densities in the grain boundary region (indicated in red in Fig. 4-7) were larger than those in the grain interior region (indicated in blue in Fig. 4-7). The simulated dislocation density distribution is similar to the commonly reported dislocation pile-up at grain boundaries, which could be captured by the incompatibility between any two neighboring grains with different orientations or slip activities. The

intensified dislocation densities in the grain boundary region can also affect the recrystallization behavior.

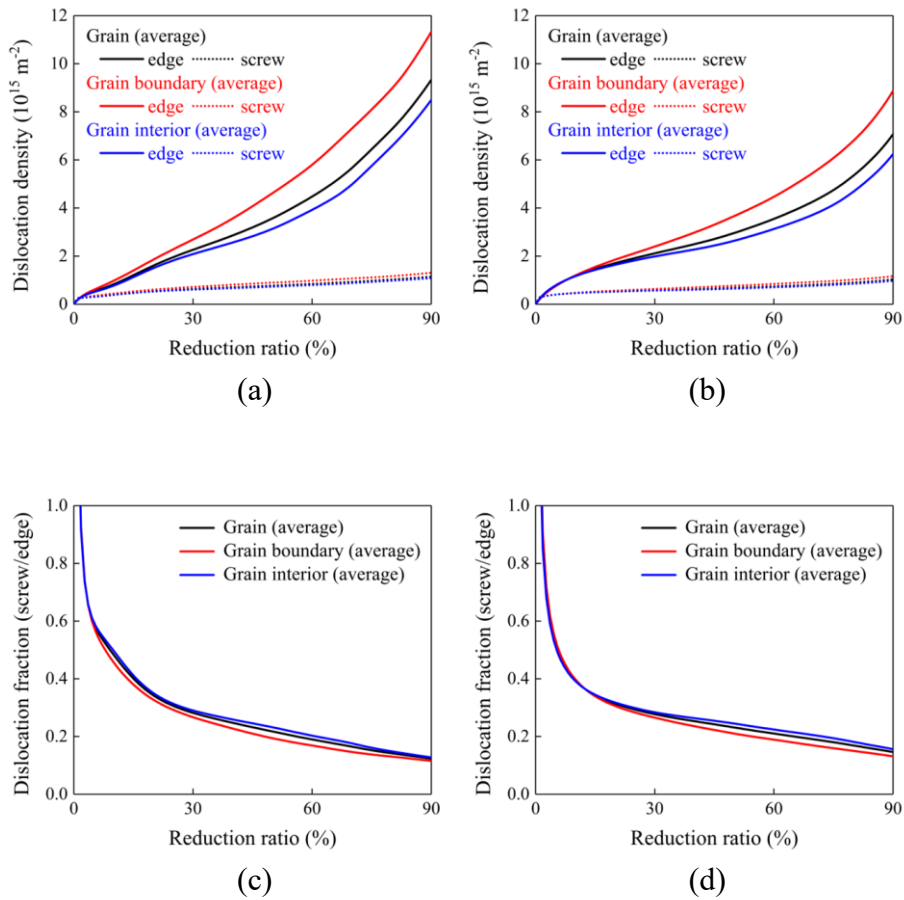


Fig. 4-7. (a, b) Evolution of the edge and screw dislocation densities and (c, d) screw/edge dislocation fraction of two selected grains in the grain boundary and interior regions, respectively.

Small-scale CP simulation using the RVE₁₈ model

The shear bands, known to be formed in extremely localized areas, cause deformation heterogeneities. Therefore, a high-resolution computational model is required to predict the formation and evolution behavior of the shear bands. That is, in a large-scale model, for example, in the RVE₂₂₄ model formulated in this chapter, the activation of shear bands may appear only in a few finite elements and thus can lead to underestimated results. Thus, in this chapter, to capture the evolution of shear bands during cold rolling, the small-scale (microscopic) RVE₁₈ model was used. To make the results consistent with those of the previously used large scale RVE₂₂₄ model, crystal orientations used in the macroscopic RVE₂₂₄ model in the designated local area were used.

Fig. 4-8 shows the accumulated shear strain for the shear band (γ^z) of the small-scale RVE₁₈ model and its grains with obvious shear bands after a thickness reduction ratio of 76%, which are depicted in the undeformed configuration for visual clarity. To identify activated shear band elements, the accumulated shear band strain of 10^{-6} was used. Because of the localized nature of shear band formation, only 3.73% of the elements in the RVE₁₈ model had activated shear bands.

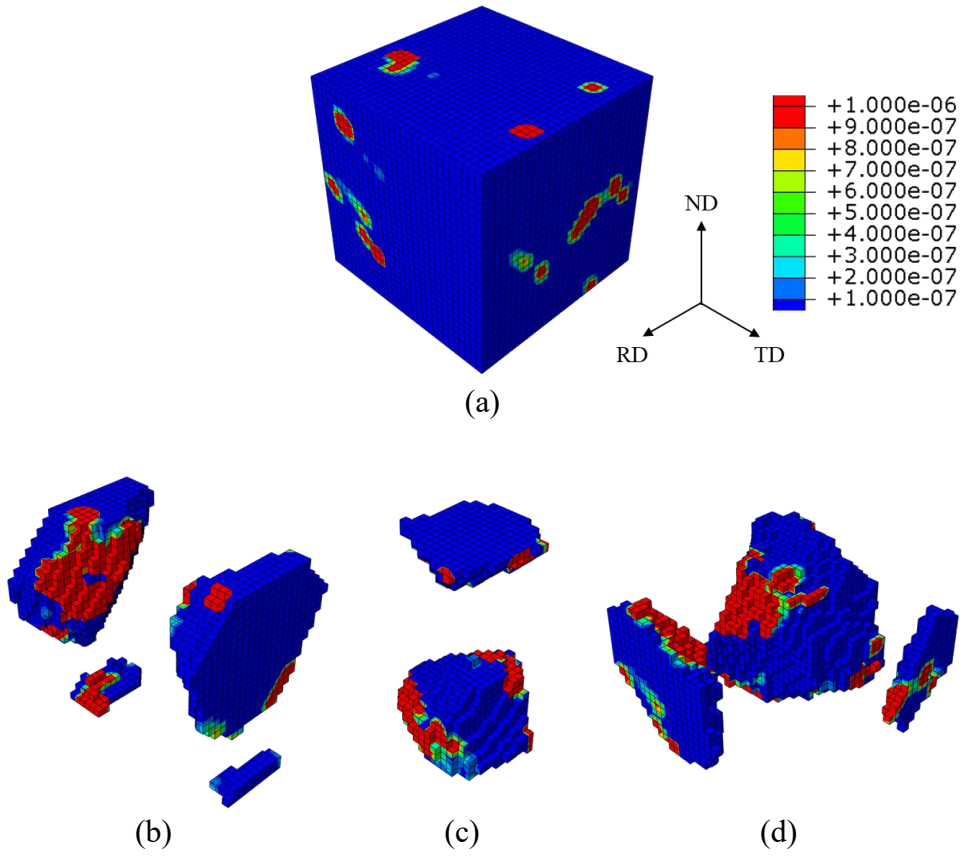


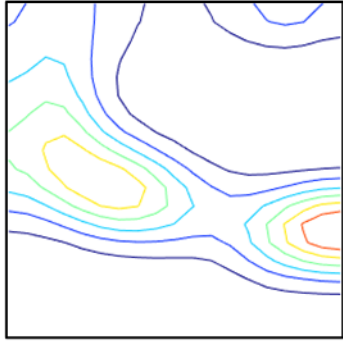
Fig. 4-8. Accumulated shear strain for shear band (γ^z) of (a) the small-scale RVE₁₈ model and (b, c, d) grains with obvious shear bands after a thickness reduction ratio of 76%. For visual clarity, contours have been mapped in the undeformed configuration.

Figs. 4-9(a) and (b) show the $\varphi_2=45^\circ$ ODF sections of cold-rolled GO electrical steel predicted using the microscopic RVE₁₈ model after thickness reduction ratios of 76% and 90%, respectively. Although the number of grains in the model is inadequate to fully represent the microstructure, the overall tendency of the deformation texture is similar to the results obtained using the RVE₂₂₄ model (Figs. 4-6(c) and (d)). The $\{001\}\langle 110\rangle$ component shown in Figs. 4-9(a) and (b) particularly matches the experimental components (Figs. 4-6(a) and (b)).

To further validate the proposed CP model, the effect of the rolling texture on shear band formation was examined. Only the orientations of elements with obvious shear bands (accumulated shear band strain exceeding 10^{-6}) were selected and displayed in Figs. 4-9(c) and (d) for 76% and 90% thickness reduction ratios. The cold rolling textures of the elements without shear bands are shown in Figs. 4-9(e) and (f) for 76% and 90% thickness reduction ratios, respectively.

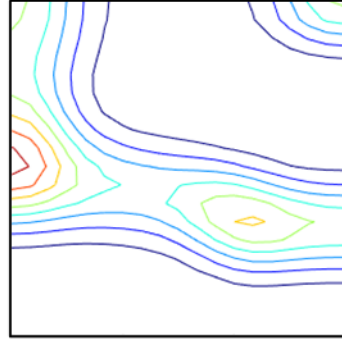
Figs. 4-9(c) and (d) show that the texture components with γ -fibers centered on $\{111\}\langle 112\rangle$ are highly related to the active shear bands in the simulation. Although the texture component intensities at the two thickness reduction ratios are marginally different, the $\{111\}\langle 112\rangle$ texture component has an obvious major peak for shear band activation. As shown in Figs. 4-9(e) and (f), not all γ -fibers can activate shear bands because the orientations

without shear bands also share some γ -fibers. Their ODFs appear to be similar to the overall ODF of the cold-rolled RVE₁₈ model in Figs. 4-9(a) and (b). This observation made through CP simulation explains that shear bands become active and evolve when local deformation is concentrated in specific γ -fibers, as shown in Figs. 4-9(c) and (d). In this study, the γ -fiber with the $\{111\}\langle 112\rangle$ component may play the most significant major role in activating the shear bands of GO electrical steel [122].



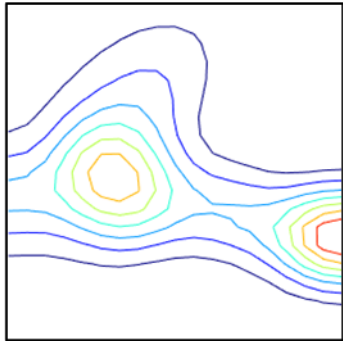
MAX: 6.6

(a)



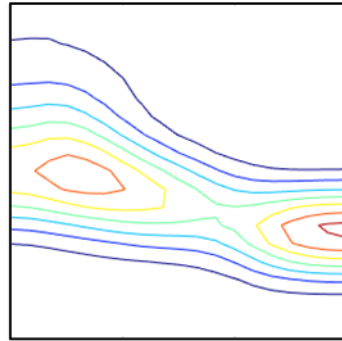
MAX: 7.3

(b)



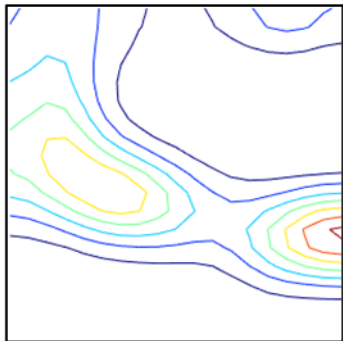
MAX: 7.7

(c)



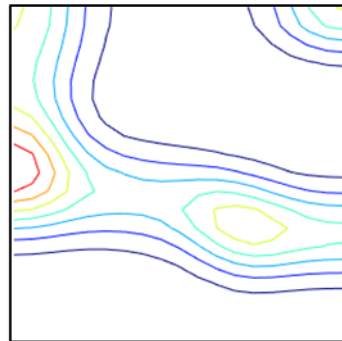
MAX: 6.6

(d)



MAX: 6.6

(e)



MAX: 7.9

(f)

(caption on next page)

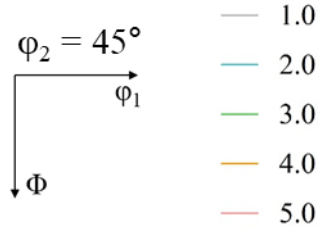


Fig. 4-9. $\phi_2=45^\circ$ ODF sections of cold-rolled GO electrical steel predicted by the CP using the small-scale RVE₁₈ model. (a, b) Rolling texture after a thickness reduction ratio of 76% and 90%, respectively. (c, d) Rolling texture in the shear band activated elements after a thickness reduction ratio of 76% and 90%, respectively. (e, f) Rolling texture in the elements without shear bands after a thickness reduction ratio of 76% and 90%, respectively.

The effect of shear band activation on dislocation slip activities was examined by conducting simulation using the small-scale RVE₁₈ model. Fig 4-10 presents the evolution of the total dislocation densities in the regions with and without shear bands as the rolling reduction ratio increases. At the beginning of rolling, the total dislocation densities in the two regions were almost same. However, as the thickness reduction ratio reached $\sim 30\%$, the difference between the total dislocation densities in the two regions gradually increased, and at a thickness reduction ratio of 90%, it had almost doubled. Moreover, the model without shear bands produced almost the same dislocation density as the large-scale RVE₂₂₄ model (Figs. 4-7(a) and (b)). The simulated results indicate that shear bands are activated at locations where

deformation is locally concentrated and that they lead to increased slip activities.

Because stored energy, the driving force of recrystallization, is highly associated with the dislocation density, a microstructure with a high dislocation density can serve as the preferred nucleation site during primary recrystallization. That is, microscopic sites with activated shear bands can serve as preferred nucleation sites, as further discussed in Section 4.3.3.

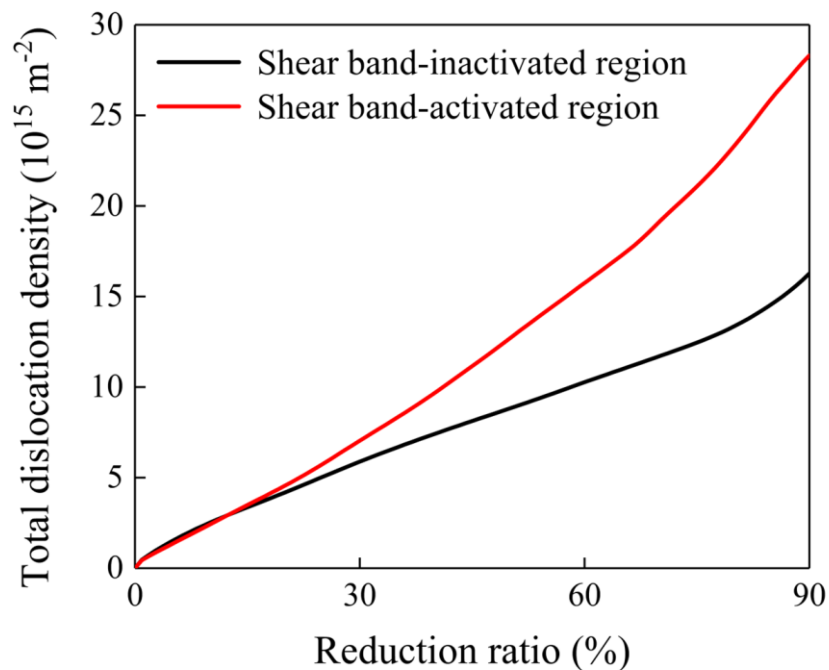


Fig. 4-10. Evolution of total dislocation densities in the regions with and without shear band activation.

4.3.3. Simulation of recrystallized GO electrical steel

To study the nucleation behavior during primary recrystallization, the microstructure characteristics of cold-rolled GO electrical steel heat treated at 600 °C for 60 s and 2 s were determined using EBSD and TEM, respectively. Because heat treatment was conducted within a short time and at low temperature, only sites with high stored energy underwent recrystallization. In this section, the role of shear bands serving as preferred nucleation sites of Goss grain are presented. Furthermore, the ability of the developed model with shear band activation to predict recrystallized grain orientations was confirmed.

Goss grains present in the shear bands during primary recrystallization

Fig. 4-11 presents the IPF maps of cold-rolled GO electrical steel subjected to heat treatment at 600 °C for 60 s obtained using the EBSD method. The ND IPF map in Fig. 4-11(a) shows that only a part of the specimen with highly accumulated stored energy could be recrystallized through heat treatment. Recrystallized grains can be readily differentiated from the remaining deformed grains due to their equiaxed shapes. The residual deformed grains were elongated along the RD, taking a fibrous form, which is a typical characteristic for metals that have undergone cold rolling.

The unindexed black regions shown in Fig. 4-11(a) result from severe lattice distortion and high stored energy and include the shear bands induced by locally concentrated severe deformation. It is noted that most of the unindexed regions are concentrated in the γ -fibers, which are shown in blue in Fig. 4-11(a). These results are consistent with the results predicted by the CP model because, as discussed in Section 4.3.2, shear bands are activated in γ -fibers centered on the $\{111\}\langle 112\rangle$ component.

Despite the short heat treatment time, many grains with varying orientations were newly nucleated, as shown in Fig. 4-11(a). Figs. 4-11(b) and (c) display the ND and RD IPF maps, respectively, by enhancing the visual clarity of Goss grains while suppressing the other texture components, except for Goss grains. The yellow dotted lines in Figs. 4-11(b) and (c) indicate the shear bands. Most of the Goss grains were intensively nucleated along the directions of the evolved shear bands. Because the shear bands were observed mainly in γ -fibers, the Goss grains would have originated owing to the deformation heterogeneities of the γ -fibers. Moreover, shear bands can be preferred nucleation sites for recrystallized grains at the early stage of primary recrystallization because of the high amount of stored energy they possess.

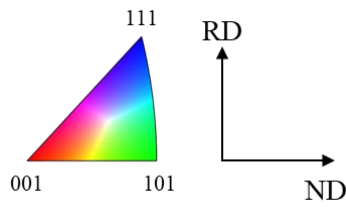
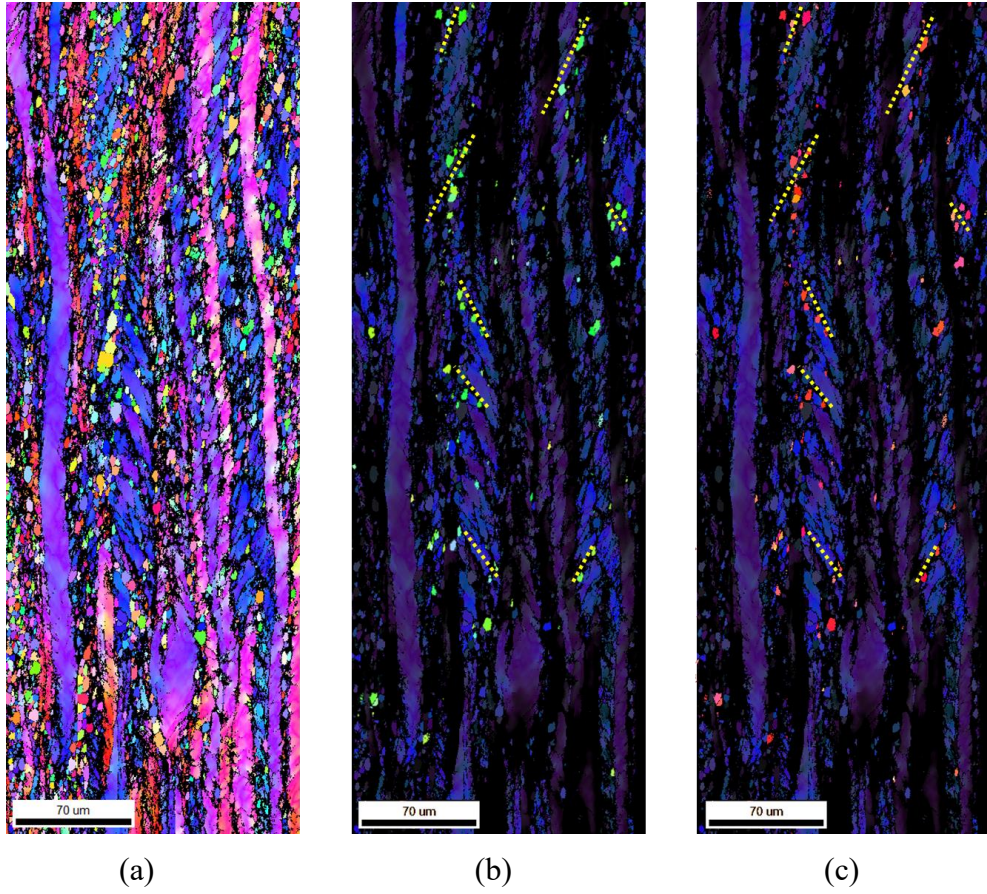


Fig. 4-11. (a) Normal direction (ND) inverse pole figure (IPF) map of cold-rolled GO electrical steel subjected to heat treatment at 600 °C for 60 s. (b) ND IPF map and (c) rolling direction IPF map in which other texture components except Goss have been suppressed to highlight the Goss texture. In (b) and (c), the yellow dotted lines indicate the shear bands.

To investigate the origin of the Goss grains, TEM-based orientation mapping was conducted on the specimen taken from γ -fiber of cold-rolled GO electrical steel heat treated at 600 °C for 2 s. Fig. 4-12 shows a newly nucleated equiaxed Goss grain within the shear band with the $\{111\}\langle 112\rangle$ component. Figs. 4-12(a) and (b) show the ND and RD IPF maps, respectively, and Fig. 4-12(c) displays a confidence index (CI) map [135]. The CI is the parameter calculated as $CI = (V_1 - V_2) / V_{ideal}$ for the measured diffraction pattern by a voting scheme. V_1 and V_2 are the votes for the first and second solutions, and V_{total} is the total possible number of votes for a diffraction pattern. This value approaches 1 when the first solution has high reliability, while it approaches 0 when too many solutions exist for the given diffraction pattern. That is, the region with a low CI value has a measured diffraction pattern of low reliability because of severe plastic deformation. The IPF and CI maps shown in Fig. 4-12 confirm that the submicron-sized Goss grain was newly nucleated within the severely deformed shear band in the γ -fiber. These observations indicate that the severely deformed shear bands activated in the γ -fibers can be preferred nucleation sites for Goss grains during the early stage of primary recrystallization.

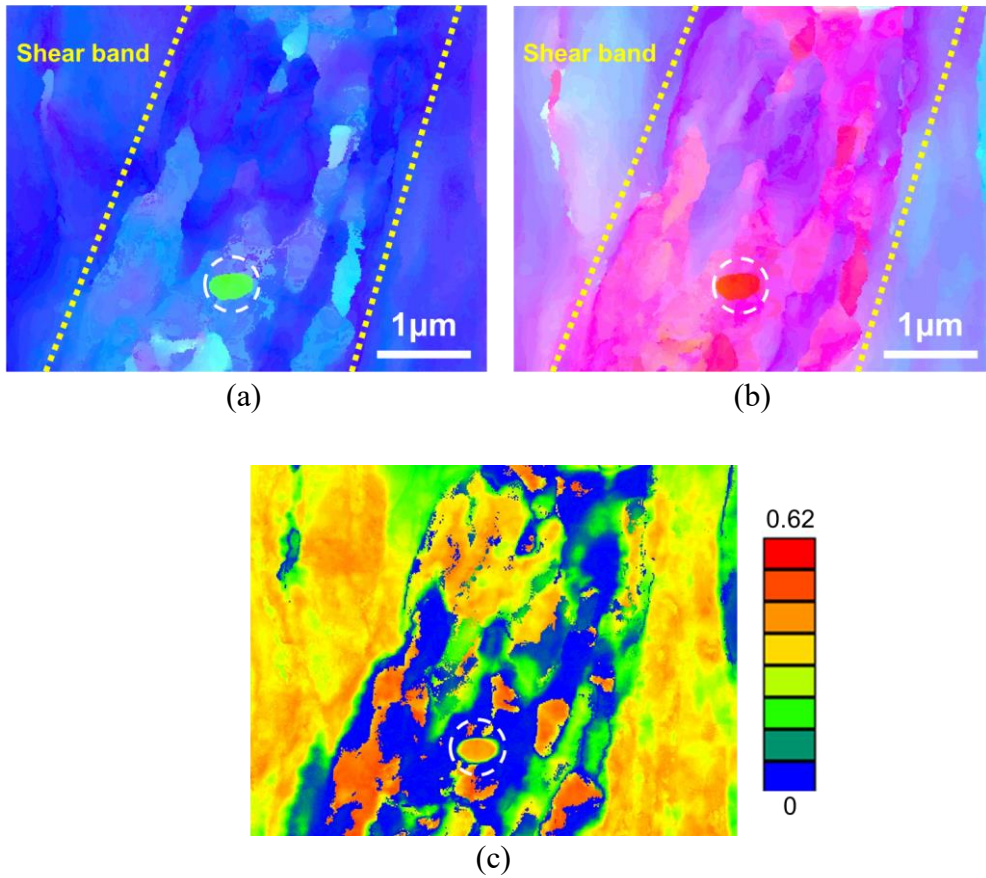


Fig. 4-12. Nucleation of Goss grain (white circle) within shear band (yellow dotted line) with the $\{111\}\langle 112\rangle$ component, measured using TEM orientation imaging. (a) Normal direction inverse pole figure (IPF) map, (b) rolling direction IPF map, and (c) confidence index map.

Prediction of recrystallization texture of cold-rolled GO electrical steel using the integrated CP-PF model

The recrystallization texture of cold-rolled GO electrical steel was predicted using the integrated CP-PF model and validated through EBSD measurements. The CP model provides the edge dislocation densities with active slip systems and rolling texture, except common finite element results, including stress- and strain-related variables. These results can be used as the inputs of the GSERM model. To include the effect of shear bands on the recrystallization texture, the results of small-scale RVE₁₈ model were used. The GSERM model calculates only the orientation probability when nucleation takes place, as it does not consider nucleation and grain growth during recrystallization. Thus, its integration with the PFM is necessary for accurately predicting recrystallization texture.

Figs. 4-13(a) and (b) show the nucleation orientation probabilities as predicted by the GSERM model in the regions with and without shear band activation, respectively. In the shear band activated region, the Goss, $\langle 100 \rangle //$ RD component, and γ -fiber centered on the $\{111\} \langle 110 \rangle$ component could be predicted as shown in Fig. 4-13(a). However, in the region without shear bands, a high intensity $\{111\} \langle 112 \rangle$ component was predicted as shown in Fig. 4-13(b). The evolution of the γ -fiber centered on the $\{111\} \langle 112 \rangle$ component during static recrystallization is a common characteristics of

recrystallized low carbon steel, as discussed in detail in Chapter 3. Therefore, specific texture components, such as the Goss texture, which play a key role in enhancing electrical steel performance, result from shear band evolution during cold rolling.

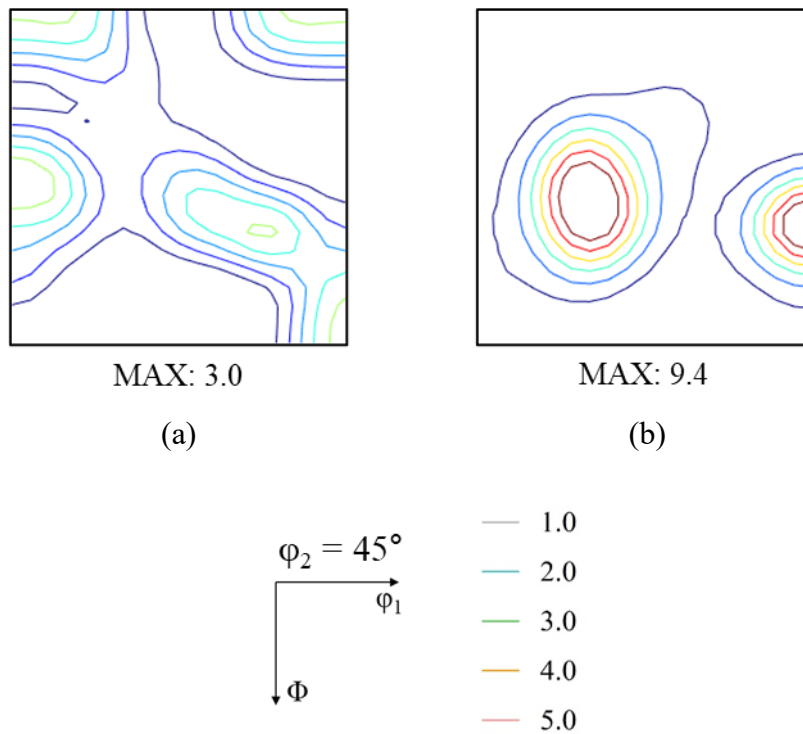


Fig. 4-13. Predicted nucleation orientation probabilities for recrystallized GO electrical steel in the regions (a) with shear bands and (b) without shear bands.

A more comprehensive investigation into the recrystallization texture of GO electrical steel was conducted utilizing the PFM. To distinctly ascertain the effect of shear bands on the recrystallization texture, a region with dominant shear band activation was targeted for PF modeling, as shown in Fig. 4-14. The state variables, which were calculated using the CPFEM within the shear band-dominant area, were numerically transferred onto PF grids using the proposed Wigner-Seitz mapping algorithm, discussed in detail in Section 2.4. Considering the similar level of carbon content (below ~ 0.1 wt%), the PF parameters used in the simulation were the same as those previously utilized for ultra-low carbon steel (Section 3.3.3), with the exception of Δx , which was set to $0.25 \mu\text{m}$. The time increment applied was 4.29×10^{-4} s, calculated based on the grid size.

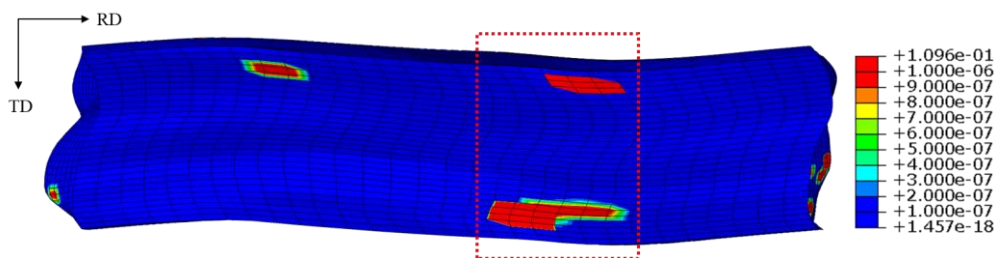


Fig. 4-14. Depiction of the target area for the PF simulation, indicated by the red dotted rectangle. The contour represents the accumulated shear strain for the shear band (γ^z), as predicted using the RVE₁₈ model.

Fig 4-15 depicts the progression of static recrystallization over time during the annealing process, as predicted by the PFM. The color coding within the grains corresponds to the ND IPF map. The orientations of newly nucleated grains were determined based on the nucleation orientation probability predicted using the GSERM model, as presented in Fig. 4-13. As a result of the high stored energy driven by the evolution of shear band, nucleation occurred at the early stage of annealing in the shear band activated regions, with an incubation time less than 1 s. Within the area targeted for PF simulation, complete recrystallization was achieved by 3.35 s. These predictions made through PF simulation align with experimental observations, where nucleation was found to occur in shear bands during short heat treatment (as seen in Fig. 4-11 and Fig. 4-12). Furthermore, even though a multitude of grains with varying orientations were newly nucleated, the Goss grains, represented in green in Fig. 4-15, occupied the most substantial area, centered around the shear band-dominant region. Through the PFM simulation, it was substantiated that shear bands can indeed serve as preferred nucleation sites for Goss grains during the initial stages of recrystallization.

Fig. 4-16(a) displays the recrystallization texture derived from the PFM simulation, while Fig. 4-16(b) shows the fully recrystallized texture of GO electrical steel obtained through EBSD measurements. Heat treatment was applied to the steel at 850 °C for 5 min. Both Figs. 4-16(a) and (b) show the

Goss, γ -fiber centered on the $\{111\}\langle 112\rangle$ component, and the $\langle 100\rangle//$ RD component. A comparison of Figs. 4-16(a) and (b) indicates that the developed integrated CP-PF model could successfully predict the main characteristics of recrystallized electrical steel with reasonable accuracy. If the conventional CP model is used without considering shear band formation, only the γ -fiber centered on the $\{111\}\langle 112\rangle$ component, indicated in Fig. 4-13(b), would be captured.

While the overall prediction quality is acceptable, the intensity of minor texture components remains underpredicted. This is primarily because the simulation employed a relatively small number of grains, which may not adequately represent the full intergranular heterogeneities inherent in a polycrystalline metal. This limitation could potentially be improved by implementing large-scale modeling, despite the associated high computational costs, which can be the topic of a future study.

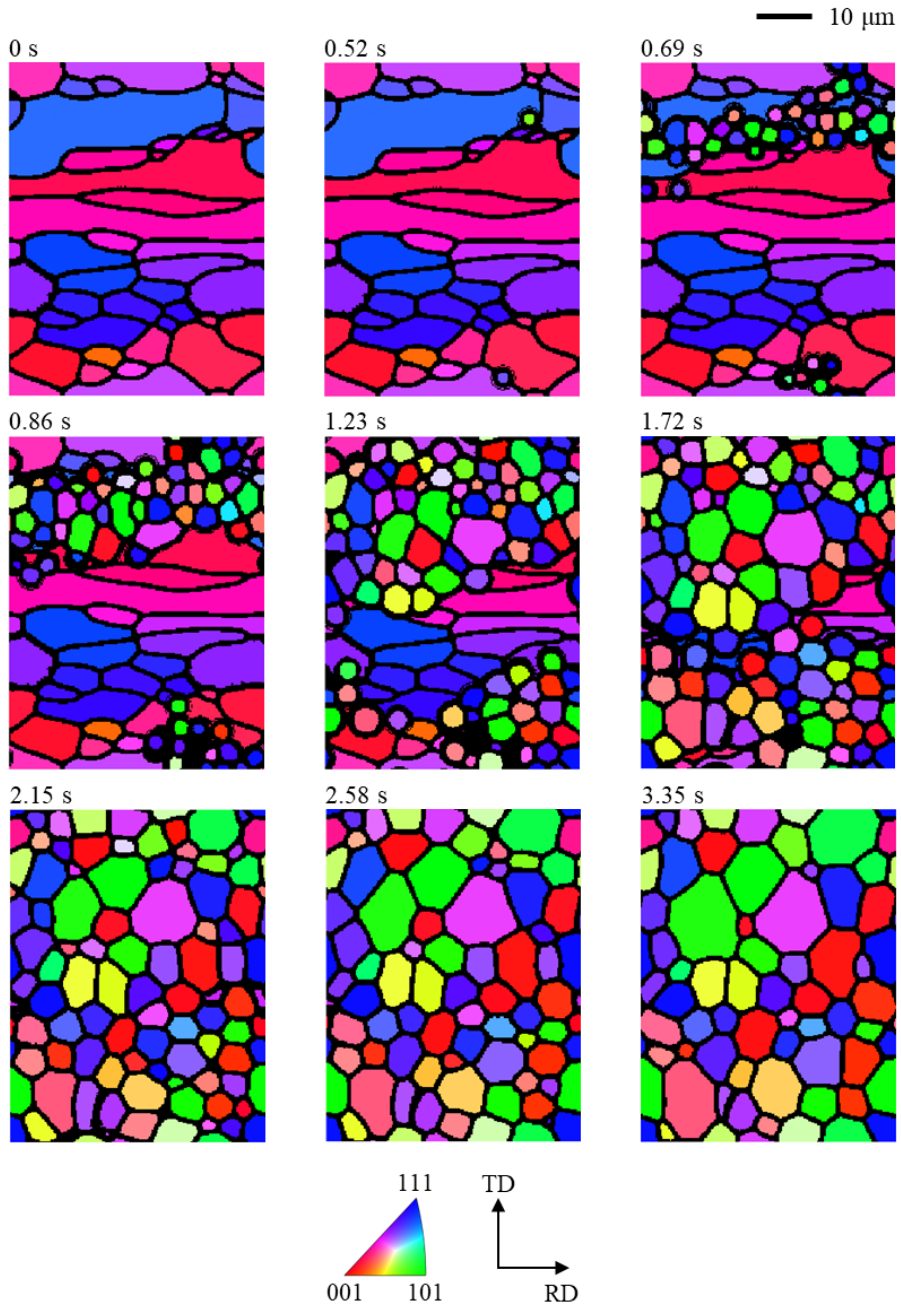


Fig. 4-15. Microstructure evolution in the shear band-dominant region during static recrystallization of GO electrical steel, as predicted using the integrated CP-PF model. The colors indicate the normal direction inverse pole figure map.

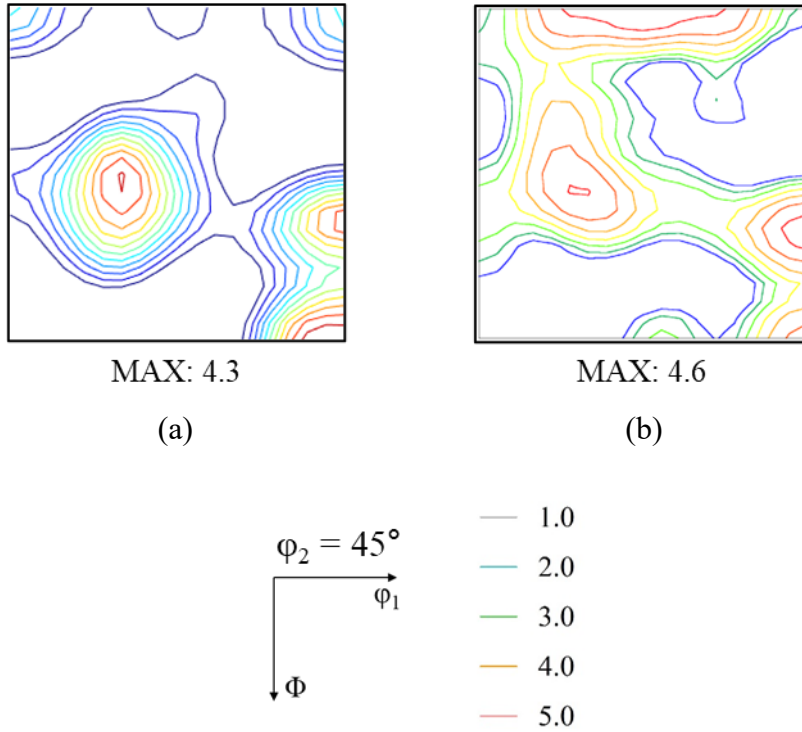


Fig. 4-16. (a) Predicted and (b) measured recrystallization texture of GO electrical steel, represented by the $\phi_2=45^\circ$ orientation distribution function section.

4.4. Summary

In this chapter, the origin of Goss grains during the primary recrystallization of 3.24 wt% Si GO electrical steel was investigated experimentally and numerically. The test specimen was subjected to 76% cold rolling, followed by heat treatment at 600 °C for 60 s to reproduce nucleation at the early stage of recrystallization. The resulting microstructures were characterized using EBSD, XRD, and TEM. To complement the experimental findings, the experimental process was simulated numerically. The cold-rolling process was simulated using the CPFEM, while the static recrystallization process was predicted using the PFM model. The predictive accuracy of the developed model was validated by comparing its texture components with experimentally measured ones. The major findings of this chapter can be summarized as follows:

- (1) Shear band formation was successfully simulated using the CPFEM in the severely deformed microstructures of cold-rolled GO electrical steels.
- (2) The activation and evolution of shear bands occurred in the γ -fibers centered on the $\{111\}\langle 112\rangle$ component. The origin of shear band formation could be theoretically confirmed using the dual-scale RVE approach coupled with the developed CP model.

- (3) Because of their high stored energy content, shear bands can be preferred nucleation sites at the early stage of primary recrystallization. This preference could be validated through CP simulations in which the higher activities of dislocation activities were present in the shear band-dominant regions.
- (4) Goss grains were nucleated in shear bands at the beginning of primary recrystallization. The developed integrated CP-PF model could reproduce the nucleation of Goss, $\langle 100 \rangle // \text{RD}$ component, and γ -fiber centered on the $\{111\} \langle 110 \rangle$ component, which determine the main characteristics of electrical steel, in shear band-dominant regions.
- (5) The recrystallization texture predicted through PF simulation aligned well with experimental observations, enhancing the fidelity of the developed integrated CP-PF model.

5. Conclusion

In this study, a multiscale numerical simulation approach was developed to facilitate a comprehensive exploration of the relationship between thermo-mechanical processing, microstructure evolution, and mechanical properties. This was accomplished through the numerical integration of CPFEM and PFM. The proposed integrated CP-PF model was validated through its application to two types of steels: ultra-low carbon steel and GO electrical steel. The primary achievements of this study can be encapsulated in the following points:

- The CPFEM, serving as a mechanical simulation module, provided microstructural heterogeneities at the grain-scale, including crystallographic orientations (rolling texture), inhomogeneous dislocation distributions, and shear band evolutions through polycrystalline grains by satisfying both equilibrium and compatibility within the context of the FE approach.
- The PFM, operating as a microstructure prediction module, provided the temporal evolution of the microstructure resulting from recovery, recrystallization, and grain growth. The key parameters used in the PFM simulation were transferred from the local effects obtained in the CPFEM module.

- A mapping technology, based on the Wigner-Seitz cell approach, was numerically implemented using Matlab™ software after introducing a special regularization technique to rectify the discrepancy between the coarser FE mesh and the finer finite difference grid used by the PFM. The validity of proposed mapping methodology was corroborated by the accurately transferred crystallographic orientations and stored elastic energy (or dislocation density).
- In the modeling of nucleation and growth for recrystallized grains during PFM simulation, new implementations were included: a reduction of stored energy due to the recovery process and a physics-based nucleation criterion considering the stored energy-dependent critical nucleus radius and its competition with the growing subgrain, as a function of misorientation and stored energy difference among neighboring grains.
- A significant advancement was made in accurately predicting the crystallographic orientations of newly nucleated grains during recrystallization (termed nucleation orientation probability), which can define the recrystallization texture when incorporated into the PFM. To achieve this, an extension of the SERM theory was deeply investigated to account for general deformation conditions involving multi-slip activities during mechanical loading, hence termed the

generalized SERM (GSERM) model. The concept of effective slip direction (ESD) was employed to correlate with the absolute maximum stress direction (AMSD) induced by dislocation stress fields. Given the inherent complexity of multiple ESDs resulting from the pencil glide of BCC metals, a novel variant selection rule for ESD was proposed, taking into account the empirically recognized in-grain shear band direction and highly mobile $\{110\}$ plane. However, in instances where shear bands were activated, it was found that the nucleation orientation probability could be predicted without the need for applying the variant selection rule. The effectiveness of this approach was confirmed by comparing the predicted recrystallization texture with experimental observations. The updated algorithms for recrystallized grains in PFM simulation were detailed in this study.

- Sheet anisotropy and formability of thermo-mechanically processed ultra-low carbon steel were evaluated through the virtual mechanical tests. Additionally, the nucleation of Goss grains within the shear bands were numerically reproduced during the early stage of static recrystallization in grain-oriented electrical steel. All predictions were compared with experimental findings for validation purposes, demonstrating the precision and robustness of the proposed

integrated CP-PF model.

- The activation and evolution of shear bands were found to occur in the γ -fibers centered on the $\{111\}\langle 112\rangle$ component. Due to their high stored energy content, these shear bands could serve as preferred nucleation sites during the early stages of primary recrystallization. The nucleation of Goss grains within the shear bands during this recrystallization was successfully reproduced using the proposed integrated CP-PF model, aligning well with the experimental observations.

Reference

- [1] K. Czelej, K.J. Kurzydłowski, Ab initio prediction of strong interfacial bonding in the Fe|Al bimetallic composite system, *Scr Mater.* 177 (2020) 162–165.
- [2] W.-S. Ko, W.S. Choi, G. Xu, P.-P. Choi, Y. Ikeda, B. Grabowski, Dissecting functional degradation in NiTi shape memory alloys containing amorphous regions via atomistic simulations, *Acta Mater.* 202 (2021) 331–349.
- [3] M. Jiang, G. Monnet, B. Devincre, On the origin of the Hall–Petch law: A 3D-dislocation dynamics simulation investigation, *Acta Mater.* 209 (2021) 116783.
- [4] K.M. Min, W. Jeong, S.H. Hong, C.A. Lee, P.-R. Cha, H.N. Han, M.-G. Lee, Integrated crystal plasticity and phase field model for prediction of recrystallization texture and anisotropic mechanical properties of cold-rolled ultra-low carbon steels, *Int J Plast.* 127 (2020) 102644.
- [5] H. Li, C.A. Duarte, A two-scale generalized finite element method for parallel simulations of spot welds in large structures, *Comput Methods Appl Mech Eng.* 337 (2018) 28–65.
- [6] J.-H. Kang, J. Kim, J.-Y. Kang, S.-W. Kwon, M.-W. Kang, S.H. Hong, Multiscale study on the dark-etching region due to rolling contact fatigue of 0.57C-bearing steel, *Acta Mater.* 226 (2022) 117666.

- [7] D. Zhang, Y. Zhu, L. Liu, X. Ying, C.-E. Hsiung, R. Sougrat, K. Li, Y. Han, Atomic-resolution transmission electron microscopy of electron beam-sensitive crystalline materials, *Science* (1979). 359 (2018) 675–679.
- [8] F.J. Humphreys, M. Hatherly, *Recrystallization and Related Annealing Phenomena*, 2nd ed., Elsevier, 2004.
- [9] H.J. Bong, F. Barlat, D.C. Ahn, H.-Y. Kim, M.-G. Lee, Formability of austenitic and ferritic stainless steels at warm forming temperature, *Int J Mech Sci.* 75 (2013) 94–109.
- [10] J.-Y. Lee, F. Barlat, M.-G. Lee, Constitutive and friction modeling for accurate springback analysis of advanced high strength steel sheets, *Int J Plast.* 71 (2015) 113–135.
- [11] N.-T. Nguyen, O. Seo, C. Lee, M.-G. Lee, J. Kim, H. Kim, Mechanical Behavior of AZ31B Mg Alloy Sheets under Monotonic and Cyclic Loadings at Room and Moderately Elevated Temperatures, *Materials.* 7 (2014) 1271–1295.
- [12] J. Park, M. Rout, K.M. Min, S.F. Chen, M.G. Lee, A fully coupled crystal plasticity-cellular automata model for predicting thermomechanical response with dynamic recrystallization in AISI 304LN stainless steel, *Mechanics of Materials.* 167 (2022).
- [13] K. Huang, R.E. Logé, A review of dynamic recrystallization phenomena in metallic materials, *Mater Des.* 111 (2016).
- [14] D.N. Lee, *Texture and related phenomena*, 2nd edition, The Korean Institute of Metals and Materials, Seoul, 2014.
- [15] G.I. Taylor, Plastic strain in metals, *J. Inst. Metals.* 62 (1938) 307–324.

- [16] M. Crumbach, M. Goerdeler, G. Gottstein, L. Neumann, H. Aretz, R. Kopp, Through-process texture modelling of aluminium alloys, *Model Simul Mat Sci Eng.* 12 (2004) S1–S18.
- [17] A. Molinari, G.R. Canova, S. Ahzi, A self consistent approach of the large deformation polycrystal viscoplasticity, *Acta Metallurgica.* 35 (1987) 2983–2994.
- [18] R.A. Lebensohn, C.N. Tomé, A self-consistent anisotropic approach for the simulation of plastic deformation and texture development of polycrystals: Application to zirconium alloys, *Acta Metallurgica et Materialia.* 41 (1993) 2611–2624.
- [19] D. Peirce, R.J. Asaro, A. Needleman, An analysis of nonuniform and localized deformation in ductile single crystals, *Acta Metallurgica.* 30 (1982) 1087–1119.
- [20] R.J. Asaro, *Micromechanics of Crystals and Polycrystals*, in: 1983: pp. 1–115.
- [21] S.R. Kalidindi, C.A. Bronkhorst, L. Anand, Crystallographic texture evolution in bulk deformation processing of FCC metals, *J Mech Phys Solids.* 40 (1992) 537–569.
- [22] P.R. Dawson, Computational crystal plasticity, *Int J Solids Struct.* 37 (2000) 115–130.
- [23] D. Raabe, P. Klose, B. Engl, K.-P. Imlau, F. Friedel, F. Roters, Concepts for Integrating Plastic Anisotropy into Metal Forming Simulations, *Adv Eng Mater.* 4 (2002) 169–180.

- [24] A. Ma, F. Roters, A constitutive model for fcc single crystals based on dislocation densities and its application to uniaxial compression of aluminium single crystals, *Acta Mater.* 52 (2004) 3603–3612.
- [25] J. Xiao, H. Cui, H. Zhang, W. Wen, J. Zhou, A physical-based constitutive model considering the motion of dislocation for Ni3Al-base superalloy, *Materials Science and Engineering A.* 772 (2020).
- [26] A. Arsenlis, D.M. Parks, Modeling the evolution of crystallographic dislocation density in crystal plasticity, 2002.
- [27] A. Patra, D.L. McDowell, Crystal plasticity-based constitutive modelling of irradiated bcc structures, *Philosophical Magazine.* 92 (2012) 861–887.
- [28] H. Li, C. Wu, H. Yang, Crystal plasticity modeling of the dynamic recrystallization of two-phase titanium alloys during isothermal processing, *Int J Plast.* 51 (2013) 271–291.
- [29] A. Alankar, I.N. Mastorakos, D.P. Field, A dislocation-density-based 3D crystal plasticity model for pure aluminum, *Acta Mater.* 57 (2009) 5936–5946.
- [30] J.T. Park, J.A. Szpunar, Evolution of recrystallization texture in nonoriented electrical steels, *Acta Mater.* 51 (2003) 3037–3051.
- [31] D. Raabe, R.C. Becker, Coupling of a crystal plasticity finite-element model with a probabilistic cellular automaton for simulating primary static recrystallization in aluminium, *Model Simul Mat Sci Eng.* 8 (2000) 445–462.

- [32] B. Radhakrishnan, G. Sarma, H. Weiland, P. Baggethun, Simulations of deformation and recrystallization of single crystals of aluminium containing hard particles, *Model Simul Mat Sci Eng.* 8 (2000) 737–750.
- [33] B. Radhakrishnan, G. Sarma, The effect of coarse non-deformable particles on the deformation and static recrystallization of aluminium alloys, *Philosophical Magazine.* 84 (2004) 2341–2366.
- [34] T. Takaki, Y. Tomita, Static recrystallization simulations starting from predicted deformation microstructure by coupling multi-phase-field method and finite element method based on crystal plasticity, *Int J Mech Sci.* 52 (2010) 320–328.
- [35] Y.-G. Cho, J.-Y. Kim, H.-H. Cho, P.-R. Cha, D.-W. Suh, J.K. Lee, H.N. Han, Analysis of Transformation Plasticity in Steel Using a Finite Element Method Coupled with a Phase Field Model, *PLoS One.* 7 (2012) e35987.
- [36] A. Vondrous, P. Bienger, S. Schreijäg, M. Selzer, D. Schneider, B. Nestler, D. Helm, R. Mönig, Combined crystal plasticity and phase-field method for recrystallization in a process chain of sheet metal production, *Comput Mech.* 55 (2015) 439–452.
- [37] D.K. Kim, W. Woo, W.W. Park, Y.T. Im, A. Rollett, Mesoscopic coupled modeling of texture formation during recrystallization considering stored energy decomposition, *Comput Mater Sci.* 129 (2017) 55–65.

- [38] M. Zecevic, R.A. Lebensohn, R.J. McCabe, M. Knezevic, Modelling recrystallization textures driven by intragranular fluctuations implemented in the viscoplastic self-consistent formulation, *Acta Mater.* 164 (2019) 530–546.
- [39] B.S. Fromm, K. Chang, D.L. McDowell, L.-Q. Chen, H. Garmestani, Linking phase-field and finite-element modeling for process–structure–property relations of a Ni-base superalloy, *Acta Mater.* 60 (2012) 5984–5999.
- [40] C. Liu, P. Shanthraj, M. Diehl, F. Roters, S. Dong, J. Dong, W. Ding, D. Raabe, An integrated crystal plasticity–phase field model for spatially resolved twin nucleation, propagation, and growth in hexagonal materials, *Int J Plast.* 106 (2018) 203–227.
- [41] V.I. Levitas, Phase field approach for stress- and temperature-induced phase transformations that satisfies lattice instability conditions. Part I. General theory, *Int J Plast.* 106 (2018) 164–185.
- [42] H. Babaei, V.I. Levitas, Phase-field approach for stress- and temperature-induced phase transformations that satisfies lattice instability conditions. Part 2. simulations of phase transformations Si I↔Si II, *Int J Plast.* 107 (2018) 223–245.
- [43] G. Gottstein, R. Sebal, Modelling of recrystallization textures, *J Mater Process Technol.* 117 (2001) 282–287.
- [44] D. Raabe, Introduction of a scalable three-dimensional cellular automaton with a probabilistic switching rule for the discrete mesoscale simulation of recrystallization phenomena, *Philosophical Magazine A.* 79 (1999) 2339–2358.

- [45] D. Raabe, L. Hantcherli, 2D cellular automaton simulation of the recrystallization texture of an IF sheet steel under consideration of Zener pinning, *Comput Mater Sci.* 34 (2005) 299–313.
- [46] R. Sebal, G. Gottstein, Modeling of recrystallization textures:: interaction of nucleation and growth, *Acta Mater.* 50 (2002) 1587–1598.
- [47] D. Raabe, A texture-component Avrami model for predicting recrystallization textures, kinetics and grain size, *Model Simul Mat Sci Eng.* 15 (2007) 39–63.
- [48] M.A. Miodownik, A review of microstructural computer models used to simulate grain growth and recrystallisation in aluminium alloys, *Journal of Light Metals.* 2 (2002) 125–135.
- [49] D. Raabe, Multiscale recrystallization models for the prediction of crystallographic textures with respect to process simulation, *J Strain Anal Eng Des.* 42 (2007) 253–268.
- [50] D.N. Lee, The evolution of recrystallization textures from deformation textures, *Scripta Metallurgica et Materialia.* 32 (1995) 1689–1694.
- [51] D.N. Lee, Strain energy release maximization model for evolution of recrystallization textures, *Int J Mech Sci.* 42 (2000) 1645–1678.
- [52] S.-H. Hong, D.N. Lee, Recrystallization Textures in Cold-Rolled Ti Bearing IF Steel Sheets., *ISIJ International.* 42 (2002) 1278–1287.
- [53] D.N. Lee, H.N. Han, H.S. Choi, Deformation and Recrystallization Textures of Surface Layers of Aluminum and Copper Sheets Cold-Rolled under Unlubricated Condition, *Key Eng Mater.* 535–536 (2013) 211–214.

- [54] K.H. Oh, Y.M. Koo, D.N. Lee, Evolution of Textures and Microstructures in Low-Reduction Rolled and Annealed Low-Carbon Steels, *Materials Science Forum*. 715–716 (2012) 173–178.
- [55] J.K. Kim, D.N. Lee, Y.M. Koo, The evolution of the Goss and Cube textures in electrical steel, *Mater Lett*. 122 (2014) 110–113.
- [56] H.H. Lee, J. Jung, J.I. Yoon, J.-K. Kim, H.S. Kim, Modelling the evolution of recrystallization texture for a non-grain oriented electrical steel, *Comput Mater Sci*. 149 (2018) 57–64.
- [57] K.H. Oh, J.S. Jeong, Y.M. Koo, D.N. Lee, The evolution of the rolling and recrystallization textures in cold-rolled Al containing high Mn austenitic steels, *Mater Chem Phys*. 161 (2015) 9–18.
- [58] Z. Marciniak, K. Kuczyński, Limit strains in the processes of stretch-forming sheet metal, *Int J Mech Sci*. 9 (1967) 609–620.
- [59] H.J. Bong, J. Lee, X. Hu, X. Sun, M.G. Lee, Predicting forming limit diagrams for magnesium alloys using crystal plasticity finite elements, *Int J Plast*. 126 (2020).
- [60] C.P. Kohar, J.L. Bassani, A. Brahme, W. Muhammad, R.K. Mishra, K. Inal, A new multi-scale framework to incorporate microstructure evolution in phenomenological plasticity: Theory, explicit finite element formulation, implementation and validation, *Int J Plast*. 117 (2019) 122–156.
- [61] I. Steinbach, F. Pezzolla, A generalized field method for multiphase transformations using interface fields, *Physica D*. 134 (1999) 385–393.

- [62] S.G. Kim, D.I. Kim, W.T. Kim, Y.B. Park, Computer simulations of two-dimensional and three-dimensional ideal grain growth, *Phys Rev E*. 74 (2006) 061605.
- [63] H. Zurob, Y. Brechet, J. Dunlop, Quantitative criterion for recrystallization nucleation in single-phase alloys: Prediction of critical strains and incubation times, *Acta Mater.* 54 (2006) 3983–3990.
- [64] S.R. Kalidindi, Modeling anisotropic strain hardening and deformation textures in low stacking fault energy fcc metals, *Int J Plast.* 17 (2001) 837–860.
- [65] N. Jia, F. Roters, P. Eisenlohr, C. Kords, D. Raabe, Non-crystallographic shear banding in crystal plasticity FEM simulations: Example of texture evolution in α -brass, *Acta Mater.* 60 (2012) 1099–1115.
- [66] M. Ardeljan, I.J. Beyerlein, M. Knezevic, A dislocation density based crystal plasticity finite element model: Application to a two-phase polycrystalline HCP/BCC composites, *J Mech Phys Solids.* 66 (2014) 16–31.
- [67] D. Hull, D.J. Bacon, *Introduction to Dislocations*, 5th edition, Elsevier, Amsterdam, 2011.
- [68] L. Anand, C. Su, A theory for amorphous viscoplastic materials undergoing finite deformations, with application to metallic glasses, *J Mech Phys Solids.* 53 (2005) 1362–1396.
- [69] Y. Wei, C. Su, L. Anand, A computational study of the mechanical behavior of nanocrystalline fcc metals, *Acta Mater.* 54 (2006) 3177–3190.

- [70] M.A. Groeber, M.A. Jackson, DREAM.3D: A Digital Representation Environment for the Analysis of Microstructure in 3D, *Integr Mater Manuf Innov.* 3 (2014) 56–72.
- [71] S.G. Kim, Y.B. Park, Grain boundary segregation, solute drag and abnormal grain growth, *Acta Mater.* 56 (2008) 3739–3753.
- [72] T. Takaki, Y. Hisakuni, T. Hirouchi, A. Yamanaka, Y. Tomita, Multi-phase-field simulations for dynamic recrystallization, *Comput Mater Sci.* 45 (2009) 881–888.
- [73] T. Takaki, A. Yamanaka, Y. Tomita, Multi-phase-field Simulations of Dynamic Recrystallization during Transient Deformation, *ISIJ International.* 51 (2011) 1717–1723.
- [74] T. Takaki, C. Yoshimoto, A. Yamanaka, Y. Tomita, Multiscale modeling of hot-working with dynamic recrystallization by coupling microstructure evolution and macroscopic mechanical behavior, *Int J Plast.* 52 (2014) 105–116.
- [75] H.J. Frost, M.F. Ashby, *Deformation-Mechanism Maps: The Plasticity and Creep of Metals and Ceramics*, 1st edition, Pergamon Press, Oxford, 1982.
- [76] W.T. Read, W. Shockley, Dislocation Models of Crystal Grain Boundaries, *Physical Review.* 78 (1950) 275–289.
- [77] F.J. Humphreys, A unified theory of recovery, recrystallization and grain growth, based on the stability and growth of cellular microstructures—I. The basic model, *Acta Mater.* 45 (1997) 4231–4240.

- [78] O. Güvenç, T. Henke, G. Laschet, B. Böttger, M. Apel, M. Bambach, G. Hirt, Modeling of static recrystallization kinetics by coupling crystal plasticity FEM and multiphase field calculations, *Comput Methods Mater Sci.* 13 (2013) 368–374.
- [79] T. Takaki, A. Yamanaka, Y. Higa, Y. Tomita, Phase-field model during static recrystallization based on crystal-plasticity theory, *Journal of Computer-Aided Materials Design.* 14 (2007) 75–84.
- [80] J.E. Bailey, P.B. Hirsch, The recrystallization process in some polycrystalline metals, *Proc R Soc Lond A Math Phys Sci.* 267 (1962) 11–30.
- [81] D. Kuhlmann, Zur Theorie der Nachwirkungerscheinungen, *Zeitschrift Für Physik.* 124 (1948) 468–481.
- [82] A.H. Cottrell, V. Aytakin, The flow of zinc under constant stress, *J. Inst. Metals.* 77 (1950) 389.
- [83] J. Friedel, *Dislocations*, 1st edition, Elsevier, Amsterdam, 1964.
- [84] X. Song, M. Rettenmayr, Modelling study on recrystallization, recovery and their temperature dependence in inhomogeneously deformed materials, *Materials Science and Engineering: A.* 332 (2002) 153–160.
- [85] R. Sandström, Subgrain growth occurring by boundary migration, *Acta Metallurgica.* 25 (1977) 905–911.
- [86] S.K. Varma, Effects of the amount of prior cold work and annealing temperature on subgrain growth in Al 0.2Mg alloy, *Materials Science and Engineering.* 82 (1986) L19–L22.

- [87] D.N. Lee, H.N. Han, Orientation Relationships between Precipitates and Their Parent Phases in Steels at Low Transformation Temperatures, *Journal of Solid Mechanics and Materials Engineering*. 6 (2012) 323–338.
- [88] D.N. Lee, H.N. Han, Recrystallization Textures of Metals and Alloys, in: *Recent Developments in the Study of Recrystallization*, InTech, 2013.
- [89] W.T. Read, *Dislocation in crystals*, McGraw-Hill, New York, 1953.
- [90] Y.B. Park, D.N. Lee, G. Gottstein, The evolution of recrystallization textures in body centred cubic metals, *Acta Mater*. 46 (1998) 3371–3379.
- [91] Y.B. Park, L. Kestens, J.J. Jonas, Effect of Internal Stresses in Cold Rolled IF Steel on the Orientations of Recrystallized Grains., *ISIJ International*. 40 (2000) 393–401.
- [92] S. Takaki, T. Masumura, T. Tsuchiyama, Dislocation Characterization by the Direct-fitting/modified Williamson–Hall (DF/mWH) Method in Cold Worked Ferritic Steel, *ISIJ International*. 59 (2019) 567–572.
- [93] Y. Oh, W.-S. Ko, N. Kwak, J. Jang, T. Ohmura, H.N. Han, Small-scale analysis of brittle-to-ductile transition behavior in pure tungsten, *J Mater Sci Technol*. 105 (2022) 242–258.
- [94] A.P. Sutton, R.W. Balluffi, *Interfaces in Crystalline Materials*, Oxford University Press, Oxford, 1995.
- [95] M.R. Barnett, J.J. Jonas, Influence of Ferrite Rolling Temperature on Microstructure and Texture in Deformed Low C and IF Steels., *ISIJ International*. 37 (1997) 697–705.

- [96] T. Urabe, J.J. Jonas, Modeling Texture Change during the Recrystallization of an IF Steel., *ISIJ International*. 34 (1994) 435–442.
- [97] T. Watanabe, Observations of plane-matching grain boundaries by electron channelling patterns, *Philosophical Magazine A*. 47 (1983) 141–146.
- [98] M.E. McHenry, D.E. Laughlin, Magnetic Properties of Metals and Alloys, in: *Physical Metallurgy*, Elsevier, 2014: pp. 1881–2008.
- [99] T. Urabe, High Formability Steel, in: *Encyclopedia of Materials: Metals and Alloys*, Elsevier, 2022: pp. 3–11.
- [100] S.K. Paul, S. Mishra, On the formability of sheet steels, *Bulletin of Materials Science*. 19 (1996) 963–984.
- [101] K.S. Chan, Effects of plastic anisotropy and yield surface shape on sheet metal stretchability, *Metallurgical Transactions A*. 16 (1985) 629–639.
- [102] F. Bachmann, R. Hielscher, H. Schaeben, Texture Analysis with MTEX – Free and Open Source Software Toolbox, *Solid State Phenomena*. 160 (2010) 63–68.
- [103] D. Raabe, Y. Wang, F. Roters, Crystal plasticity simulation study on the influence of texture on earing in steel, *Comput Mater Sci*. 34 (2005) 221–234.
- [104] S. Takaki, Review on the Hall-Petch relation in ferritic steel, in: *Materials Science Forum*, Trans Tech Publications Ltd, 2010: pp. 11–16.

- [105] W. Ye, R. Le Gall, G. Saindrenan, A study of the recrystallization of an IF steel by kinetics models, *Materials Science and Engineering: A*. 332 (2002) 41–46.
- [106] S. Ratanaphan, D.L. Olmsted, V. V. Bulatov, E.A. Holm, A.D. Rollett, G.S. Rohrer, Grain boundary energies in body-centered cubic metals, *Acta Mater.* 88 (2015) 346–354.
- [107] A. Martínez-de-Guerenu, F. Arizti, I. Gutiérrez, Recovery during annealing in a cold rolled low carbon steel. Part II: Modelling the kinetics, *Acta Mater.* 52 (2004) 3665–3670.
- [108] P.-R. Cha, J.-Y. Kim, W.-T. Kim, S.G. Kim, Phase Field Study on the Austenite/Ferrite Transition in Low Carbon Steel, *Materials and Manufacturing Processes*. 25 (2010) 106–110.
- [109] G. Abrivard, E.P. Busso, S. Forest, B. Appolaire, Phase field modelling of grain boundary motion driven by curvature and stored energy gradients. Part II: Application to recrystallisation, *Philosophical Magazine*. 92 (2012) 3643–3664.
- [110] H. Rodney, A theory of the yielding and plastic flow of anisotropic metals, *Proc R Soc Lond A Math Phys Sci*. 193 (1948) 281–297.
- [111] F. Barlat, J.C. Brem, J.W. Yoon, K. Chung, R.E. Dick, D.J. Lege, F. Pourboghrat, S.-H. Choi, E. Chu, Plane stress yield function for aluminum alloy sheets—part 1: theory, *Int J Plast.* 19 (2003) 1297–1319.
- [112] Metallic materials-Sheet and strip-Determination of forming-limit curves-Part 2: Determination of forming-limit curves in the laboratory, International Organization for Standardization, 2008.

- [113] K. Günther, G. Abbruzzese, S. Fortunati, G. Ligi, Recent technology developments in the production of grain-oriented electrical steel, *Steel Res Int.* 76 (2005) 413–421.
- [114] X. Shen, F. Meng, K.B. Lau, P. Wang, C.H.T. Lee, Texture and microstructure characterizations of Fe-3.5wt%Si soft magnetic alloy fabricated via laser powder bed fusion, *Mater Charact.* 189 (2022) 112012.
- [115] Y.-K. Jeong, Y.-K. Ahn, S.-B. Kwon, T.-Y. Kim, H.-K. Kim, I.-S. Kim, C.-H. Han, N.-M. Hwang, Variables Affecting the Evolution of the $\{100\}$ Texture Induced by Surface Nucleation During $\gamma \rightarrow \alpha$ Phase Transformation in Fe–Si Electrical Steel, *Metals and Materials International.* (2022).
- [116] Z. Xia, Y. Kang, Q. Wang, Developments in the production of grain-oriented electrical steel, *J Magn Magn Mater.* 320 (2008) 3229–3233.
- [117] H.H. Lee, J. Jung, J.I. Yoon, J.K. Kim, H.S. Kim, Modelling the evolution of recrystallization texture for a non-grain oriented electrical steel, *Comput Mater Sci.* 149 (2018) 57–64.
- [118] T.-Y. Kim, T.-W. Na, H.-S. Shim, K. Gil, N.-M. Hwang, Effect of the magnitude of sub-boundary angles on the abnormal grain growth rate of Goss grains in Fe-3%Si steel, *Mater Charact.* 184 (2022) 111655.
- [119] I. Samajdar, S. Cicale, B. Verlinden, P. Van Houtte, G. Abbruzzese, Primary recrystallization in a grain oriented silicon steel: on the origin of goss $\{110\}$ grains, *Scr Mater.* 39 (1998) 1083–1088.

- [120] T.-Y. Kim, T.-W. Na, H.-S. Shim, Y.-K. Ahn, Y.-K. Jeong, H.N. Han, N.-M. Hwang, Misorientation Characteristics at the Growth Front of Abnormally-Growing Goss Grains in Fe-3%Si Steel, *Metals and Materials International*. 27 (2021) 5114–5120.
- [121] T. Haratani, W.B. Hutchinson, I.L. Dillamore, P. Bate, Contribution of shear banding to origin of Goss texture in silicon iron, *Metal Science*. 18 (1984) 57–66.
- [122] K. Ushioda, W.B. Hutchinson, Role of shear bands in annealing texture formation in 3%Si-Fe(111)[112] single crystals., *ISIJ International*. 29 (1989) 862–867.
- [123] Y. Wang, Y.B. Xu, Y.X. Zhang, F. Fang, X. Lu, H.T. Liu, G.D. Wang, Development of microstructure and texture in strip casting grain oriented silicon steel, *J Magn Magn Mater*. 379 (2015) 161–166.
- [124] F. Fang, X. Lu, Y.X. Zhang, Y. Wang, H.T. Jiao, G.M. Cao, G. Yuan, Y.B. Xu, R.D.K. Misra, G.D. Wang, Influence of cold rolling direction on texture, inhibitor and magnetic properties in strip-cast grain-oriented 3% silicon steel, *J Magn Magn Mater*. 424 (2017) 339–346.
- [125] H. Xu, Y. Xu, Y. He, H. Jiao, S. Yue, J. Li, A quasi in-situ EBSD study of the nucleation and growth of Goss grains during primary and secondary recrystallization of a strip-cast Fe-6.5 wt% Si alloy, *J Alloys Compd*. 861 (2021).
- [126] S. Chen, J. Butler, S. Melzer, Effect of asymmetric hot rolling on texture, microstructure and magnetic properties in a non-grain oriented electrical steel, *J Magn Magn Mater*. 368 (2014) 342–352.

- [127] M. Mehdi, Y. He, E.J. Hilinski, A. Edrisy, Texture Evolution of a 2.8 Wt Pct Si Non-oriented Electrical Steel and the Elimination of the $\langle 111 \rangle$ /ND Texture, *Metallurgical and Materials Transactions A*. 50 (2019) 3343–3357.
- [128] M. Mehdi, Y. He, E.J. Hilinski, L.A.I. Kestens, A. Edrisy, The evolution of cube ($\{001\}\langle 100 \rangle$) texture in non-oriented electrical steel, *Acta Mater*. 185 (2020) 540–554.
- [129] K. Pawlik, J. Pospiech, K. Lücke, The ODF Approximation From Pole Figures With the Aid of the ADC Method, *Textures and Microstructures*. 14 (1991) 25–30.
- [130] M. Hölscher, D. Raabe, K. Lücke, Rolling and recrystallization textures of bcc steels, *Steel Research*. 62 (1991) 567–575.
- [131] T. Nguyen-Minh, J.J. Sidor, R.H. Petrov, L.A.I. Kestens, Shear banding and its contribution to texture evolution in rotated Goss orientations of BCC structured materials, in: *IOP Conf Ser Mater Sci Eng*, Institute of Physics Publishing, 2015.
- [132] Q.Z. Chen, M.Z. Quadir, B.J. Duggan, Shear band formation in IF steel during cold rolling at medium reduction levels, *Philosophical Magazine*. 86 (2006) 3633–3646.
- [133] T. Ungár, A. Borbély, The effect of dislocation contrast on x-ray line broadening: A new approach to line profile analysis, *Appl Phys Lett*. 69 (1996) 3173–3175.
- [134] G.K. Williamson, R.E. Smallman, III. Dislocation densities in some annealed and cold-worked metals from measurements on the X-ray debye-scherrer spectrum, *Philosophical Magazine*. 1 (1956) 34–46.

[135] D.P. Field, Recent advances in the application of orientation imaging, *Ultramicroscopy*. 67 (1997) 1–9.

Appendix A. Time integration procedure and analytical Jacobian for crystal plasticity finite element model

For CPFEM, the fully implicit Euler-backward time integration schemes was implemented in the commercial software package Abaqus/Standard, following an “static, implicit” finite element procedure. This implicit finite element procedure uses Newton-Rhaphson iterative method to revise estimates of nodal displacements, necessitating the calculation of a Jacobian matrix that is consistent with the time integration procedure employed in the constitutive model. In the following, the computational methodology for the time integration procedure and the evaluation of analytical Jacobian matrix are described. [1,2]

A.1. Time integration procedure

$\mathbf{F}(t)$ and the list of variables $\{\mathbf{F}^p(t), \rho_{edge}^\alpha(t), \rho_{screw}^\alpha(t), \mathbf{S}(t)\}$ in each grain at time t were assumed to be given. $\mathbf{F}(\tau)$, an estimate of the deformation gradient at time $\tau = t + \Delta t$ was assumed to be given.

(i) Calculate

$$\mathbf{A} = \mathbf{F}^{p^{-T}}(t)\mathbf{F}^T(\tau)\mathbf{F}(\tau)\mathbf{F}^{p^{-1}}(t) \quad (\text{A.1})$$

$$\mathbf{S}^{e,tr} = \mathbf{C}^e \left[\frac{1}{2} \{ \mathbf{A} - \mathbf{I} \} \right]. \quad (\text{A.2})$$

Time independent slip quantities are as follows:

$$\mathbf{C}^\alpha = \mathbf{C}^e \left[\frac{1}{2} \left(\mathbf{A} \mathbf{s}_0^\alpha + \mathbf{s}_0^{\alpha T} \mathbf{A} \right) \right] \quad (\text{A.3})$$

where $\mathbf{s}_0^\alpha = \mathbf{m}_0^\alpha \otimes \mathbf{n}_0^\alpha$.

Time dependent shear band quantities are as follows:

$$\mathbf{C}^\chi \left(\mathbf{S}^e(\tau) \right) = \mathbf{C}^e \left[\frac{1}{2} \left(\mathbf{A} \mathbf{s}^\chi(\tau) + \mathbf{s}^{\chi T}(\tau) \mathbf{A} \right) \right] \quad (\text{A.4})$$

where $\mathbf{s}^\chi(\tau) = \mathbf{m}^\chi(\tau) \otimes \mathbf{n}^\chi(\tau)$. \mathbf{m}^χ and \mathbf{n}^χ can be derived by spectral decomposition of \mathbf{S}^e , obtained in the following.

(ii) Solve

$$\begin{aligned} \mathbf{S}^e(\tau) = & \mathbf{S}^{e,tr} - \sum_{\alpha} \Delta \gamma^\alpha \left(\tau^\alpha \left(\mathbf{S}^e(\tau) \right), \rho_{edge}^\alpha(\tau), \rho_{screw}^\alpha(\tau) \right) \mathbf{C}^\alpha \\ & - \sum_{\chi} \Delta \gamma^\chi \left(\tau^\chi \left(\mathbf{S}^e(\tau) \right) \right) \mathbf{C}^\chi \left(\mathbf{S}^e(\tau) \right) \end{aligned} \quad (\text{A.5})$$

$$\begin{aligned} \rho_{edge}^\alpha(\tau) = & \rho_{edge}^\alpha(t) + \left\{ \frac{\sqrt{\rho_F^\alpha(\tau)}}{c_4} \rho_{mobile,screw}^\alpha(\tau) v_{screw}^\alpha(\tau) \right. \\ & \left. - \frac{1}{2} \rho_{mobile,edge}^\alpha(\tau) \rho_{edge}^\alpha(\tau) R_{edge} v_{edge}^\alpha(\tau) \right\} \Delta t \end{aligned} \quad (\text{A.6})$$

$$\rho_{screw}^\alpha(\tau) = \rho_{screw}^\alpha(t) + \left\{ \frac{\sqrt{\rho_F^\alpha(\tau)}}{c_5} \rho_{mobile,edge}^\alpha(\tau) v_{edge}^\alpha(\tau) - \frac{1}{2} \rho_{mobile,screw}^\alpha(\tau) \rho_{screw}^\alpha(\tau) R_{screw} v_{screw}^\alpha(\tau) \right\} \Delta t \quad (\text{A.7})$$

with

$$v_{edge}^\alpha(\tau) = v_{edge}^\alpha\left(\tau^\alpha(\mathbf{S}^e(\tau)), \rho_{edge}^\alpha(\tau), \rho_{screw}^\alpha(\tau)\right) \quad (\text{A.8})$$

$$v_{screw}^\alpha(\tau) = v_{screw}^\alpha\left(\tau^\alpha(\mathbf{S}^e(\tau)), \rho_{edge}^\alpha(\tau), \rho_{screw}^\alpha(\tau)\right) \quad (\text{A.9})$$

for $\mathbf{S}^e(\tau)$, $\rho_{edge}^\alpha(\tau)$, and $\rho_{screw}^\alpha(\tau)$ using the following two-step iterative procedure.

In the first step, Eq. (A.5) was solved for $\mathbf{S}^e(\tau)$, keeping $\rho_{edge}^\alpha(\tau)$ and $\rho_{screw}^\alpha(\tau)$ fixed at their best available estimates using the following Newton-Raphson iterative method:

$$\mathbf{S}_{n+1}^e(\tau) = \mathbf{S}_n^e(\tau) - \mathbf{J}_n^{-1}[\mathbf{G}_n] \quad (\text{A.10})$$

where

$$\begin{aligned} \mathbf{G}_n &= \mathbf{S}_n^e(\tau) - \mathbf{S}^{e,tr} \\ &+ \sum_{\alpha} \Delta \gamma^\alpha \left(\tau^\alpha(\mathbf{S}_n^e(\tau)), \rho_{edge,k+1}^\alpha(\tau), \rho_{screw,k+1}^\alpha(\tau) \right) \mathbf{C}^\alpha \quad (\text{A.11}) \\ &+ \sum_{\chi} \Delta \gamma^\chi \left(\tau^\chi(\mathbf{S}_n^e(\tau)) \right) \mathbf{C}^\chi(\mathbf{S}_n^e(\tau)) \end{aligned}$$

$$\begin{aligned} \mathbf{J}_n = \mathbf{I} + \sum_{\alpha} \left\{ \frac{\partial}{\partial \tau^{\alpha}} \Delta \gamma^{\alpha} \left(\tau^{\alpha} \left(\mathbf{S}_n^e(\tau) \right), \rho_{edge,k+1}^{\alpha}(\tau), \rho_{screw,k+1}^{\alpha}(\tau) \right) \right\} \mathbf{C}^{\alpha} \otimes \mathbf{s}_0^{\alpha} \\ + \sum_{\chi} \left\{ \frac{\partial}{\partial \mathbf{S}_n^e(\tau)} \Delta \gamma^{\chi} \left(\tau^{\chi} \left(\mathbf{S}_n^e(\tau) \right) \right) \right\} \otimes \mathbf{C}^{\chi} \left(\mathbf{S}_n^e(\tau) \right) \end{aligned} \quad (\text{A.12})$$

where the subscripts n and $n+1$ refer to estimates of $\mathbf{S}^e(\tau)$ at the end of n and $n+1$ iterations, respectively, in the first step of the iterative scheme. Subscript k refers to the values of $\rho_{edge}^{\alpha}(\tau)$ and $\rho_{screw}^{\alpha}(\tau)$ at the end of the k^{th} update in the second step of iterations. In the first step of iterative procedure, following constraint was applied to handle the low-rate sensitivity of plastic flow:

If

$$\left| \Delta \gamma^{\alpha,\chi} \right|_{\max} < \Delta \gamma_{tol} \quad (\text{A.13})$$

then accept the Newton correction

else

$$(S_{ij}^e)_{n+1}(\tau) = (S_{ij}^e)_n(\tau) + \eta \Delta S_{ij}^e \quad (\text{A.14})$$

where η is a numerical constant. A value of 0.25 was found to give reasonable results in the calculations in this study.

After convergence of $\mathbf{S}^e(\tau)$, the second step iterative procedure involves a simple update of $\rho_{edge}^{\alpha}(\tau)$ and $\rho_{screw}^{\alpha}(\tau)$ as follows:

$$\rho_{edge,k+1}^\alpha = \rho_{edge}^\alpha(t) + \left\{ \frac{\sqrt{\rho_{F,k}^\alpha(\tau)}}{c_4} \rho_{mobile,screw,k}^\alpha(\tau) v_{screw,k}^\alpha(\tau) - \frac{1}{2} \rho_{mobile,edge,k}^\alpha(\tau) \rho_{edge,k}^\alpha(\tau) R_{edge} v_{edge,k}^\alpha(\tau) \right\} \Delta t \quad (\text{A.15})$$

$$\rho_{screw,k+1}^\alpha = \rho_{screw}^\alpha(t) + \left\{ \frac{\sqrt{\rho_{F,k}^\alpha(\tau)}}{c_5} \rho_{mobile,edge,k}^\alpha(\tau) v_{edge,k}^\alpha(\tau) - \frac{1}{2} \rho_{mobile,screw,k}^\alpha(\tau) \rho_{screw,k}^\alpha(\tau) R_{screw} v_{screw,k}^\alpha(\tau) \right\} \Delta t \quad (\text{A.16})$$

with

$$v_{edge,k}^\alpha(\tau) = v_{edge,k}^\alpha \left(\tau^\alpha \left(\mathbf{S}_{n+1}^e(\tau) \right), \rho_{edge,k}^\alpha(\tau), \rho_{screw,k}^\alpha(\tau) \right) \quad (\text{A.17})$$

$$v_{screw,k}^\alpha(\tau) = v_{screw,k}^\alpha \left(\tau^\alpha \left(\mathbf{S}_{n+1}^e(\tau) \right), \rho_{edge,k}^\alpha(\tau), \rho_{screw,k}^\alpha(\tau) \right) \quad (\text{A.18})$$

The initial guesses for $\mathbf{S}^e(\tau)$, $\rho_{edge}^\alpha(\tau)$, and $\rho_{screw}^\alpha(\tau)$ used to start the two-step iterative procedure were taken as $\mathbf{S}^e(t)$, $\rho_{edge}^\alpha(t)$, and $\rho_{screw}^\alpha(t)$. The convergence criterion of $\mathbf{S}^e(\tau)$ was based on the maximum of the absolute changes in the components, less than $10^{-4} \times \sigma_{tol}$,

with

$$\sigma_{tol} = \frac{1}{2} Gb \sqrt{\rho_{0,edge}^\alpha + \rho_{0,screw}^\alpha} \quad (\text{A.19})$$

For $\rho_{edge}^\alpha(\tau)$ and $\rho_{screw}^\alpha(\tau)$, the convergence criterion was given as

follows:

$$\sigma_{res,k}^{\alpha} = \frac{1}{2} Gb \sqrt{\left(\rho_{edge,k}^{\alpha}(\tau) + \rho_{screw,k}^{\alpha}(\tau) \right)} \quad (\text{A.20})$$

If

$$\left| \sigma_{res,k+1}^{\alpha} - \sigma_{res,k}^{\alpha} \right|_{\max} < 10^{-3} \times \sigma_{tol} \quad (\text{A.21})$$

then accept the values.

(iii) Calculate

$$\mathbf{F}^p(\tau) = \left\{ \mathbf{I} + \sum_{\alpha} \Delta\gamma^{\alpha} \mathbf{s}_0^{\alpha} + \sum_{\chi} \Delta\gamma^{\chi} \mathbf{s}^{\chi} \right\} \mathbf{F}^p(t) \quad (\text{A.22})$$

It is necessary to normalize $\mathbf{F}^p(\tau)$ by dividing the calculated values of each of its components by the cube root of the calculated determinant to ensure the plastic incompressibility, which means that $\det(\mathbf{F}^p(\tau))$ is unity.

(iv) Calculate

$$\begin{aligned} \mathbf{S}(\tau) &= \frac{1}{\det \mathbf{F}^e(\tau)} \mathbf{F}^e(\tau) \mathbf{S}^e(\tau) \mathbf{F}^{eT}(\tau) \\ &= \frac{1}{\det \mathbf{F}^e(\tau)} \mathbf{F}(\tau) \mathbf{F}^{p^{-1}}(\tau) \mathbf{S}^e(\tau) \mathbf{F}^{p^{-T}}(\tau) \mathbf{F}^T(\tau) \end{aligned} \quad (\text{A.23})$$

(v) Calculate

$$\mathbf{m}^{\alpha}(\tau) = \mathbf{F}^e(\tau) \mathbf{m}_0^{\alpha} = \mathbf{F}(\tau) \mathbf{F}^{p^{-1}}(\tau) \mathbf{m}_0^{\alpha} \quad (\text{A.24})$$

$$\mathbf{n}^\alpha(\tau) = \mathbf{F}^{e^{-T}}(\tau)\mathbf{n}_0^\alpha = \mathbf{F}^{-T}(\tau)\mathbf{F}^{p^T}(\tau)\mathbf{n}_0^\alpha \quad (\text{A.25})$$

The time-stepping for the implicit finite element procedure was automatically handled based on the maximum value of the slip and shear band increment. A parameter $R = \frac{\Delta\gamma_{\max}^{\alpha,\mathcal{Z}}}{\Delta\gamma_{\text{lim}}}$ was used as a measure for handling time-increments, where $\Delta\gamma_{\max}^{\alpha,\mathcal{Z}}$ is the maximum value of $\Delta\gamma^{\alpha,\mathcal{Z}}$ over all the crystals and all integration points in the finite element, and $\Delta\gamma_{\text{lim}}$ is a numerical constant. A value of 0.03 was found to give reasonable results in the calculations in this study. If the value of R is greater than 1, then the time-step is repeated with a new time increment with $\Delta t_{\text{new}} = 0.75\Delta t_{\text{old}}$. If $0.5 < R < 1$, then the value is maintained, and if $R < 0.5$, then the time-increment is increased; $\Delta t_{n+1} = 1.25\Delta t_n$.

A.2. Analytical Jacobian

The Jacobian matrix for Abaqus/Standard was obtained numerically by perturbing $\mathbf{F}(\tau) = \mathbf{F}_t(\tau)\mathbf{F}(t)$ with relative deformation gradient $\mathbf{F}_t(\tau)$ and using the methodology for the time integration procedure to calculate $\mathbf{S}(\tau)$.

The Jacobian matrix required for Abaqus/Standard can be defined as follows:

$$\mathbf{w} = \frac{\partial \mathbf{s}}{\partial \mathbf{e}} \quad (\text{A.26})$$

with

$$\mathbf{s} = \begin{pmatrix} S(\tau)_{11} \\ S(\tau)_{22} \\ S(\tau)_{33} \\ S(\tau)_{12} \\ S(\tau)_{13} \\ S(\tau)_{23} \end{pmatrix}, \quad \mathbf{e} = \begin{pmatrix} E_t(\tau)_{11} \\ E_t(\tau)_{22} \\ E_t(\tau)_{33} \\ 2E_t(\tau)_{12} \\ 2E_t(\tau)_{13} \\ 2E_t(\tau)_{23} \end{pmatrix} \quad (\text{A.27})$$

where $S(\tau)_{ij}$ and $E_t(\tau)_{ij}$ are the components of the symmetric Cauchy stress tensor $\mathbf{S}(\tau)$ and a symmetric relative strain tensor $\mathbf{E}_t(\tau)$, respectively. The relative strain increment is given as $\mathbf{E}_t(\tau) = \ln \mathbf{U}_t(\tau)$, where $\mathbf{U}_t(\tau)$ is the relative stretch tensor obtained from the polar decomposition of $\mathbf{F}_t(\tau)$. For relatively small incremental stretch,

$$\mathbf{E}_t(\tau) = \ln \mathbf{U}_t(\tau) \approx \mathbf{U}_t(\tau) - 1 \quad (\text{A.28})$$

then $d\mathbf{E}_t(\tau) \doteq d\mathbf{U}_t(\tau)$.

By differentiating Eq. (A.23),

$$d\mathbf{S} = \frac{1}{\det \mathbf{F}^e} \left[d\mathbf{F}^e \mathbf{S}^e \mathbf{F}^{eT} + \mathbf{F}^e d\mathbf{S}^e \mathbf{F}^{eT} + \mathbf{F}^e \mathbf{S}^e d\mathbf{F}^{eT} - (\mathbf{F}^e \mathbf{S}^e \mathbf{F}^{eT}) \text{tr}(d\mathbf{F}^e \mathbf{F}^{e-1}) \right] \quad (\text{A.29})$$

In Eq. (A.29), all the variables are at time τ . Eq. (A.26) can be rewritten as the indicial notation as follows:

$$dS_{ij} = w_{ijkl} dE_{t,kl} \quad (\text{A.30})$$

By introducing the following two fourth-rank tensors for convenience,

$$\mathbf{G} = \frac{\partial \mathbf{F}^e}{\partial \mathbf{E}_t} \approx \frac{\partial \mathbf{F}^e}{\partial \mathbf{U}_t}, \quad \mathbf{Q} = \frac{\partial \mathbf{S}^e}{\partial \mathbf{E}_t} \approx \frac{\partial \mathbf{S}^e}{\partial \mathbf{U}_t} \quad (\text{A.31})$$

and rewriting Eq. (A.29) in the indicial notation, the following equation can be obtained:

$$w_{ijkl} = \frac{1}{\det \mathbf{F}^e} \left[G_{ijkl} S_{mn}^e F_{nj}^{eT} + F_{im}^e Q_{mnkl} F_{nj}^{eT} + F_{im}^e S_{mn}^e G_{jnlk} - F_{im}^e S_{mn}^e F_{nj}^{eT} (G_{pqkl} F_{qp}^{e-1}) \right] \quad (\text{A.32})$$

In order to calculate w_{ijkl} in Eq. (A.32), \mathbf{G} and \mathbf{Q} should be calculated.

In the following, the necessary steps will be outlined.

$$(i) \quad \mathbf{G} = \frac{\partial \mathbf{F}^e}{\partial \mathbf{U}_t}$$

$$\mathbf{F}^e(\tau) = \mathbf{R}_t \mathbf{U}_t \mathbf{F}^e(t) \left\{ 1 - \sum_{\alpha} \Delta\gamma^{\alpha} \mathbf{s}_0^{\alpha} - \sum_{\chi} \Delta\gamma^{\chi} \mathbf{s}^{\chi} \right\} \quad (\text{A.33})$$

where \mathbf{R}_t and \mathbf{U}_t are obtained from the polar decomposition of \mathbf{F}_t . By differentiating Eq. (A.33) and rewriting in the indicial notation,

$$\begin{aligned} dF_{ij}^e = & \left[R_{t,ik} F_{lj}^e(t) - R_{t,ik} F_{lp}^e(t) \left\{ \sum_{\alpha} \Delta\gamma^{\alpha} s_{0,pj}^{\alpha} + \sum_{\chi} \Delta\gamma^{\chi} s_{pj}^{\chi} \right\} \right. \\ & \left. - R_{t,im} U_{t,mn} F_{np}^e(t) \left\{ \sum_{\alpha} R_{kl}^{\alpha} s_{0,pj}^{\alpha} + \sum_{\chi} H_{kl}^{\chi} s_{pj}^{\chi} \right\} \right] dU_{t,kl} \end{aligned} \quad (\text{A.34})$$

with

$$\mathbf{R}^{\alpha} = \frac{\partial \Delta\gamma^{\alpha}}{\partial \mathbf{U}_t}, \quad \mathbf{H}^{\chi} = \frac{\partial \Delta\gamma^{\chi}}{\partial \mathbf{U}_t} \quad (\text{A.35})$$

Therefore,

$$\begin{aligned} G_{ijkl} = & \left[R_{t,ik} F_{lj}^e(t) - R_{t,ik} F_{lp}^e(t) \left\{ \sum_{\alpha} \Delta\gamma^{\alpha} s_{0,pj}^{\alpha} + \sum_{\chi} \Delta\gamma^{\chi} s_{pj}^{\chi} \right\} \right. \\ & \left. - R_{t,im} U_{t,mn} F_{np}^e(t) \left\{ \sum_{\alpha} R_{kl}^{\alpha} s_{0,pj}^{\alpha} + \sum_{\chi} H_{kl}^{\chi} s_{pj}^{\chi} \right\} \right] \end{aligned} \quad (\text{A.36})$$

$$(ii) \quad \mathbf{Q} = \frac{\partial \mathbf{S}^e}{\partial \mathbf{U}_t}$$

By differentiating Eq. (A.5),

$$\begin{aligned} d\mathbf{S}^e(\tau) \doteq d\mathbf{S}^{e,tr} - \sum_{\alpha} d\Delta\gamma^{\alpha} \mathbf{C}^{\alpha} - \sum_{\alpha} \Delta\gamma^{\alpha} d\mathbf{C}^{\alpha} \\ - \sum_{\chi} d\Delta\gamma^{\chi} \mathbf{C}^{\chi} - \sum_{\chi} \Delta\gamma^{\chi} d\mathbf{C}^{\chi} \end{aligned} \quad (\text{A.37})$$

Let

$$\frac{\partial \Delta \mathbf{S}^{e,tr}}{\partial \mathbf{U}_t} = \mathbf{D} \quad (\text{A.38})$$

$$\frac{\partial \mathbf{A}}{\partial \mathbf{U}_t} = \mathbf{L} \quad (\text{A.39})$$

From Eq. (A.2),

$$dS_{ij}^{e,tr} = \frac{1}{2} C_{ijmn}^e L_{mnkl} dU_{t,kl} \quad (\text{A.40})$$

Therefore,

$$D_{ijkl} = \frac{1}{2} \mathbf{C}_{ijmn}^e L_{mnkl} \quad (\text{A.41})$$

Next, let

$$\frac{\partial \mathbf{C}^{\alpha}}{\partial \mathbf{U}_t} = \mathbf{J}^{\alpha} \quad (\text{A.42})$$

From Eq. (A.3),

$$d\mathbf{C}_{ij}^{\alpha} = \frac{1}{2} \left\{ C_{ijmn}^e L_{mpkl} s_{0,pn}^{\alpha} + C_{ijmn}^e s_{0,mp}^{\alpha T} L_{pnkl} \right\} dU_{t,kl} \quad (\text{A.43})$$

Therefore,

$$J_{ijkl}^\alpha = \frac{1}{2} \left\{ C_{ijmn}^e L_{mpkl} S_{0,pn}^\alpha + C_{ijmn}^e S_{0,mp}^{\alpha T} L_{pnkl} \right\} \quad (\text{A.44})$$

Next, let

$$\frac{\partial \mathbf{C}^\chi}{\partial \mathbf{U}_t} = \mathbf{K}^\chi \quad (\text{A.45})$$

From Eq. (A.4),

$$dC_{ij}^\chi = \frac{1}{2} \left\{ C_{ijmn}^e L_{mpkl} S_{sb,pn}^\chi + C_{ijmn}^e S_{sb,mp}^{\chi T} L_{pnkl} \right\} dU_{t,kl} \quad (\text{A.46})$$

Therefore,

$$K_{ijkl}^\alpha = \frac{1}{2} \left\{ C_{ijmn}^e L_{mpkl} S_{sb,pn}^\alpha + C_{ijmn}^e S_{sb,mp}^{\alpha T} L_{pnkl} \right\} \quad (\text{A.47})$$

The relation for $d\mathbf{S}^e$ in Eq. (A.37) can be rewritten in terms of \mathbf{D} , \mathbf{R}^α ,

\mathbf{J}^α , \mathbf{H}^χ , and \mathbf{K}^χ as follows:

$$\begin{aligned} dS_{ij}^e = & D_{ijkl} dU_{t,kl} - \sum_{\alpha} R_{kl}^\alpha dU_{t,kl} C_{ij}^\alpha - \sum_{\alpha} \Delta\gamma^\alpha J_{ijkl}^\alpha dU_{t,kl} \\ & - \sum_{\chi} H_{kl}^\chi dU_{t,kl} C_{ij}^\chi - \sum_{\chi} \Delta\gamma^\chi K_{ijkl}^\chi dU_{t,kl} \end{aligned} \quad (\text{A.48})$$

Therefore,

$$Q_{ijkl} = D_{ijkl} - \sum_{\alpha} C_{ij}^\alpha R_{kl}^\alpha - \sum_{\alpha} \Delta\gamma^\alpha J_{ijkl}^\alpha - \sum_{\chi} C_{ij}^\chi H_{kl}^\chi - \sum_{\chi} \Delta\gamma^\chi K_{ijkl}^\chi \quad (\text{A.49})$$

$$\text{(iii) } \mathbf{L} = \frac{\partial \mathbf{A}}{\partial \mathbf{U}_t}$$

$$\mathbf{A} = \mathbf{F}^{eT}(t) \mathbf{U}_t(\tau) \mathbf{U}_t(\tau) \mathbf{F}^e(t) \quad (\text{A.50})$$

By differentiating Eq. (A.50),

$$d\mathbf{A} = \mathbf{F}^{eT}(t) d\mathbf{U}_t(\tau) \mathbf{U}_t(\tau) \mathbf{F}^e(t) + \mathbf{F}^{eT}(t) \mathbf{U}_t(\tau) d\mathbf{U}_t(\tau) \mathbf{F}^e(t) \quad (\text{A.51})$$

By rewriting in the indicial notation,

$$dA_{ij} = F_{ik}^{eT}(t) dU_{t,kl} U_{t,lm} F_{mj}^e(t) + F_{im}^{eT}(t) U_{t,mk} dU_{t,kl} F_{lj}^e(t) \quad (\text{A.52})$$

Therefore,

$$L_{ijkl} = F_{ik}^{eT}(t) U_{t,lm} F_{mj}^e(t) + F_{im}^{eT}(t) U_{t,mk} F_{lj}^e(t) \quad (\text{A.53})$$

$$\text{(iv) } \mathbf{R}^\alpha = \frac{\partial \Delta \gamma^\alpha}{\partial \mathbf{U}_t}$$

$$\Delta \gamma^\alpha = \Delta \gamma^\alpha(\mathbf{S}^e(\mathbf{U}_t)) \quad (\text{A.54})$$

For simplicity, the changes in the dislocation densities during increment Δt is neglected. Therefore, the plastic shear increment for slip is dependent only on the resolved shear stress. Eq. (A.54) can be differentiated as follows.

$$\begin{aligned} \frac{\partial \Delta \gamma^\alpha}{\partial \mathbf{U}_t} \cdot \mathbf{X} &= \left[\frac{d}{d\alpha} \Delta \gamma^\alpha(\mathbf{U}_t + \alpha \mathbf{X}) \right]_{\alpha=0} \\ &= \frac{\partial \Delta \gamma^\alpha}{\partial \mathbf{S}^e} \cdot \frac{\partial \Delta \mathbf{S}^e}{\partial \mathbf{U}_t}[\mathbf{X}] = \left[\frac{\partial \Delta \mathbf{S}^e}{\partial \mathbf{U}_t} \right]^T \left[\frac{\partial \Delta \gamma^\alpha}{\partial \mathbf{S}^e} \right] \cdot \mathbf{X} \end{aligned} \quad (\text{A.55})$$

Let

$$\frac{\partial \Delta \gamma^\alpha}{\partial \mathbf{S}^e} = \mathbf{Y}^\alpha \quad (\text{A.56})$$

Then,

$$R_{ij}^\alpha = Y_{kl}^\alpha Q_{klij} \quad (\text{A.57})$$

$$(v) \mathbf{H}^\lambda = \frac{\partial \Delta \gamma^\lambda}{\partial \mathbf{U}_t}$$

$$\Delta \gamma^\lambda = \Delta \gamma^\lambda (\mathbf{S}^e(\mathbf{U}_t)) \quad (\text{A.58})$$

For the same reason,

$$\begin{aligned} \frac{\partial \Delta \gamma^\lambda}{\partial \mathbf{U}_t} \cdot \mathbf{X} &= \left[\frac{d}{d\alpha} \Delta \gamma^\lambda (\mathbf{U}_t + \alpha \mathbf{X}) \right]_{\alpha=0} \\ &= \frac{\partial \Delta \gamma^\lambda}{\partial \mathbf{S}^e} \cdot \frac{\partial \Delta \mathbf{S}^e}{\partial \mathbf{U}_t} [\mathbf{X}] = \left[\frac{\partial \Delta \mathbf{S}^e}{\partial \mathbf{U}_t} \right]^T \left[\frac{\partial \Delta \gamma^\lambda}{\partial \mathbf{S}^e} \right] \cdot \mathbf{X} \end{aligned} \quad (\text{A.59})$$

Let

$$\frac{\partial \Delta \gamma^\lambda}{\partial \mathbf{T}^e} = \mathbf{Z}^\lambda \quad (\text{A.60})$$

Then,

$$H_{ij}^\lambda = Z_{kl}^\lambda Q_{klij} \quad (\text{A.61})$$

By substituting Eqs. (A.57) and (A.61) in Eq. (A.49), the final expression for \mathbf{Q} can be obtained as follows:

$$\begin{aligned} \mathbf{Q} = & \mathbf{D} - \sum_{\alpha} (\mathbf{C}^{\alpha} \otimes \mathbf{Y}^{\alpha}) \mathbf{Q} - \sum_{\alpha} \Delta\gamma^{\alpha} \mathbf{J}^{\alpha} \\ & - \sum_{\chi} (\mathbf{C}^{\chi} \otimes \mathbf{Z}^{\chi}) \mathbf{Q} - \sum_{\chi} \Delta\gamma^{\chi} \mathbf{K}^{\chi} \end{aligned} \quad (\text{A.62})$$

Therefore,

$$\begin{aligned} \mathbf{Q} = & \left\{ \mathbf{I} + \sum_{\alpha} (\mathbf{C}^{\alpha} \otimes \mathbf{Y}^{\alpha}) + \sum_{\chi} (\mathbf{C}^{\chi} \otimes \mathbf{Z}^{\chi}) \right\}^{-1} \\ & \left\{ \mathbf{D} - \sum_{\alpha} \Delta\gamma^{\alpha} \mathbf{J}^{\alpha} - \sum_{\chi} \Delta\gamma^{\chi} \mathbf{K}^{\chi} \right\} \end{aligned} \quad (\text{A.63})$$

$$\text{(vi)} \quad \mathbf{Y}^{\alpha} = \frac{\partial \Delta\gamma^{\alpha}}{\partial \mathbf{S}^e}$$

$$\begin{aligned} \mathbf{Y}^{\alpha} &= \frac{\partial \Delta\gamma^{\alpha}}{\partial \mathbf{S}^e} = \frac{\partial \Delta\gamma^{\alpha}}{\partial \tau^{\alpha}} \frac{\partial \tau^{\alpha}}{\partial \mathbf{S}^e} = \frac{\partial \Delta\gamma^{\alpha}}{\partial \tau^{\alpha}} \text{sym}(\mathbf{s}_0^{\alpha}) \\ &= \left(\frac{Q_0}{k_b T} \right) \left(\frac{1}{\tau_{CRSS}^{\alpha}} \right) \Delta\gamma^{\alpha} \text{sym}(\mathbf{s}_0^{\alpha}) \end{aligned} \quad (\text{A.64})$$

$$\text{(vii)} \quad \mathbf{Z}^{\chi} = \frac{\partial \Delta\gamma^{\chi}}{\partial \mathbf{S}^e}$$

$$\mathbf{Z}^{\chi} = \gamma_0^{\chi} \left(\frac{Q_0}{k_b T} \right) \left(\frac{\text{sym}(\mathbf{s}^{\chi}) (\tau_0^{\chi} + \mu \sigma^{\chi}) + \mu \tau^{\chi} \text{sym}(\mathbf{n}^{\chi} \otimes \mathbf{n}^{\chi})}{(\tau_0^{\chi} + \mu \sigma^{\chi})^2} \right) \quad (\text{A.65})$$

(viii) C_{ijkl} in global coordinates

Let $\mathbf{C}^{e,c}$ and \mathbf{C}^e denote the fourth order stiffness tensors in the crystal and global basis, respectively. Then, the stress-strain relation with respect to

the crystal basis can be expressed follows:

$$\mathbf{S}^{e,c} = \mathbf{C}^{e,c} : \mathbf{E}^{e,c} \quad (\text{A.66})$$

If \mathbf{B} is the orthogonal tensor that rotates the crystal to global basis, then $\mathbf{S}^e = \mathbf{B}\mathbf{S}^{e,c}\mathbf{B}^T$ and $\mathbf{E}^{e,c} = \mathbf{B}^T\mathbf{E}^e\mathbf{B}$. Therefore,

$$\mathbf{S}^e = \mathbf{B}\mathbf{C}^{e,c} : (\mathbf{B}^T\mathbf{E}^e\mathbf{B})\mathbf{B}^T \quad (\text{A.67})$$

Eq. (A.67) can be rewritten as the indicial notation as follows:

$$S_{ij}^e = B_{im} C_{mnop}^{e,c} B_{ok}^T E_{kl}^e B_{lp} B_{nj}^T \quad (\text{A.68})$$

Therefore,

$$C_{ijkl}^e = B_{im} B_{jn} B_{ko} B_{lp} C_{mnop}^{e,c} \quad (\text{A.69})$$

A.3. Computational algorithm for the analytical Jacobian

(i) Calculate

$$L_{ijkl} = F_{ik}^{e^T}(t)U_{t,lm}(\tau)F_{mj}^e(t) + F_{im}^{e^T}(t)U_{t,mk}(\tau)F_{lj}^e(t)$$

(ii) Calculate

$$C_{ijkl}^e = B_{im}B_{jn}B_{ko}B_{lp}C_{mnop}^{e,c}$$

(iii) Calculate

$$D_{ijkl} = \frac{1}{2}C_{ijmn}^e L_{mnkl}$$

(iv) Calculate

$$J_{ijkl}^\alpha = \frac{1}{2} \left\{ C_{ijmn}^e L_{mpkl} s_{0,pn}^\alpha + C_{ijmn}^e s_{0,mp}^{\alpha^T} L_{pnkl} \right\}$$

$$K_{ijkl}^\alpha = \frac{1}{2} \left\{ C_{ijmn}^e L_{mpkl} s_{sb,pn}^\chi + C_{ijmn}^e s_{sb,mp}^{\chi^T} L_{pnkl} \right\}$$

(v) Calculate

$$\begin{aligned} \mathbf{Y}^\alpha &= \frac{\partial \Delta \gamma^\alpha}{\partial \mathbf{S}^e} = \frac{\partial \Delta \gamma^\alpha}{\partial \tau^\alpha} \frac{\partial \tau^\alpha}{\partial \mathbf{S}^e} = \frac{\partial \Delta \gamma^\alpha}{\partial \tau^\alpha} \text{sym}(\mathbf{s}_0^\alpha) \\ &= \left(\frac{Q_0}{k_b T} \right) \left(\frac{1}{\tau_{CRSS}^\alpha} \right) \Delta \gamma^\alpha \text{sym}(\mathbf{s}_0^\alpha) \end{aligned}$$

$$\mathbf{Z}^\chi = \gamma_0^\chi \left(\frac{Q_0}{k_b T} \right) \left(\frac{\text{sym}(\mathbf{s}^\chi) (\tau_0^\chi + \mu \sigma^\chi) + \mu \tau^\chi \text{sym}(\mathbf{n}^\chi \otimes \mathbf{n}^\chi)}{(\tau_0^\chi + \mu \sigma^\chi)^2} \right)$$

(vi) Calculate

$$Q_{ijkl} = \left\{ I_{ijkl} + \sum_{\alpha} (C_{ij}^{\alpha} Y_{kl}^{\alpha}) + \sum_{\chi} (C_{ij}^{\chi} Z_{kl}^{\chi}) \right\}^{-1} \left\{ D_{ijkl} - \sum_{\alpha} \Delta \gamma^{\alpha} J_{ijkl}^{\alpha} - \sum_{\chi} \Delta \gamma^{\chi} K_{ijkl}^{\chi} \right\}$$

(vii) Calculate

$$R_{ij}^{\alpha} = Y_{kl}^{\alpha} Q_{kl ij}$$

$$H_{ij}^{\chi} = Z_{kl}^{\chi} Q_{kl ij}$$

(viii) Calculate

$$G_{ijkl} = \left[R_{t,ik} F_{lj}^e(t) - R_{t,ik} F_{lp}^e(t) \left\{ \sum_{\alpha} \Delta \gamma^{\alpha} S_{0,pj}^{\alpha} + \sum_{\chi} \Delta \gamma^{\chi} S_{pj}^{\chi} \right\} \right. \\ \left. - R_{t,im} U_{t,mn} F_{np}^e(t) \left\{ \sum_{\alpha} R_{kl}^{\alpha} S_{0,pj}^{\alpha} + \sum_{\chi} H_{kl}^{\chi} S_{pj}^{\chi} \right\} \right]$$

(ix) Calculate

$$w_{ijkl} = \frac{1}{\det \mathbf{F}^e} \left[G_{ijkl} S_{mn}^e F_{nj}^{eT} + F_{im}^e Q_{mnkl} F_{nj}^{eT} \right. \\ \left. + F_{im}^e S_{mn}^e G_{jnkl} - F_{im}^e S_{mn}^e F_{nj}^{eT} (G_{pqkl} \mathbf{F}_{qp}^{e-1}) \right]$$

Reference

[1] S.R. Kalidindi, Polycrystal plasticity: Constitutive modeling and deformation processing, Ph.D. Dissertation, Massachusetts Institute of Technology, Cambridge, MA, USA, 1992.

[2] S. Balasubramanian, Polycrystalline plasticity: application to deformation processing of lightweight metals, Ph.D. Dissertation, Massachusetts Institute of Technology, Cambridge, MA, USA, 1998.

Appendix B. Stress fields around dislocation arrays

The stress field surrounding an isolated edge dislocation with a Burgers vector parallel to the x-axis can be calculated using the following equations [1]:

$$\sigma_{xx} = -\frac{Gb}{2\pi(1-\nu)} \frac{y(3x^2 + y^2)}{(x^2 + y^2)^2} \quad (\text{B.1})$$

$$\sigma_{yy} = \frac{Gb}{2\pi(1-\nu)} \frac{y(x^2 - y^2)}{(x^2 + y^2)^2} \quad (\text{B.2})$$

$$\sigma_{xy} = \frac{Gb}{2\pi(1-\nu)} \frac{x(x^2 - y^2)}{(x^2 + y^2)^2} \quad (\text{B.3})$$

$$\sigma_{zz} = \nu(\sigma_{xx} + \sigma_{yy}) \quad (\text{B.4})$$

$$\sigma_{xz} = \sigma_{yz} = 0 \quad (\text{B.5})$$

where G is the shear modulus, b is the Burgers vector, and ν is Poisson's ratio. The stress component distributions were calculated using Matlab™ software and are depicted in Fig. B-1(a). When dislocations are infinitely arrayed along the x-axis with a distance D between two neighboring dislocations, the stress field can be calculated by applying the following superposition principle [2].

$$\begin{aligned}
\sigma_{xx} &= -\frac{Gb}{2\pi(1-\nu)} \sum_{n=-\infty}^{\infty} \frac{y(3(x-nD)^2 + y^2)}{((x-nD)^2 + y^2)^2} \\
&= -\sigma_0 \left\{ \left(2 \sinh\left(\frac{2\pi y}{D}\right) \left(\cosh\left(\frac{2\pi y}{D}\right) - \cos\left(\frac{2\pi x}{D}\right) \right) \right. \right. \\
&\quad \left. \left. - \left(\frac{2\pi y}{D}\right) \left(\cosh\left(\frac{2\pi y}{D}\right) \cos\left(\frac{2\pi x}{D}\right) - 1 \right) \right\} \tag{B.6}
\end{aligned}$$

$$\begin{aligned}
\sigma_{yy} &= -\frac{Gb}{2\pi(1-\nu)} \sum_{n=-\infty}^{\infty} \frac{y((x-nD)^2 - y^2)}{((x-nD)^2 + y^2)^2} \\
&= -\sigma_0 \left(\frac{2\pi y}{D} \right) \left(\cosh\left(\frac{2\pi y}{D}\right) \cos\left(\frac{2\pi x}{D}\right) - 1 \right) \tag{B.7}
\end{aligned}$$

$$\begin{aligned}
\sigma_{xy} &= -\frac{Gb}{2\pi(1-\nu)} \sum_{n=-\infty}^{\infty} \frac{x((x-nD)^2 - y^2)}{((x-nD)^2 + y^2)^2} \\
&= \sigma_0 \sin\left(\frac{2\pi x}{D}\right) \left(\cosh\left(\frac{2\pi y}{D}\right) \right. \\
&\quad \left. - \cos\left(\frac{2\pi x}{D}\right) - \left(\frac{2\pi y}{D}\right) \sinh\left(\frac{2\pi y}{D}\right) \right) \tag{B.8}
\end{aligned}$$

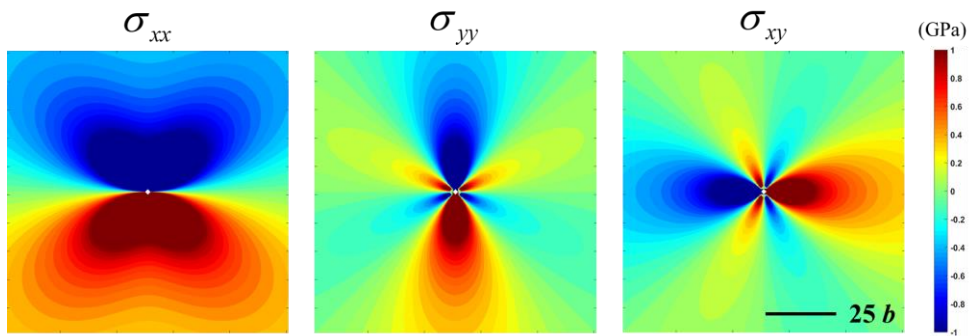
$$\sigma_{zz} = \nu(\sigma_{xx} + \sigma_{yy}) \tag{B.9}$$

$$\sigma_{xz} = \sigma_{yz} = 0 \tag{B.10}$$

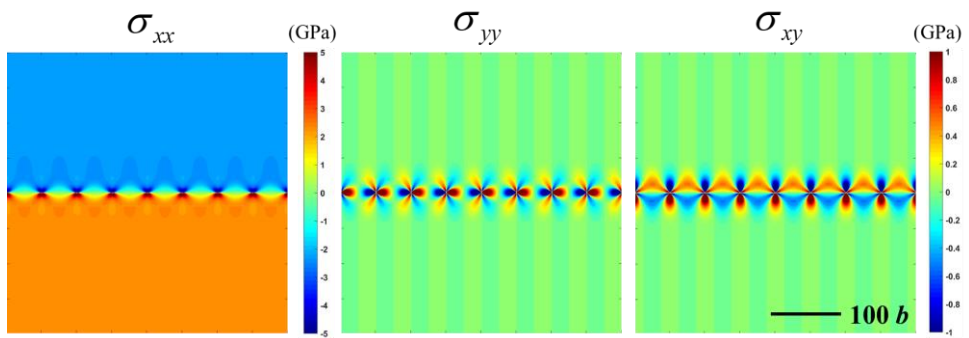
with

$$\sigma_0 = \frac{Gb}{2D(1-\nu) \left(\cosh\left(\frac{2\pi y}{D}\right) - \cos\left(\frac{2\pi x}{D}\right) \right)^2} \tag{B.11}$$

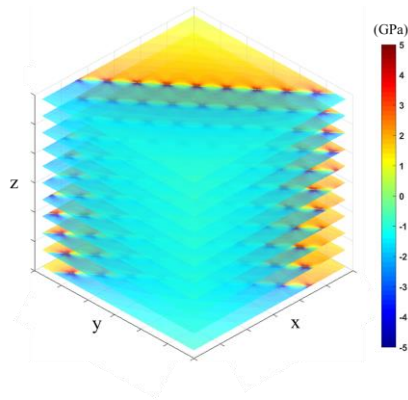
In deformed materials, the piled-up dislocations on the slip system can be approximated as an infinite array of edge dislocations. Consequently, the stress component σ_{xx} tends to saturate towards $\frac{Gb}{D(1-\nu)}\text{sgn}(x)$ as the distance from the slip plane tends to infinity ($y \rightarrow \pm\infty$). Meanwhile, the other components, σ_{yy} and σ_{xy} , tend to saturate towards zero. The saturated value of σ_{xx} is determined by the distance D , which can be related to the dislocation density. For cold-deformed metals, the approximate dislocation density is in the range of $10^{15-16} \text{ m}^{-2}$ [3]. With this value, the stress field of arrayed dislocations at a distance of $40b$ can be calculated, as depicted in Fig. B-1(b). This figure demonstrates that the stress components σ_{yy} and σ_{xy} are nearly zero except near the slip plane, whereas the stress component σ_{xx} exhibits finite saturated values even far from the slip plane. Therefore, except in the vicinity of the slip plane, the direction of the eigenvector corresponding to the maximum principal stress (in absolute value) is parallel to the slip direction (or Burgers vector), or x -axis, in this case. Furthermore, since the magnitude of the maximum principal stress depends on the dislocation density, it is reasonably acceptable to use the dislocation density as the weighting factor for the calculation of the effective slip direction (Eq. (2.57)) under multiple slip activities. Fig. B-1(c) presents an example of the maximum principal stress (in absolute value) in a three-dimensional space for one FCC slip system (111)[1-10].



(a)



(b)



(c)

Fig. B-1. Calculated stress fields for (a) an isolated edge dislocation, and (b) an infinite array of edge dislocations. (c) An example of the maximum principal stress (absolute value) for the (111)[1-10] slip system in FCC metals.

Reference

- [1] P. M. Anderson, J. P. Hirth, J. Lothe, Theory of Dislocations, 3rd edition, Cambridge University Press, Cambridge, 2017.
- [2] A.P. Sutton, R.W. Balluffi, Interfaces in Crystalline Materials, Oxford University Press, Oxford, 1995.
- [3] W. D. Callister, Fundamentals of Materials Science and Engineering: An Integrated Approach, 2nd Edition, Wiley-VCH, Weinheim, 2004.

Appendix C. Dislocation densities measurement using the X-ray diffraction

To evaluate edge and screw dislocation densities, X-ray diffraction (XRD) measurements were performed on the samples before and after cold rolling. The XRD measurement conditions and sample preparation were consistent with those employed for the texture measurement. The edge and screw dislocation densities were measured using the modified Williamson-Hall method, which is based on the analysis of full width at half maximum (FWMH) of the obtained XRD peaks. The Rigaku PDXL2 software was utilized to determine the full width at half maximum (FWHM) values from the XRD peaks.

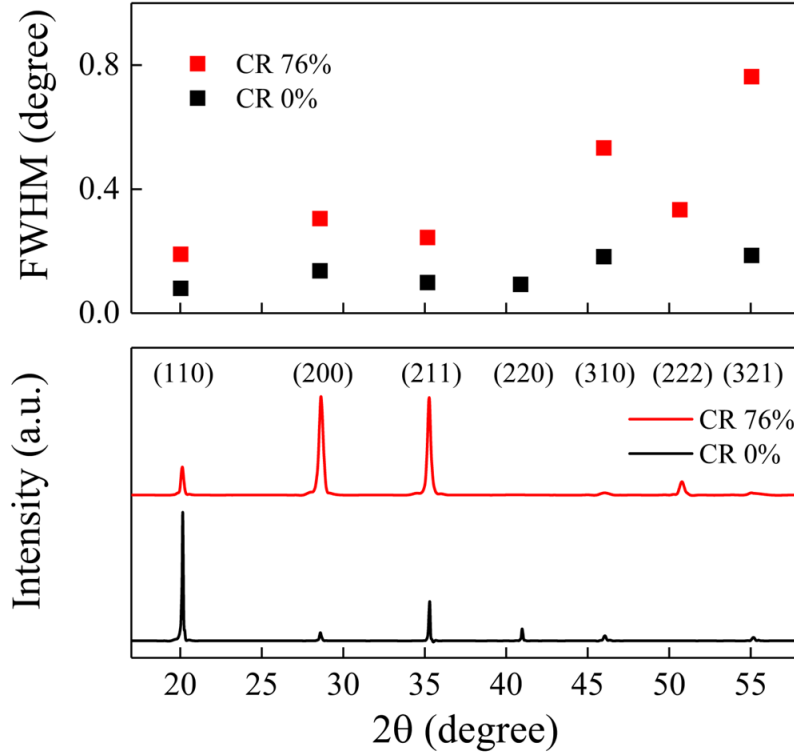


Fig. C-1. The XRD peaks of the GO electrical steel before and after cold rolling, along with the corresponding full width at half maximum (FWHM) at each peak. The 6 peaks detected in order starting from the (110) were utilized for evaluating the dislocation density.

According to modified Williamson-Hall method, ΔK (FWHM) can be expressed as [1]:

$$\Delta K \cong \frac{0.9}{D} + \left(\frac{\pi M^2 b^2}{2} \right)^{\frac{1}{2}} \rho^{\frac{1}{2}} K \sqrt{C} \quad (C.1)$$

where b , D , ρ , represent the burgers vector, average particle size, and average dislocation density, respectively. M is the parameter determined by the effective outer cutoff radius of dislocation. The diffraction vector K can be defined as $K = 2\sin\theta/\lambda$, where λ is the wavelength of the X-ray and θ is the diffraction angle.

Average contrast factor of dislocation, \bar{C} , can be formulated as follows [2]:

$$\bar{C}_{hkl} = \bar{C}_{h00} (1 - qH^2) \quad (C.2)$$

$$H^2 = \frac{(h^2k^2 + k^2l^2 + l^2h^2)}{(h^2 + k^2 + l^2)}. \quad (C.3)$$

Here, \bar{C}_{h00} represents the average dislocation contrast factor for the $\{h00\}$ reflection and q is the value indicating the dislocation character. Substituting Eq. (C.2) into Eq. (C.1) yields the following expression:

$$\frac{[(\Delta K)^2 - \alpha]}{K^2} \cong \beta \bar{C}_{h00} (1 - qH^2) \quad (C.4)$$

Here, $\alpha = (0.9/D)^2$ and $\beta = (\pi M^2 b^2 / 2) \rho$. By plotting $\frac{[(\Delta K)^2 - \alpha]}{K^2}$ against H^2 and linear regression, $-q\beta\bar{C}_{h00}$ (slope of regression line) and $\beta\bar{C}_{h00}$ (intercept of regression line) can be obtained [3,4]. The experimental

value of q can be determined by taking the ratio of these two values. By comparing the experimental value of q with the theoretical value of q (q^{th}), the fraction of screw and edge dislocations can be obtained [5].

$$f_{edge} = \frac{q_{screw}^{th} - q}{q_{screw}^{th} - q_{edge}^{th}} \quad (C.5)$$

The theoretical value of q for pure screw/edge dislocation can be determined using elastic anisotropy A_n , which can be expressed in terms of elastic constants.

$$q^{th} = a^q \left[1 - \exp\left(\frac{-A_n}{b^q}\right) \right] + c^q A_n + d^q \quad (C.6)$$

$$A_n = \frac{2C_{44}}{C_{11} - C_{12}} \quad (C.7)$$

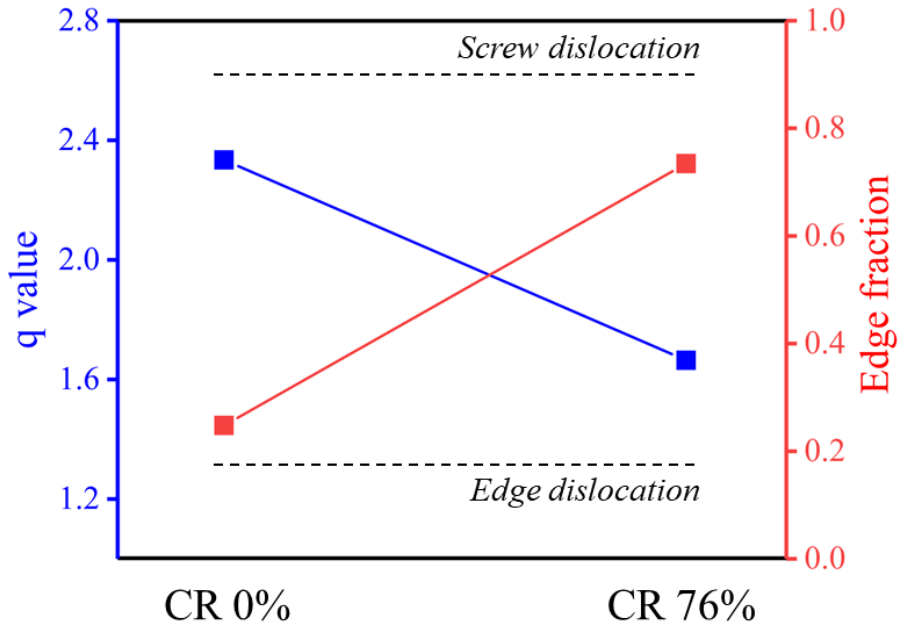


Fig. C-2. Experimentally measured q value (blue) and the fraction of edge component (red) determined by the modified Williamson-Hall method.

The average contrast factor of dislocation \bar{C}_{h00} is obtained by taking the weighted average of C_{h00} values for pure edge and screw components, which are determined by experimentally measured q value and Eq. (C.5). C_{h00} can also be expressed in terms of elastic anisotropy, a , b , c , and d as follows [2]:

$$C_{h00} = a^c [1 - \exp(\frac{-A_n}{b^c})] + c^c A + d^c \quad (\text{C.8})$$

The elastic constants utilized in here are identical to those employed in the manuscript. The other parameters required for Eq. (C.6) and (C.8) can be obtained from previous work [2]. By utilizing \bar{C}_{h00} values obtained from Eq. (S8), we determined the total dislocation density using the Convolutional Multiple Whole Profile (CMWP) fitting procedure based on the Wilkins model [6,7].

Reference

- [1] T. Ungár, A. Borbély, The effect of dislocation contrast on x-ray line broadening: A new approach to line profile analysis, *Appl Phys Lett.* 69 (1996) 3173–3175.
- [2] T. Ungár, I. Dragomir, Á. Révész, A. Borbély, The contrast factors of dislocations in cubic crystals: the dislocation model of strain anisotropy in practice, *J Appl Crystallogr.* 32 (1999) 992–1002.
- [3] F. HajyAkbari, J. Sietsma, A.J. Böttger, M.J. Santofimia, An improved X-ray diffraction analysis method to characterize dislocation density in lath martensitic structures, *Materials Science and Engineering: A.* 639 (2015)

208–218.

[4] E. Schafner, M. Zehetbauer, T. Ungár, Measurement of screw and edge dislocation density by means of X-ray Bragg profile analysis, *Materials Science and Engineering: A*. 319–321 (2001) 220–223.

[5] Z. Cong, Y. Murata, Dislocation Density of Lath Martensite in 10Cr-5W Heat-Resistant Steels, *Mater Trans.* 52 (2011) 2151–2154.

[6] G. Ribárik, J. Gubicza, T. Ungár, Correlation between strength and microstructure of ball-milled Al–Mg alloys determined by X-ray diffraction, *Materials Science and Engineering: A*. 387–389 (2004) 343–347.

[7] M. Wilkens, The determination of density and distribution of dislocations in deformed single crystals from broadened X-ray diffraction profiles, *Physica Status Solidi (a)*. 2 (1970) 359–370.

Korean abstract

통상적으로 구조용 금속 재료는 열간 압연, 냉간 압연, 그리고 열처리 공정을 포함하는 일련의 열-기계적 (thermo-mechanical) 공정을 통해 제조된다. 이러한 공정 중 금속 재료는 탄소성 변형과 더불어 회복 (recovery)-재결정 (recrystallization)-결정립 성장 (grain growth), 그리고 때로는 상변태 (phase transformation)를 겪으며 결정립 크기, 결정학적 방위(집합조직)와 같은 미세조직적 특성이 발현된다. 그리고 이러한 미세조직적 발현은 금속 재료의 이방성과 성형성을 포함하는 기계적 물성에 직접적으로 영향을 끼친다. 그러므로 성능 요구치를 만족하는 최종 제품을 얻기 위한 공정 설계 단계에서 공정-미세조직-물성-성능 사이 관계에 대한 이해는 필수적이다.

본 연구에서는 철강 소재의 열-기계적 공정 모사를 위해 결정 소성 유한 요소 모델 (crystal plasticity finite element model, CPFEM)과 상장 모델 (phase field model, PFM)을 결합한 모델을 제안하였다. CPFEM 은 기계적 거동 모사 모듈로서 국부적 응력 집중, 불균일 전위 분포, 전단 밴드 (shear band)와 같은 변형 비균질성을 예측하는 데 사용되는 반면, PFM은 미세조직 발현 모사 모듈로서 열처리 공정 중 핵생성과 성장을 포함하는 재결정된 미세조직적 특징을 예측하는 데 사용되었다. 각각 유한요소법과 유한차분법을 수치 체계로 사용하는 CPFEM과 PFM의

완전한 결합을 위해 높은 계산 비용을 초래하지 않는 효율적인 결합 알고리즘이 제시되었다. 특히 철강 소재의 재결정 집합조직을 예측할 수 있는 strain energy release maximization (SERM) 모델이 CPFEM 해석 결과를 이용하여 기계적 하중이 가해진 상태에서 다수의 슬립 활성화도(slip activity)를 고려할 수 있도록 일반화되어 (generalized SERM 모델로 명명) PFM 내에 구현되었다. 제안된 모델은 극저탄소강 (ultra-low carbon steel)과 방향성 전기강판 (grain-oriented electrical steel)에 대해 적용되어 검증되었다.

극저탄소강의 경우 가상 기계적 실험을 통해 열-기계적 공정 후 소재의 이방성과 성형성을 평가하는데 제안된 모델이 사용되었다. 가상 기계적 실험을 통해 방향별 r-value (Lankford coefficient)와 항복 응력 (yield stress)를 예측하였고 실험으로부터 측정된 값과 비교를 통해 검증하였다. 그 후, 예측값과 측정값을 활용하여 이방성 항복함수 (anisotropic yield function)인 Hill'48과 Yld2000-2d의 매개변수를 확보하였다. 마지막으로, 확보한 항복 함수와 Marciniak-Kuczynski (M-K) 모델을 활용하여 성형 한계도 (forming limit diagram, FLD)를 예측하였다. 특히 본 연구에서는 CPFEM 기반의 M-K 모델 또한 활용하여 FLD를 예측하고 실험으로부터 측정된 값과 비교를 통해 제안된 모델을 검증하였다.

방향성 전기강판의 경우 1차 재결정 초기 단계에서 Goss{110}<001> 결정립의 전단 밴드 내 핵생성을 예측하는데 제안된 모델이 사용되었다. CPFEM으로부터 전단 밴드를 예측하기 위해 dual-scale 대표체적요소 (representative volume element, RVE) 모델 접근법이 활용되었다. 이를 통해 전단 밴드의 발현과 슬립 기제 사이 관계, 그리고 전단 밴드의 우선 핵생성 사이트 (preferred nucleation site)로서의 역할 등이 논의되었다. 그 후, 전단 밴드의 발현에 따른 재결정 집합조직의 차이가 논의되었고 이를 통해 전기 강판의 특성을 결정 짓는 Goss를 포함하는 주요 집합조직 성분이 전단 밴드에서 비롯됨을 확인하였다. 모델의 검증은 실험으로부터 측정된 압연, 그리고 재결정 집합조직과의 비교를 통해 이루어졌다.

결론적으로, 두 철강 소재로의 적용을 통해 제안된 모델이 공정-미세조직-물성-성능 사이 관계를 효율적이고 정확하게 예측할 수 있음을 보여주었다.

주요어: 결정 소성 유한 요소 모델, 상장 모델, 정적 재결정, 전단 밴드, 집합조직, 이방성, 성형성

학 번: 2018-24252

감사의 글

이 자리를 빌려 학위 과정을 마치는 동안 제가 도움을 받았던 분들에게 감사를 표현하고 싶습니다. 먼저 제게 학위 과정의 기회를 주시고 연구를 지도해 주신 이명규 교수님께 감사를 드립니다. 다소 어렵게 느껴질 수 있는 사제 간이지만 교수님께서 저를 친근하고 편하게 대해 주셔서 불편함 없이 연구에 집중할 수 있었습니다. 또한 학문적으로도 많은 것을 배워 당당하게 사회에 첫 발걸음을 내디딜 수 있을 것 같습니다.

또 다른 지도 교수님이신 한홍남 교수님께도 감사를 드리고 싶습니다. 연구를 진행하며 막히는 부분이 있을 때 학문적으로 통찰력 있는 안목으로 언제나 제게 해결책을 제시해 주셨습니다. 교수님 덕분에 현재의 성과를 이룰 수 있었다고 생각합니다. 항상 좋은 지도에 감사드리며 앞으로도 더 열심히 하는 모습 보여드리겠습니다.

본 연구에서 큰 비중을 차지하고 있는 상장 모델에 대해 도움을 주신 차필령 교수님께도 감사를 드립니다. 갓 입학해서 아무것도 모르는 저를 지도해 주시고 문제를 해결할 때마다 격려해 주셔서 지금까지 올 수 있었습니다. 앞으로도 주어진 공학 문제를 해결할 때 해 주신 조언은 큰 도움이 될 것 같습니다.

결정 소성 모델과 성형성 예측에 도움을 주신 봉혁중 박사님께도 감사를 드립니다. 막막하기만 했던 문제를 같이 논의하고 해결할 기회를 주셔서 감사했습니다. 박사님께서 도움 주신 내용을 바탕으로 해서 앞으로 더 어렵고 복잡한 공학 문제를 해결해 나가도록 노력하겠습니다.

바쁘신 일정에도 불구하고 시간을 내어 주시어 제 학위 심사를 맡아 주시고 귀한 조언해 주신 유웅열 교수님께도 감사의 말씀드립니다.

연구를 지속할 수 있게 지원해 주시고 귀한 조언해 주신 현대자동차 홍승현 상무님, 권순우 책임님, 이충안 책임님, 김현기 책임님께도 감사를 드립니다. 덕분에 학위 과정 동안 연구에 집중할 수 있었고 현재의 성과도 낼 수 있었습니다. 같은 이유로 포스코 주형돈 박사님께도 감사의 말씀드립니다.

돌이켜보면 지난 연구실 생활은 함께한 동료들 덕분에 행복했던 것 같습니다. 이제 막 입학한 신입생을 친절하게 대해주시고 많은 것을 가르쳐 주셨던 우람이 형, 정연 누나, 원재형 정말 감사합니다. 신입생으로서 높아만 보였던 박사후과정을 어느덧 시간이 지나 제가 하게 되었습니다. 저 또한 형, 누나처럼 따듯하게 후배들을 대하겠습니다. 연구실의 두 기둥이었던 우진이 형, 찬양이 형 많이 보고

싶습니다. 형들과 함께 연구실 생활해서 너무 행복했습니다. 같이 있을 때는 몰랐는데 형들 졸업하고 나니 제가 얼마나 큰 도움을 받았는지 알게 됐습니다. 홍진이 형, 기정이 형, 유미 누나, 고려대 시절부터 함께한 시간이 길어서인지 마찬가지로 많이 보고 싶습니다. 함께 웃고 장난칠 수 있는 형, 누나가 있어서 지난 연구실 생활이 행복했던 것 같습니다. 학부때부터 세면 가장 오랜 시간을 함께한 동준이 형, 형과 함께 연구실 생활할 수 있어서 즐거웠습니다. 형 덕분에 연구실 생활하는 동안 많이 웃을 수 있었습니다. 준호 형, 형은 저와 개인적인 시간을 가장 많이 보낸 선배였습니다. 버릇없이 장난쳐도 함께 웃어주고 어려운 일이 있을 때 먼저 손 내밀어 주셔서 감사했습니다. 시간 괜찮으시면 언제 한잔했으면 좋겠습니다. 연구실에 오셔서 항상 후배들 위해주시고 격려해 주신 형림이 형, 함께 연구실 생활할 수 있어서 감사했습니다. 앞으로도 항상 행복하시길 바랍니다. 먼저 졸업한 재민이 형, 석규 형님, 정환이 형, 수현 누나 함께 연구실 생활할 수 있어서 아주 행복했습니다. 고려대에서 함께 연구했던 시간은 잊지 못할 추억이 될 것 같습니다.

연구실 후배들에게도 특별히 감사를 표현하고 싶습니다. 일할 때 다소 날카롭고 예민한 저를 따뜻하게 품어 주어 오히려 제가 큰 도움을 받았던 것 같습니다. 항상 일에 집중하고 깊이 있는 연구를 해서

학문적인 이야기를 할 때마다 든든한 진흥이, 해외에 있어 오랜 기간 떨어져 있었지만 보고 싶은 찬미, 이미 졸업해서 번듯하게 자리를 잡은 재승이, 모두 첫 후배라 서툴렀던 것만 같은데 감사합니다. 현대제철 지영 누나, 혜진 누나 함께 연구실 생활할 수 있어서 행복했습니다. 앞으로도 자주 만났으면 좋겠습니다. 서연 누나, 인생 선배로서, 그리고 학문적인 선배로서 항상 큰 도움을 주셔서 감사했습니다. 앞으로도 상변태 관련해서 많이 물어볼 것 같습니다. 잘 부탁드립니다. 영원한 연구실 막내 똑똑이 성환이, 거대 근육 하이드로 건진이, 같은 방에서 같이 연구할 수 있어서 행복했습니다. 새벽에 제로 맥주 마시면서 우리 신세 한탄하던 건 잊지 못할 것 같습니다. 공업 수학과 무기체계를 가르치는 3사관학교 기계공학과 교수 정영민 대위님을 중심으로 한 우리 애국 멤버들 - 서준, 정윤, 규장, 진모 - 함께한 시간은 잊지 못할 것 같습니다. 앞으로도 나라를 위하는 마음 변치 않았으면 좋겠습니다. 처음 만났을 때 외모로 깜짝 놀랐던 최국진 대위님, 앞으로도 멋진 외모 유지하시면서 졸업 준비 잘하시길 바랍니다. 연구실에서 새로운 커리어를 시작하시는 도영호 책임님, 이성비 연구원님, 이호영 책임님, 김영재 책임님, 앞으로의 행복과 무궁한 발전을 기원합니다. 마지막으로 연구실 아가들 - 태현, 민광, 중현, 제현, 태혁 - 열심히 연구해서 대한민국의 과학계를 휘어잡을 멋진 연구원이 되길 바랍니다.

한홍남 교수님 연구실의 혁재에게도 특별히 감사를 포함합니다. 다른 연구실임에도 불구하고 지도 교수님처럼 언제나 열정적으로 연구에 임하는 모습은 선배이지만 배울 점이 많았습니다. 그리고 잘생긴 얼굴에서도 배울 점이 많았습니다. 뚜렷한 이목구비처럼 준비 잘 해서 뚜렷한 성과와 함께 멋있게 졸업하길 바라겠습니다.

사랑하는 아버지, 어머니, 그리고 예쁜 내 동생 예림이, 학위 과정하는 동안 열렬한 응원과 아낌없는 지원에 감사드립니다. 우리 가족의 든든한 지지 덕분에 무사히 학위 과정을 마칠 수 있었습니다. 우리 가족의 행복을 빌며 이제 제가 우리 가족의 든든한 기둥이 되겠습니다.

마지막으로 사랑하는 도이야. 항상 연구에 집중하느라 바쁘다는 핑계로 함께 시간을 많이 보내지 못해서 미안했어. 내 곁에 있어 준 것만으로도 얼마나 큰 도움이 되었는지 모르겠다. 연구에 지칠 때 마다 도이가 웃는 모습을 생각하면서 흐트러진 마음을 바로잡을 수 있었어. 이제 내가 도이 옆에 서서 도이의 도전을 응원할게. 앞으로 우리의 결혼 생활도 웃음과 행복만 가득하길. 사랑해.

민경문 드림